The Radiative Decay Mode of the Free Neutron

by

Robert L. Cooper

A dissertation submitted in partial fulfillment
of the requirements for the degree of
Doctor of Philosophy
(Physics)
in The University of Michigan
2008

Doctoral Committee:

Professor Timothy E. Chupp, Chair
Emeritus Professor Glenn F. Knoll
Professor David W. Gidley
Professor Gordon L. Kane
Professor Jianming Qian

To my wife and to my mother

ACKNOWLEDGEMENTS

First and foremost, this dissertation would have been impossible without the constant support, guidance, and large dose of patience from my collaborators. Scott Dewey, Alan Thompson, Fred Wietfeldt, Betsy Beise, Kevin Coakley, and Herbert Breuer have all contributed so much to my intellectual growth, and I am immensely grateful for the opportunity to work with them. As I take my next step towards a postdoc, I have learned from Pieter Mumm and Brian Fisher about being a postdoc. Both would strongly encourage me to forget everything I learned in this case, but it's that humbleness that has endeared them to me so much. My fellow graduate students at NIST; "Piston", Chris, Da, Andrew, Liang, Dima, and their significant others have enriched my life in innumerable ways. To them, all that I can say is, "asps." I am grateful for the deep intellectual conversations with Jim Byrne. I have learned so much from him about physics and the historical significance of the work we're doing. I have had many theoretical conversations with Susan Gardner, and she has inspired me in more ways than she probably realizes.

I have been fortunate to have had nearly three advisors in graduate school; Tim Chupp, Jeff Nico, and Tom Gentile. Jeff's light-hearted demeanor was a joy to work with. I never realized lobotomized gibbons were responsible for so much physics before meeting Jeff. I truly appreciate Tom's serious dedication to his craft that is unfettered by ego and driven by the desire to understand the problem at hand. My advisor, Tim, has given me a long leash in graduate school to pursue many projects

that interested me. I am grateful for the ability to be curious, ask tough questions and to be supported when I have wanted to investigate something for myself. Most of all, Tim has taught me the importance of intellectual excellence, and that if a problem is worth doing, it should be done as well.

Eric Tardiff, Behzad Ebrahimi, and Monisha Sharma from the Chupp group have been dear friends whom I have leaned on through graduate school. Furthermore, I am glad that when Eric spoke, I listened. I hope our paths cross in the future. My college friends; Jamey, Dave, Kevin, Pat, Matt, Ryan, and their significant others have been with me from the beginning, and I can honestly say that with their presence, I've had more fun than a graduate student should.

I would not be here without the constant support of my parents. They have always believed in me, and that support has allowed me to give 100 % effort to my work. I really can't say enough to acknowledge everything they have done for me.

I have saved the best for last. Amy, my wife, has been an unending source of support, love, and inspiration. I am grateful for her infinite patience and sunny attitude. She has been a constant source of strength, and I can't acknowledge enough about how awesome she is.

TABLE OF CONTENTS

LIST OF FIGURES

Figure

LIST OF TABLES

LIST OF APPENDICES

Appendix

CHAPTER I

Introduction

In this chapter, a historical treatment is given that describes the development of the weak interaction and beta decay in neutrons. The current state of the neutron lifetime measurements is reviewed, and the consequences of a 6 σ discrepancy in the neutron lifetime are reviewed. The uncertainty in the neutron lifetime measurements motivates the study of the radiative decay mode of the free neutron. The radiative decay mode is another decay branch of the neutron, and it contributes to the lifetime. The motivation for measuring the radiative decay mode of the neutron is given. At the end of the chapter, an outline of the dissertation is given.

1.1 History of the Weak Interaction and Neutron Beta decay

Chadwick first discovered the neutron in 1932 by bombarding alpha particles from radioactive polonium onto a beryllium target, producing neutrons. The resulting neutron beam was scattered by nuclear targets, and the neutron was found to have a mass similar to the proton [8]. Snell and Miller [9] later discovered that the neutron beam from a nuclear reactor pile at Oak Ridge National Laboratory decayed. Groups at Oak Ridge National Laboratory [10] and Chalk River in Canada [11, 12] discovered that the neutron decayed into a proton and an electron. The Chalk River group also measured the continuous electron energy spectrum and its endpoint energy. By this

time, Pauli had postulated the existence of the neutrino to account for the continuous electron energy spectra and to conserve angular momentum. These measurements were consistent with the neutron beta decaying to a proton, an electron, and an unobserved antineutrino.

In 1957, Wu et al. discovered parity violation by observing a directional decay asymmetry of electrons from polarized ^{60}Co at the National Bureau of Standards [13]. Garwin et al. performed an experiment at Brookhaven soon afterwards which confirmed parity violation in muon decays [14]. Frauenfelder later was able to measure the helicity of the outgoing neutrino in ^{60}Co, and these neutrinos always had left-handed helicity. Additionally, a series of experiments by Goldhaber [15, 16] measured the electron helicity to be $-v/c$ where v is the electron velocity. These results are all consistent with the weak interaction being a purely left-handed interaction which maximally violate parity.

Also in 1957, Jackson, Treiman, and Wyld Jr. (JTW) calculated the lowest order differential decay rate for a polarized nucleus [17, 18] using a general, Lorentz invariant parameterization of the weak interaction postulated by Lee and Yang [19]. The resulting decay rate was written as a function of the possible interaction strengths in this parameterization. The weak interaction is left-handed, but it was unknown if it was dominantly vector and axial-vector combinations (V, A), scalar and tensor combinations (S, T), or a mixture of the four.

The angular dependence of the decay products in unpolarized nuclear decay was measured to address this problem. The decay intensity $I(\theta_{e\bar{\nu}})$ for an unpolarized nucleus is a function of the for electron-antineutrino opening angle $\theta_{e\bar{\nu}}$, and it is

$$I(\theta_{e\nu}) \propto 1 - a\frac{v}{c}\cos\theta_{e\bar{\nu}} \tag{1.1}$$

where v is the electron velocity and a is a correlation coefficient. The value of the

Interaction	Coefficient a
Scalar (S)	+1
Tensor (T)	+1/3
Axial-Vector (A)	-1/3
Vector (V)	-1

Table 1.1: Value of symmetry parameter a for a pure type of interaction.

correlation coefficient a is a function of the structure of the weak interaction and of the decay, and its value can be found in [17]. The value of a for each interaction type is given in table 1.1. Pure Fermi transitions (FT) are those that preserve parity, total angular momentum and isospin, i.e. $\Delta J = 0$, $\Delta T = 0$. Gamow-Teller transitions (GT) violate parity and can change total angular momentum and isospin by 0 or 1 i.e. $|\Delta J| = 0$ or 1 but no $0 \rightarrow 0$ and $|\Delta T| = 0$ or 1 with no $0 \rightarrow 0$.

FT transitions arise from only S or V interactions, and GT transitions arise from only A or T. References [20, 21] discuss various FT, GT, and mixed transitions and conclude that the weak interaction is a vector - axial-vector interaction ($V-A$). From JTW, any admixture of S, T interactions appears as measurable distortions in the electron energy spectrum. These distortions are measurable in the Fierz interference term b, described in Chapter II. Tests to observe non-V/A interactions have placed very stringent limits on their size [22, 23].

For FT or GT transitions, the strength of A relative to V is unnecessary in determining a because only one type of interaction contributes. For a mixed transition, there is an admixture of FT and GT, and the measured strength of A relative to V in neutron decay is λ. The parameter λ not only determines a in angular correlation measurements, but it factors in the absolute neutron decay rate. The neutron lifetime is inversely proportional to the total interaction strength, and it is

$$\tau_n^{-1} = K|V_{ud}|(1 + 3|\lambda|^2) \tag{1.2}$$

where the factor of 3 is from the 3 projections of $|\Delta J| = 1$ for neutron decay ($1/2^+ \rightarrow 1/2^+$). The parameter K is a constant to be discussed later, and $|V_{ud}|$ is a weak interaction factor discussed below. Angular correlations (λ) and the neutron lifetime (τ_n) are important to understanding the structure of the weak interaction.

1.2 Neutron Decay and Lifetime

The neutron is composed of three valence quarks, two down quarks and one up quark. Beta decay converts one of the down quarks into an up quark while the virtual W^- gauge boson that mediates the interaction decays to an electron and antineutrino. To measure the neutron lifetime, an experiment must measure either the neutron survival rate or the decay rate through its decay products. One method is to trap ultra-cold neutrons (UCNs) in a magnetic, gravitational, or material bottle and count the surviving neutrons. UCNs are neutrons with kinetic energies less than 0.2 μeV. A decay rate measurement can operate with a UCN bottle or a cold neutron beam. A more detailed description of the types of neutron lifetime experiments is in a review article by Nico and Snow [24].

The four most recent lifetime measurements are given in table 1.2. Before 2005, the neutron lifetime measurements were in good agreement with the world average [7]. The first three are the most recent measurements which are included in the Particle Data Group (PDG) world average while the latest measurement differs significantly from these measurements comprising the PDG world average [6]. Because the neutron lifetime is important in understanding to the structure of weak interaction, the 6 σ discrepancy between the latest measurement and PDG world average must be resolved.

Measurement and Year	Neutron Lifetime [s]	Measurement Type
Byrne 1996 [25]	$889.2 \pm 3.0\,[\text{syst.}] \pm 3.8\,[\text{stat.}]$	Beam, Penning trap
Arzumanov 2000 [26]	$885.4 \pm 0.9\,[\text{syst.}] \pm 0.4\,[\text{stat.}]$	Bottle, UCN gravitational trap
Nico 2005 [27]	$886.3 \pm 1.2\,[\text{syst.}] \pm 3.2\,[\text{stat.}]$	Beam, Penning trap
World Average	885.7 ± 0.8	
Serebrov 2005 [7]	$878.5 \pm 0.7\,[\text{syst.}] \pm 0.3\,[\text{stat.}]$	Bottle, UCN gravitational trap

Table 1.2: The four most recent neutron lifetime measurements. The Particle Data Group world average [6] includes the first three measurements and others not listed on the table. The latest result [7] is not included in this average.

1.2.1 CKM unitarity

The decay rate of the neutron occurs with a slight suppression because the mass eigenstates of the quarks are not the same as the weak eigenstates of the quarks that participate in the decay process. The down quark mass eigenstate in the neutron is a linear combination of these weak eigenstates. The Cabibbo-Kobayashi-Maskawa (CKM) matrix determines this mixing and is shown below

$$\begin{pmatrix} d \\ s \\ b \end{pmatrix}_{\text{weak}} = \begin{pmatrix} V_{ud} & V_{us} & V_{ub} \\ V_{cd} & V_{cs} & V_{cb} \\ V_{td} & V_{ts} & V_{tb} \end{pmatrix}_{\text{CKM}} \begin{pmatrix} d \\ s \\ b \end{pmatrix}_{\text{mass}} . \tag{1.3}$$

The CKM matrix is unitary, and a significant deviation from unitarity from measurements is indicative of new physics. New physics models that can be incorporated into neutron decay include scalar / tensor interactions from a Higgs or supersymmetric particles, exotic contact interactions, and several others. References [22, 23] discuss these extensions to the Standard Model of particle physics and their experimental constraints from neutron decay.

The unitarity condition implies the condition

$$|V_{ud}|^2 + |V_{us}|^2 + |V_{ub}|^2 = 1. \tag{1.4}$$

The PDG reports that $|V_{ud}| = 0.97418 \pm 0.00027$, and this value is from nuclear

$0^+ \rightarrow 0^+$ superallowed decays [6, 28, 29, 30]. The dominant sources of uncertainties are Coulomb distortions, radiative corrections, and nuclear structure effects. $|V_{ud}|$ can also be derived from pion decays ($\pi^+ \rightarrow \pi^0 e^+ \nu_e$), and it is 0.9751 ± 0.0027. This measurement is consistent with the superallowed decays [31]. The parameter $|V_{us}| = 0.2255 \pm 0.0019$, and its reported value has recently changed due to new experimental data and a new calculation of its form factor [6, 29]. The PDG reports that $|V_{ub}| = (3.93 \pm 0.36) \times 10^{-3}$ which is a negligible contribution to the unitarity sum. The sum in equation 1.4 is satisfied by the experimental data.

The parameter $|V_{ud}|$ is also derivable from neutron data, but because it is a mixed transition, the neutron lifetime and λ must both be measured (see equation 1.2). Figure 1.1 shows how the extraction of $|V_{ud}|$ is affected by the discrepancy in the neutron lifetime and the uncertain value of λ. Using the PDG values for the neutron lifetime and $\lambda = -1.2695 \pm 0.0029$, $|V_{ud}| = 0.9745 \pm 0.0018$.

The value for the neutron lifetime is unclear. Despite the small theoretical uncertainties for the neutron compared to the nuclear $0^+ \rightarrow 0^+$ superallowed decays, the experimental uncertainties are much larger. The uncertainties for each system that is sensitive to $|V_{ud}|$ are shown in figure 1.2.

1.2.2 Connection to radiative final states

The previous discussion of the neutron lifetime has shown that the neutron lifetime suffers from a dramatic discrepancy. It is imperative that every aspect of the neutron lifetime be investigated to understand the origin of these problems. The radiative decay mode has been theoretically calculated as a correction to neutron, and these calculations are the δ_R and Δ_R terms in figure 1.2. It is advisable to measure these factors directly despite the confidence in the calculation of these corrections. Additionally, measurements of λ are also discrepant.

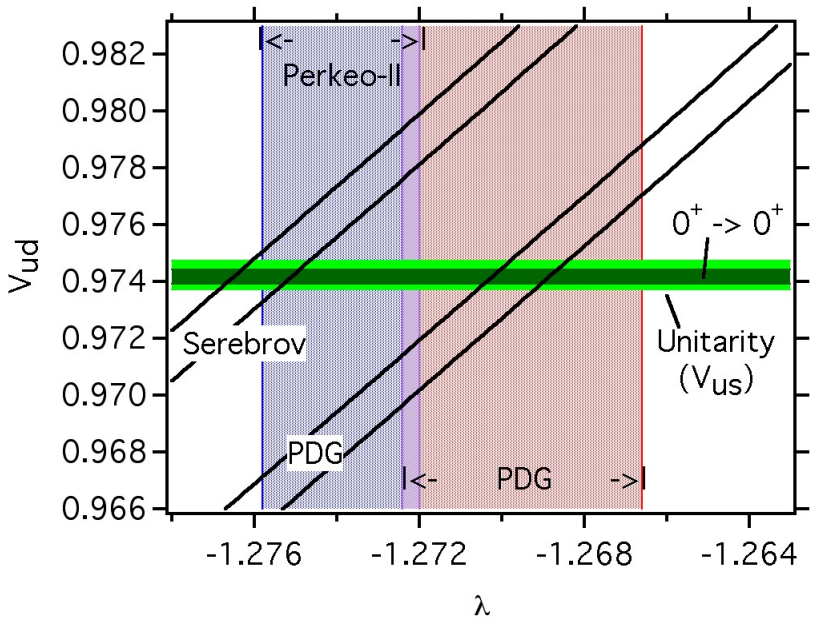

Figure 1.1: $|V_{ud}|$ can be extracted from the neutron lifetime and λ. There is significant uncertainty in the value of the neutron lifetime, and the landscape is not well constrained by λ either. It is interesting to note that pairs of lifetime / λ data points are consistent with unitarity.

The uncertainty of the neutron lifetime measurements is at the 0.1 % level, and the branching ratio for radiative decay to high energy photons is approximately 0.3%. The measurements of λ are also approaching this level of sensitivity. Therefore, any measurement at this level of precision must understand the effects of radiative decay. For example, the addition of a photon to the final state changes the average opening angle between the electron and proton. A measurement which is sensitive to this opening angle (a measure of a) is sensitive to the radiative decay mode. The radiative decay mode has a different electron energy spectrum than non-radiative decay. Therefore, a precise measurement of the electron spectrum is affected by radiative decay.

Neutrons experiments that measure the final decay products can potentially misidentify a high energy photon as a charged particle. This is true for experiments that

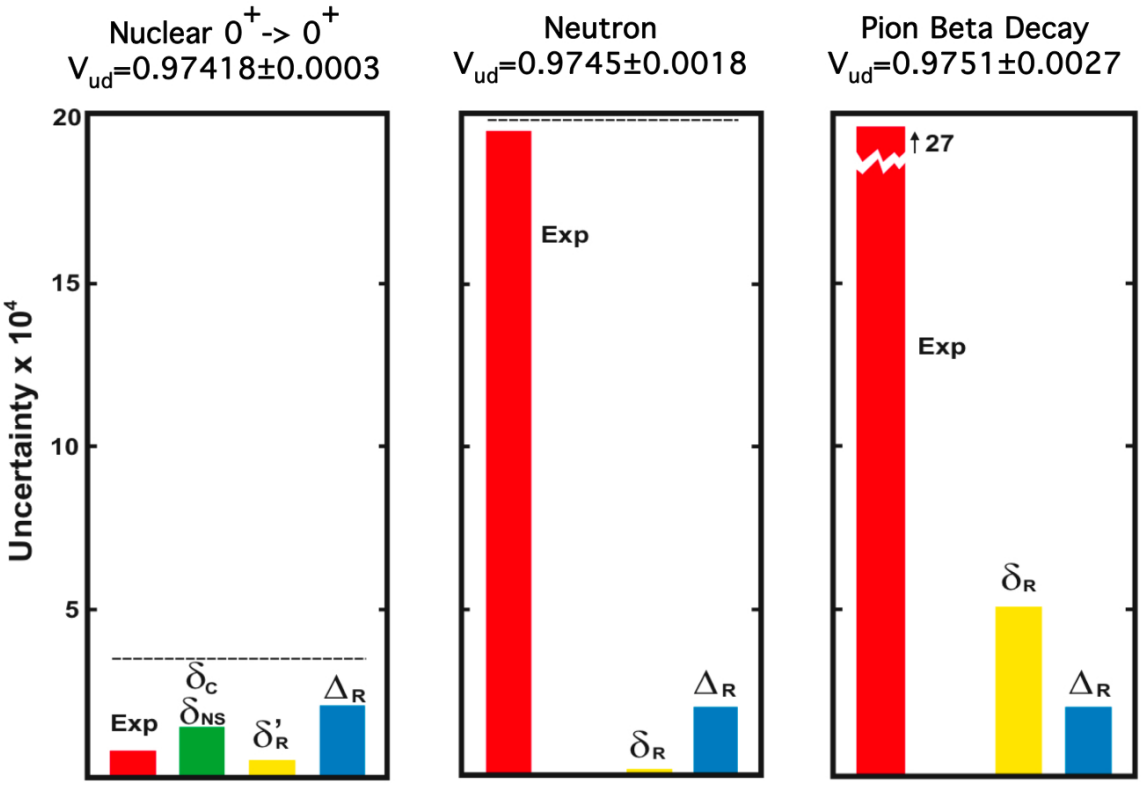

Figure 1.2: The sources of uncertainty for each extraction of $|V_{ud}|$. While the neutron's theoretical uncertainties are very small, the experimental uncertainty (EXP) is much worse than in nuclear $0^+ \rightarrow 0^+$ superallowed decays. The numbers represent the uncertainty attributed to the corrections. The correction δ_R is the radiative correction to the total phase space of the decay. The correction Δ_R is radiative corrections due to higher order interactions. The corrections δ_C and δ_{NS} are due to Coulomb and nuclear structure effects. Figure from reference [1].

collect total scintillation light in a medium of trapped UCNs. Experiments that directly count UCNs are likely to be insensitive to the radiative decay mode, but the stray photons might be responsible for an unaccounted for background. Furthermore, any extraction of V_{ud} requires radiative corrections which have only been calculated and not directly measured.

1.3 Previous Radiative Decay Measurements

Continuous gamma radiation spectra from nuclear beta decays was first observed by Aston [32], and has been observed in many nuclear beta decay systems, including forbidden beta decays [33]. Theoretical models were developed in 1936 [34, 35] to describe these measurements. Additionally, nuclei have a rich excited state structure which leads to enhancements in the nuclear radiative decay that won't be observed in the neutron. The nucleus can also capture a core, atomic electron and radiatively decay. Martin and Glauber established a theoretical framework for calculating the radiative electron capture in atoms [36], and many measurements have been made [37, 38]. The atomic and nuclear structure means that nuclei can radiatively decay at a high rate while the neutron radiative decay mode has been elusive because it lacks these enhancements.

An early measurement of the radiative decay mode of the neutron was performed in 2002 at the Institut Laue-Langevin in Grenoble, France [39]. The experiment performed an electron-delayed proton-photon triple coincidence measurement to identify the radiative decay mode. A plastic scintillator was used to detect the decay electrons, while a microchannel plate (MCP) was used to detect the decay protons. A series of electrostatic grids was used to accelerate the protons into the MCP. Six CsI(Tl) scintillators were placed around the electron detector to detect the photons.

The photon detectors were positioned to be sensitive to photons that are emitted at 35° from the detected electron. This angle was found to be the most probable angle for photon emission for the 35 keV to 100 keV photons that the experiment was sensitive to. A schematic of the experiment is shown in figure 1.3

The first experimental runs measured a rate of electron-delayed proton-photon events that were higher than theory predicts due to residual gas / ion contamination in the vacuum system. A new vacuum system dramatically reduced these ion coincidences, but the experiment was still dominated by backgrounds and detector noise. The experiment constrained the branching ratio for photons with energy from 35 keV to 100 keV to 6.9×10^{-3} at the 90 % confidence level. Theory predicts the branching ratio is 1.1×10^{-3} for photons in this energy range. The report of a more recent experiment using this apparatus [40] is disputed [23] with compelling arguments.

1.4 Motivation

The radiative decay mode is a fundamental test of a semileptonic decay mode. Because of the discrepancies in the neutron lifetime measurements (and λ), studying every contribution to the lifetime is imperative. A precise measurement of the neutron lifetime must include the effect of radiative corrections. Taken individually, some of these corrections are infinite in magnitude, and they require the inclusion of the radiative decay mode to cancel these infinities. Measuring the photon energy dependence of the radiative decay mode yields an energy dependent study of the radiative corrections to the neutron lifetime.

The addition of the photon in the final state introduces new angular correlations of the photon momentum with the other particles' momenta. The photon momentum can be correlated with the neutron spin in polarized neutron decay. A measurement

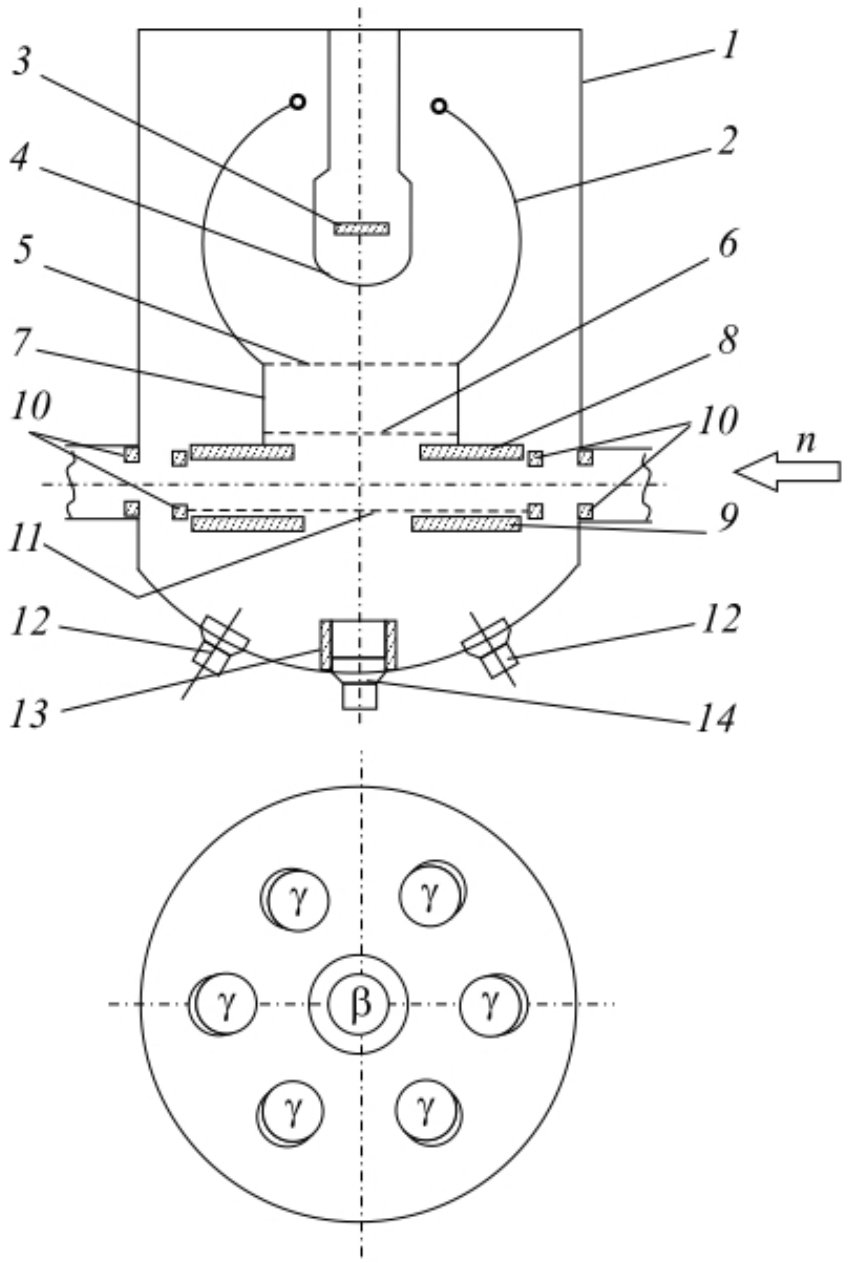

Figure 1.3: The schematic of the experimental apparatus used in the ILL measurement. The components in set up are: 1 - vacuum chamber, 2, 4 - 7, 11 - electrostatic grid, 3 - MCP proton detector, 8, 9 - plastic collimators, 10 - LiF diaphragm, 12 - CsI(Tl) photon detectors, 13 - lead cup, 14 electron detector.

of the photon polarization at high photon energy (near decay endpoint) is a test of right-handed weak interactions. These new angular correlation measurements can be used to measure λ.

Neutron decay can yield precise measurements because it is devoid of complicated nuclear structure effects, making it a reliable system to study experimentally and theoretically. Quantum electrodynamics can be used to calculate the dominant contribution to the radiative decay mode, and experimental measurements test these predictions. Therefore, radiative decay is not only important in support of the neutron lifetime, but it is important as an electroweak test in its own right.

1.5 Overview of the Dissertation

The remainder of this dissertation describes an experiment performed to measure the branching ratio of the radiative decay mode for photons with energy of 15 keV to 340 keV. The measured branching ratio is $(3.09 \pm 0.32) \times 10^{-3}$, and the photon energy spectrum is also extracted.

Chapter II constructs the theoretical framework of the weak interaction to calculate the neutron decay rate. The effect of bremsstrahlung and radiative corrections on the neutron motivates calculating the radiative decay mode. The remainder of the chapter extends previous calculations to polarized neutrons, motivating new angular correlation measurements.

Chapter III describes the experimental apparatus consisting of the neutron beamline, superconducting magnet, electron / proton detector, and photon detector. The photon detector is unique because it must operate in the cryogenic, high magnetic field environment of the superconducting magnet. The selection criteria for the photon detector are reviewed, and the discussion is general enough to be applied to any

future radiative decay experiments.

Chapter IV focuses on the collection and analysis of the raw data. The analysis reduces the data, extracts timing and energy parameters, and then applies analysis cuts. The resulting timing and energy spectra are presented and compared to a Monte Carlo simulation (MC).

Chapter V describes the MC which is composed of an event generator, event tracker, and a routine that simulates detector response. The event generator and tracking algorithms are discussed in detail, but the detector response was largely relegated to packaged software which is described. The MC results derive from the theoretical results that are calculated in chapter II.

Chapter VI discusses the systematic corrections and uncertainties that alter the measured value for the radiative decay branching ratio. These are broadly categorized into uncertainties of the photon detector, measurement of the charged particle energy, timing cuts, correlated background events, and model used in the MC. A table with all the systematic corrections and uncertainties is presented.

Chapter VII concludes the description of the experiment and presents the final branching ratio with uncertainties. While the Monte Carlo comparison to the photon energy spectrum is ongoing, important issues are brought to light. Finally, the apparatus upgrades completed for a second run of the experiment are discussed.

CHAPTER II

Theoretical Development

The neutron is composed of three constituent (or valence) quarks; two have a down flavor, and one is an up flavor and is stable under the influence of the strong and electromagnetic interactions. However, the weak interaction can convert a constituent down quark into an up quark. This conversion is also accompanied by the emission an electron and antineutrino lepton pair. This decay is mediated by a left-handed interaction through the emission of a virtual W^- gauge boson. This process is calculable at the lowest order, but additional corrections are expected.

Calculating these higher order corrections individually leads to infinite contributions, but when all the corrections are combined, they yield a finite correction due to cancellations. A necessary component of the cancellations are diagrams that have correlated photons in the final state. The presence of charged particles in the final state provides an obvious place where photons can couple to the decay. It is experimentally possible to observe this radiative beta decay mode.

In this chapter, a theoretical framework is developed to understand non-radiative beta decay. This framework can be extended to include higher order corrections, motivating the radiative beta decay mode. Sensitivity to radiative decay allows a new set of measurements to be undertaken. In section 2.1, the weak interaction is

described, and with recourse to symmetry and experimental data, its parity violating structure emerges which yields differential decay rate for neutron beta decay. In section 2.2, the inclusion of inner bremsstrahlung (IB) as a correction is motivated by examining an ideal experiment, and the section concludes with a review of the current state of the neutron lifetime. In section 2.3, the radiative decay mode is first calculated with classical physics and then with the full machinery of quantum field theory. This treatment yields the differential decay rate for radiative beta decay. In section 2.4, the differential decay rate formula is extended to a polarized neutron, and new experimental measurements are motivated. Finally, in section 2.5, a calculation of the final state photon's polarization is used as motivation for a search for new physics.

2.1 The Weak Interaction and Beta decay

This section first develops the framework of the weak interaction by starting with a completely general form that is Lorentz invariant. By appealing to experimental data, the resulting interaction is purely left-handed, but complications arise in nuclear material. While first principles calculations are difficult, the use of symmetries is explored as a way to understand any induced interactions. With a complete framework available for the weak interaction in the neutron, the differential decay rate is calculated.

2.1.1 Structure of the weak interaction

The most general form of the interaction Hamiltonian for a neutron decaying into a proton, electron, and anti-neutrino that satisfies Lorentz invariance is

$$\mathcal{H} = \sum_{i=S,V,A,T,P} \bar{\psi}_p O_i \psi_n \bar{\psi}_e O_i (C_i + C_i' \gamma_5) \psi_{\bar{\nu}}. \tag{2.1}$$

This sum is for interactions whose Lorentz transformation is scalar ($O_S \rightarrow 1$), vector ($O_V \rightarrow \gamma^\mu$), axial vector ($O_A \rightarrow \gamma^\mu\gamma_5$), tensor ($O_T \rightarrow \sigma^{\mu\nu} = \frac{i}{2}[\gamma^\mu, \gamma^\nu]$), and pseudoscalar ($O_P \rightarrow \gamma_5$). There are 10 complex-valued constants which contributes 20 independent, real constants less one for an overall phase [17]. In general, these coupling constants should be thought of as form factors that are a function of the momentum transfered squared e.g. $C_i(q^2)$. Induced operators also arise that have these Lorentz transformation properties and are scaled by the momentum transfer vector q^μ. For example, $q^\mu\gamma_5$ transforms as an axial vector. In neutron decay, the momentum transfer is small compared to the nucleon mass. Therefore, the coupling constants can be approximated by their value at 0 momentum transfer, i.e. $C_i(q^2) \approx C_i(0)$, and induced interactions are small.

Equation 2.1 represents a completely general, Lorentz invariant weak interaction, but experimental data shows that it only contains vector and axial vector operators. The Standard Model (SM) predicts that the quark and lepton weak interaction is a left-handed interaction (also written $V - A$). The leptonic weak current L_μ couples the spin 1/2 antineutrino spinor with the spin 1/2 electron spinor, and it is

$$L_\mu = \bar{v}_{\bar{\nu}}(p_{\bar{\nu}})(1 - \gamma_5)\gamma_\mu u_e(p_e) \tag{2.2}$$

where u_e is the electron spinor with 4-momentum p_e and $\bar{v}_{\bar{\nu}}$ is the antineutrino spinor with momentum $p_{\bar{\nu}}$. The quark level interaction is analogous. The hadronic weak current H^μ of interest is not at quark level, but couples the neutron to the proton. The experimental data indicate the interaction is vector and axial vector but is a mixture of left- and right-handed components.

Before discussing the hadronic weak current structure, it is instructive to understand how the neutron beta decay matrix element is constructed. The SM matrix element $\mathcal{M}$ combines the hadronic weak current (H^μ) to the leptonic weak current

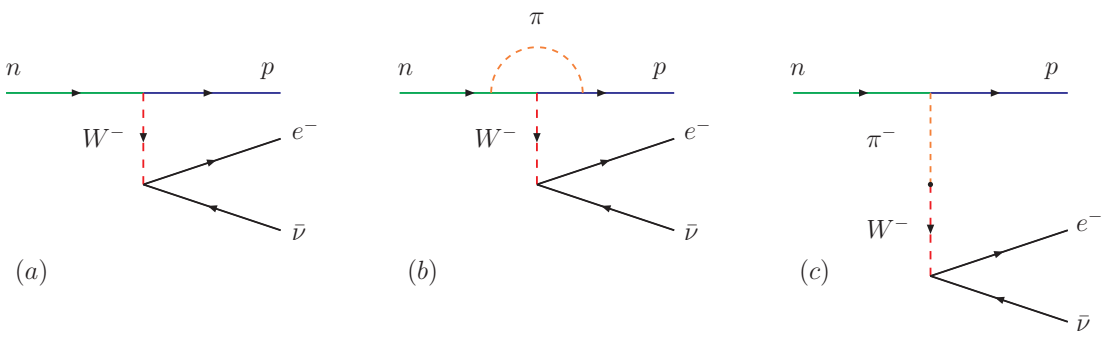

Figure 2.1: The origin of induced couplings can be motivated by imagining the neutron and proton as "bare" Dirac particles. The leading order beta decay amplitude is given by (a). The corrections to diagram (a) from pion loop (b) and pion exchange (c) are expected to contribute a large correction.

(L^ν) through the massive W^- boson propagator. At low momentum transfer, the matrix element is

$$\mathcal{M} = gH^\mu \left(\frac{g_{\mu\nu} - q_\mu q_\nu / M_W^2}{q^2 - M_W^2} \right) L^\nu = \frac{-g}{M_W^2} H^\mu L_\mu \tag{2.3}$$

where q_μ is the momentum transfer (≈ 1 MeV), g is the interaction coupling constant, M_W is the mass of the W^- gauge boson (≈ 100 GeV).

While the SM predicts a left-handed quark transformation, it occurs inside of real hadronic material in the presence of strong QCD interactions. These QCD interactions induce other vector and axial-vector couplings as a function of momentum transfer q^μ leaving a hadronic weak current that is not purely left-handed. The origin of this renormalization is made transparent by considering the neutron and proton as Dirac particles which interact with the W^- boson. It is expected that pion loop and pion exchange diagrams contribute a large correction to the "bare" neutron decay. These correction diagrams to the "bare" amplitude are shown in figure 2.1. These corrections are difficult to calculate, and it is useful to parameterize the current with form factors.

H^μ must include all the induced currents that transform as vectors and axial

vectors. The general hadronic weak interaction for any baryon to baryon semileptonic weak decay is

$$\begin{aligned} H^\mu \propto \bar{u}_p(p_p) \big[& f_1(q^2)\gamma^\mu + i f_2(q^2)\sigma^{\mu\nu}q_\nu + f_3(q^2)q^\mu \\ & - g_1(q^2)\gamma^\mu\gamma_5 - i g_2(q^2)\sigma^{\mu\nu}q_\nu\gamma_5 - g_3(q^2)q^\mu\gamma_5 \big] u_n(p_n) \\ & = V^\mu + A^\mu. \end{aligned} \tag{2.4}$$

The terms $\bar{u}_p$ and u_n are the proton and neutron spinors with 4-momentum p_p and p_n, respectively. The operators in the first line V^μ are those which transforms as a vector, and the operators in the second line A^μ are those which transform as axial vectors. Calculation of the form factors $f_i(q^2)$ and $g_i(q^2)$ is difficult, but symmetries of the underlying theory can be used to constrain the size of the form factors.

2.1.2 Symmetries of the weak interaction

QCD induces new interaction terms, so it is instructive to transform these weak bilinears with a QCD invariant transformation and examine the consequences. A G-parity transformation is formed by compounding a charge conjugation transformation and a π rotation about the isospin I_2 axis. On the isospin doublet $(n\,p)$, we have

$$\begin{pmatrix} p \\ n \end{pmatrix} \underrightarrow{\mathcal{G}} \begin{pmatrix} -\bar{p} \\ \bar{n} \end{pmatrix} \text{ where } \mathcal{G} = \mathcal{C}e^{i\pi I_2}. \tag{2.5}$$

QCD is invariant under a G-parity transformation (invariant for particles and anti-particles), but the weak bilinears transform differently from each other. The operator q^μ transforms under G-parity with a different sign from the γ^μ and $\sigma^{\mu\nu}q_\nu$ operators, while the operators $\sigma^{\mu\nu}q_\nu\gamma_5$ transforms with a different sign from the $\gamma^\mu\gamma_5$ and $q^\mu\gamma_5$ operators. Since γ^μ and $\gamma^\mu\gamma_5$ are the operators that exist before QCD induces new interactions, it is hypothesized that q^μ (f_3 term) and $\sigma^{\mu\nu}q_\nu\gamma_5$ (g_2 term) should be neglected. These neglected terms are known as second class currents, and they

generally require severely restricted field theories to implement. Searches for second class currents corroborate neglecting the terms [41, 42].

The conserved vector current hypothesis (CVC) restricts the renormalization of the vector terms V_μ. CVC assumes that the vector matrix element between hadronic states in the weak interaction are part of an isotriplet with the vector electromagnetic interaction. Therefore, conservation of the electromagnetic vector current can be generalized to all the vector currents in the isotriplet. It implies that

$$\partial_\mu V^\mu \rightarrow q_\mu V^\mu = 0. \tag{2.6}$$

Application of the conservation implies that $f_1(0) = 1$, and that $f_2(0)$ is related to the magnetic moment difference of the neutron (μ_n) and proton (μ_p). This term is the weak magnetism term, and $f_2(0) = (\mu_n - \mu_p)/2m_p$. Finally, CVC also requires the second class current $f_3(q^2) = 0$.

There exists an inexact symmetry for the axial vector currents A_μ. Calculation of the axial vector term $g_1(q^2)$ can be performed with the Adler-Weisberger relation, though the most precise value is derived from experimental data. Its experimental value is typically reported as

$$\lambda = \frac{g_1(0)}{f_1(0)}. \tag{2.7}$$

The axial vector current is only conserved in the massless pion limit. The partially conserved axial current hypothesis can be used to place a limit on $g_3(q^2)$. The effect of the bilinear in $g_3(q^2)$ is negligible at the energy scale of neutron beta decay.

2.1.3 Differential decay rate

Assuming the general weak interaction from equation 2.1, the differential decay rate can be solved for a spin polarized neutron to decay to a proton, electron, and

antineutrino. The leading result in nucleon mass is

$$\frac{d\Gamma}{dE_e d\Omega_e d\Omega_\nu} \propto |\mathbf{p_e}| E_e (E_0 - E_e)^2 \left(1 + a\frac{\mathbf{p_e}\cdot\mathbf{p}_\nu}{E_e E_\nu} + b\frac{m_e}{E_e} + \frac{\mathbf{J_n}}{|J_n|}\cdot\left[A\frac{\mathbf{p_e}}{E_e} + B\frac{\mathbf{p}_\nu}{E_\nu} + D\frac{\mathbf{p_e}\times\mathbf{p}_\nu}{E_e E_\nu}\right]\right). \tag{2.8}$$

The differential solid angle $d\Omega = d\cos\theta\, d\phi$ for both the electron and anti-neutrino, and the neutron polarization is represented by $\mathbf{J_n}$. The full expansion of the correlation coefficients a, b, A, B, and D is found in reference [17]. The result in [17] is general for any nuclear beta decay system, but equation 2.8 is appropriate for a spin 1/2 system.

The correlation coefficients in equation 2.8 can be simplified by incorporating the experimentally known structure of the weak interaction and by assuming the induced terms are small. Setting $f_1(q^2) = 1$ and $g_1(q^2) = \lambda$, the leading order results for the correlation coefficients can be calculated. Time-reversal violation can be incorporated by assuming a relative phase between the vector and axial vector coupling constant, i.e. $\lambda = |\lambda| e^{i\phi}$. With these simplifications, the correlation coefficients are

$$a = \frac{1 - |\lambda|^2}{1 + 3|\lambda|^2} \approx -0.1 \tag{2.9}$$

$$b = 0 \tag{2.10}$$

$$A = -2\frac{|\lambda|\cos\phi + |\lambda|^2}{1 + 3|\lambda|^2} \approx -0.1 \tag{2.11}$$

$$B = -2\frac{|\lambda|\cos\phi - |\lambda|^2}{1 + 3|\lambda|^2} \approx 1 \tag{2.12}$$

$$D = \frac{2|\lambda|\sin\phi}{1 + 3|\lambda|^2} \approx 0, \tag{2.13}$$

where the exact values can be found in [6].

Equations 2.9, 2.10, 2.11, 2.12, and 2.13 for the correlation coefficients represent the lowest order Standard Model (SM) neutron decay rate with a trivial extension to accommodate time-reversal violation (the SM does not have a leading order time-

reversal violation). This result neglects higher order contributions allowed in the SM, such as recoil order terms going as (q/m_n) or (m_e/m_n). The final state Coulomb interaction between the electron and proton are also neglected, but can be incorporated with the Fermi function. A precision measurement of the neutron lifetime (or correlation coefficients) must include these higher order contributions which are allowed in the SM.

Equation 2.8 provides a starting point for any neutron decay experiment when all the SM contributions have been taken into account. Test for new interactions are possible by measuring the correlation coefficients to high precision. These include scalar and tensor interactions, right-handed weak currents, and time-reversal. Review articles discuss the neutron's sensitivity to interactions beyond the SM and experimental data is used to place limits on them [22, 23, 24].

2.2 Neutron Lifetime and Radiative Corrections

All SM contributions must be understood to place limits on new interactions. In this section, the need for bremsstrahlung contributions to cancel the infinities in the higher order loop corrections is motivated. A discussion of an ideal neutron decay experiment motivates the comparison of the measured output to theoretical expectations. By combining the framework constructed in the last section with the higher order contributions, the current state the neutron lifetime is described.

2.2.1 Higher order contributions

A precise calculation of the neutron lifetime must include the transition of the neutron to every possible final state. Even when the final state is defined, there exist corrections due to virtual particle exchange loops. The simplest loops to describe are virtual photon exchange loops, but other heavy particles can be exchanged such as

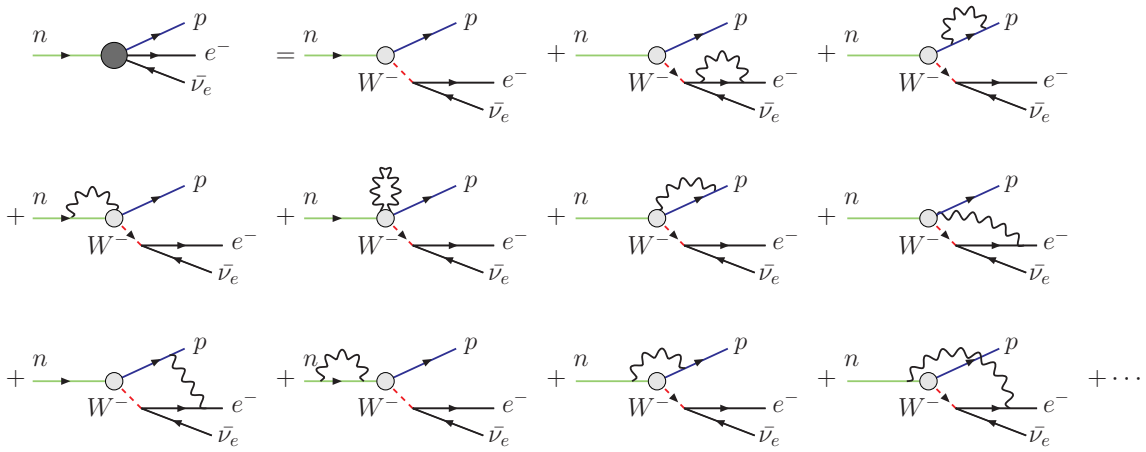

Figure 2.2: Single photon exchange loop diagrams that correct the tree-level neutron decay. The left-hand side with the dark circle represents the full sum of all corrections that maintain a proton, electron, and antineutrino in the final state. The first term on the right-hand side is the tree-level diagram while the remaining diagrams are the single photon exchange loop diagrams added coherently. The light circles are the parameterization of the weak vertex physics.

the Z, Higgs, or supersymmetric particles. A Feynman diagram expansion is made to describe the neutron decay branch to a proton, electron, and an antineutrino in the final state in figure 2.2. It is expanded to first order in the fine structure constant α or a single virtual photon exchange loop. The discussion is restricted to photons for clarity.

Calculating the virtual photon exchange loop diagrams yields infinite, negative corrections to the tree-level result. Tree-level, refers to the lowest order Feynman diagram with no virtual particle exchange loops. Tree-level calculations typically match experimental data well, and this implies is a cancellation of the infinities. Analogous to electron scattering, photon bremsstrahlung Feynman diagrams must be included to cancel the infinities from photon exchange loop diagrams [43].

The inclusion of photon bremsstrahlung Feynman diagrams must be done incoherently because the bremsstrahlung diagram has a different final state from diagrams in figure 2.2. The infinities cancel at each order in α after expanding the total contri-

bution of photon exchange loop diagrams and bremsstrahlung in the fine structure constant α. The result is a small, finite correction at each order of α, and this cancellation is a well known result from QED [44, 45, 46, 47].

2.2.2 Ideal experiment

It is useful to consider an ideal experiment before discussing the properties of the photons in the final state and radiative corrections. An ideal experiment is background free, has perfect energy resolution, and has perfect detection efficiency for all 4π solid angle for all particles. Furthermore, it is infinitely sensitive to photons above the detection threshold ω_t in all 4π solid angle. Therefore, the experiment registers a detected photon if its energy is above ω_t and no photon if its energy is less than ω_t. An experiment that registers only electrons and protons (and antineutrinos) requires all events have either no photons, or that all of the photons have energy less than ω_t. This is illustrated schematically in figure 2.3

The total measured decay rate Γ_{total} in figure 2.3 can be expanded in the number of final state photons. It is

$$\Gamma_{\text{total}} = \sum_{i=0}^{\infty} \Gamma_{ep\nu+i} \tag{2.14}$$

where i is the number of undetected photons in the final state. $\Gamma_{ep\nu+0}$ has been expanded into Feynman diagrams in figure 2.2. Matrix elements contributing to $\Gamma_{ep\nu+i}$ and $\Gamma_{ep\nu+j}$ can not be summed together for $i \neq j$ since the final states are different. If this result is expanded in α, the cancellations described in the last section can be applied here. This leads to a finite decay rate that is a function of the detection threshold ω_t.

The detection threshold ω_t in an ideal experiment can be so large that the experiment is not sensitive to photons. This situation describes the radiative corrections

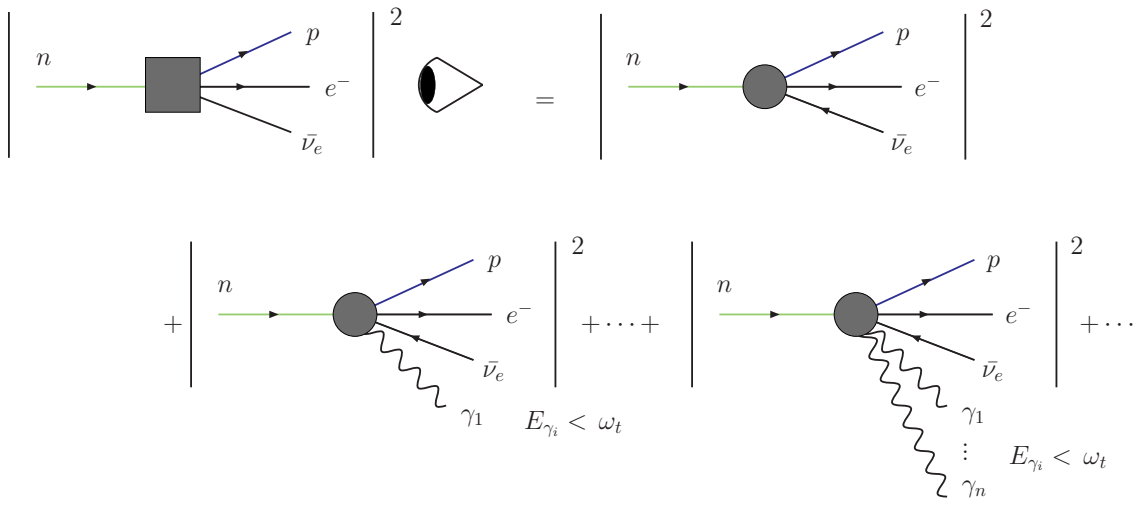

Figure 2.3: An experiment that is sensitive to photons with energy $E_\gamma > \Delta E$ registers no photons in the final state for these diagrams which represent total rates. The dark box on the left-hand side represents the full incoherent sum of rates in an experiment, while the dark circles are a coherent sum of matrix elements with the same final states. The matrix elements can not be added together since each final state is defined to have a different number particles.

to an ideal neutron beta decay experiment. In a real experiment, there may be some sensitivity to photons in the final state which requires knowledge of ω_t. Furthermore, a real experiment does not have perfect detection efficiency at all 4π solid angle. Any high precision experimental data must understand its sensitivity to ω_t as illustrated in figure 2.3 before trying to extract limits on new physics.

2.2.3 Radiative corrections

Returning to the question of bremsstrahlung, neutron decay can accommodate a photon in the final state through vertex emission and charged particle emission. The lowest order, single photon bremsstrahlung diagrams are shown in figure 2.4. Bremsstrahlung that couples to a charged particle exhibits a $1/\omega$ divergence as the photon's energy approaches 0. This is due to the pole that develops in the charged particle propagator as the initially virtual particle becomes real (equivalently, the propagator goes "on-shell"). A virtual electron emerging from the weak vertex with

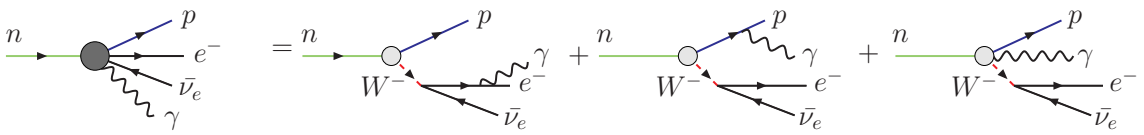

Figure 2.4: Feynman diagrams for photon bremsstrahlung. The left-hand side represents the sum of all single photons emerging from a neutron beta decay. The right-side specifies that the photon can emerge from virtual electrons, virtual protons, or emerge from the weak vertex.

4-momentum (p_e+k) emits a photon with 4-momentum k, leaving a real electron with 4-momentum p_e. The divergence in the virtual electron propagator as k approaches 0 is

$$\left.\frac{i(\not{p}_e+\not{k}+m_e)}{(p_e+k)^2-m_e^2+i\epsilon}\right|_{p_e^2=m_e^2} \rightarrow \left.\frac{i(\not{p}_e+\not{k}+m_e)}{p_e\cdot k+i\epsilon}\right|_{p_e^2=m^2} \rightarrow \infty\Big|_{k\rightarrow 0} \tag{2.15}$$

where ϵ is an infinitesimal number that moves the pole into the complex plane which aids in mathematical convergence. Also, $\not{a}=a_\mu\gamma^\mu$.

Photons emerging from the weak vertex, in general, do not couple to particles that go on-shell as photon momentum k goes to zero. The matrix element from vertex bremsstrahlung does not exhibit any divergence. Low [48], and later Adler and Dothan [49], use general principles to parameterize the matrix element for a bremsstrahlung process. The matrix element can be expanded in a power series in k,

$$\mathcal{M}=\frac{k^{\max}}{k}\left[\mathcal{M}_{-1}+\mathcal{M}_0\left(\frac{k}{m_n}\right)+\mathcal{M}_1\left(\frac{k}{m_n}\right)^2\right] \tag{2.16}$$

where the $\mathcal{M}_i$ are roughly the same order of magnitude. Vertex bremsstrahlung contributes to $\mathcal{M}_1$ and is suppressed. For photons near the endpoint energy ($\sim$ 1 MeV), the matrix element contribution from vertex bremsstrahlung is suppressed by $\sim 10^{-6}$ for powers of k^1.

The matrix element contributions $\mathcal{M}_{-1}$ and $\mathcal{M}_0$ are due to bremsstrahlung from external particles (the electron and proton). These matrix element contributions

can be derived from the non-radiative matrix element. Therefore, a low energy measurement is sensitive to the physics in the non-radiative matrix element. Vertex bremsstrahlung and any new physics associated with the photon contributes to the $\mathcal{M}_1$ (and at higher orders). This means that a search for new physics in the radiative decay mode should occur at higher energy because it has a shorter wavelength and is a deeper probe of new phenomenon.

The radiative corrections can be calculated for neutron beta decay, and an entire industry has been devoted to calculating these corrections for neutron beta decay. The integration of the correction diagrams can be divided into model independent and model dependent contributions. Sirlin [50] describes this division and shows that the corrections from the model independent piece are universal corrections to all beta decays. Sirlin [51] describes a current algebra formulation for calculating the model dependent corrections. The model independent infinities cancel when properly summed with the bremsstrahlung diagrams. The model dependent calculations are more difficult and do not benefit from well-established cancellations from QED. The model dependent corrections contribute the largest theoretical uncertainty to neutron radiative corrections. Within these model dependent corrections, the high energy photon regime of the γW box diagram shown in figure 2.5 is the largest source of the theoretical uncertainty [52].

2.2.4 Current state of the neutron lifetime

When all the corrections and decay branches have been summed, total neutron lifetime τ_n can be written [53]

$$\frac{\hbar}{\tau_n} = \frac{(m_e c^2)^5}{2\pi^3(\hbar c)^6}|V_{ud}|^2 G_F^2(1+\Delta_R)(1+3\lambda^2)f. \tag{2.17}$$

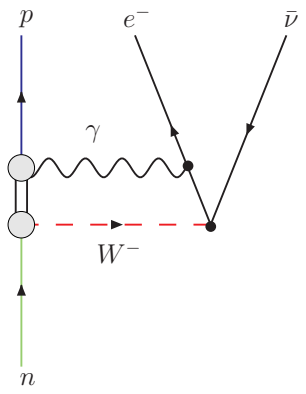

Figure 2.5: The γW box diagram that contributes the largest theoretical uncertainty to the neutron beta decay radiative corrections.

Neutron decay is normalized to the total muon decay rate through the Fermi coupling constant

$$G_F = (\hbar c)^3 \cdot 1.16637(1) \times 10^{-5}\,\mathrm{GeV}^2. \tag{2.18}$$

Any corrections common to neutron and muon decay are factored into G_F [52]. V_{ud} is the element of the Cabibbo-Kobayashi-Maskawa matrix which couples the weak eigenstate with the mass eigenstates in electroweak decay. The most precise extraction of V_{ud} is found from $0^+ \rightarrow 0^+$ superallowed nuclear decays [30] and is

$$V_{ud} = 0.97418 \pm 0.00026. \tag{2.19}$$

The total uncertainty is from nuclear structure, Coulomb distortions, and the uncertainty from loop effects [52]. The parameter λ can extracted from neutron decay angular correlation experiments. The Particle Data Group world average [6] is extracted from electron-neutron polarization correlation (A) measurements, and λ is

$$\lambda = -1.2695 \pm 0.029. \tag{2.20}$$

The phase space statistical factor includes the effect of the Fermi function and other small nucleon mass, size, and recoil corrections yielding [53]

$$f = 1.6887. \tag{2.21}$$

Finally, Δ_R is the effect of electroweak radiative corrections, and m_e is the electron mass.

To $\mathcal{O}(\alpha)$, the corrections contained in Δ_R are

$$\Delta_R = \frac{\alpha}{2\pi}\left[g(E_e) + 4\ln\frac{m_Z}{m_p} + \ln\frac{m_p}{m_A} + A_g + 2C_{\text{Born}}\right] \tag{2.22}$$

where $g(E_e)$ is Sirlin's universal function for the long-distance, model-independent and bremsstrahlung corrections [50]. This term represents the correction that remains when the infinite model independent parts of the photon exchange loop diagrams are cancelled by the IB. The second term is a short distance vector current loop effect with m_p the proton mass and m_Z the Z boson mass. The final three terms are weak axial vector contributions and are dominated by the γW box diagram. Terms $\ln m_p/m_A$ and A_g are the intermediate and short range axial-vector loop effects with $m_A = 1.2$ GeV the approximate mass of the A_1 meson and $A_g \approx -0.34$. The final term, $C_{\text{Born}} \approx 0.829$, is the long distance axial-vector current loop contribution. All the contributions taken together with the Fermi function correction to f imply a 9.37% $\mathcal{O}(\alpha)$ correction to τ_n [52, 53].

2.3 Radiative Decay Matrix Element and Decay Rate

In the previous section, the radiative decay mode of the neutron was considered as a way to cancel infrared divergences from photon exchange loop diagrams that are higher order corrections to neutron decay. These corrections are integrated and no treatment is given to angular correlations. This section treats the radiative beta decay mode as a fundamental decay process, and systematically derives the differential decay rate. A classical discussion is helpful in order to understand the radiative decay process before a field theory calculation is undertaken. First, it is instructive to consider an ideal radiative decay experiment.

2.3.1 Ideal radiative decay experiment

The ideal experiment from section 2.2.2 is considered here, and now the final state of is an electron, proton (and antineutrino), and a single photon. This experiment is shown schematically in figure 2.6. This figure has also been expanded in the number of photons in the final state. The decay rate is,

$$\Gamma_{\text{total}} = \sum_{i=0}^{\infty} \Gamma_{ep\nu\gamma+i} \tag{2.23}$$

where i is the number of undetected photons in the final state. An expansion in α illustrates that the infinities from higher multiplicity photon diagrams cancel with higher order photon exchange loop diagrams. Therefore, the Feynman diagrams in figure 2.4 are the leading contribution.

While the ideal, non-radiative decay experiment can set a threshold high enough to be insensitive to photons (effectively integrating over the entire photon energy spectrum), a radiative decay experiment is sensitive to photons with energy from threshold ω_t to a maximum energy $\omega_{\max}$. A precision measurement of $d\Gamma_{\text{tot}}/d\omega_t$ or $d\Gamma_{\text{tot}}/d\omega_{\max}$ can investigate these cancellations directly. Of these leading order diagrams, the electron bremsstrahlung is expected to be dominant due to its light mass. The remainder of this section derives the differential decay rate, at first classically, and then with field theory.

2.3.2 Classical treatment

Classically, the beta decay process can be thought of as a high energy electron being generated at the origin at time $t = 0$ with velocity $\boldsymbol{v} = c\boldsymbol{\beta}$ where c is the speed of light. The radiative decay requires this electron to be followed by a photon of energy $\hbar\omega$. The radiative decay transition

$$n \to p^+ + e^- + \bar{\nu_e} + \gamma \tag{2.24}$$

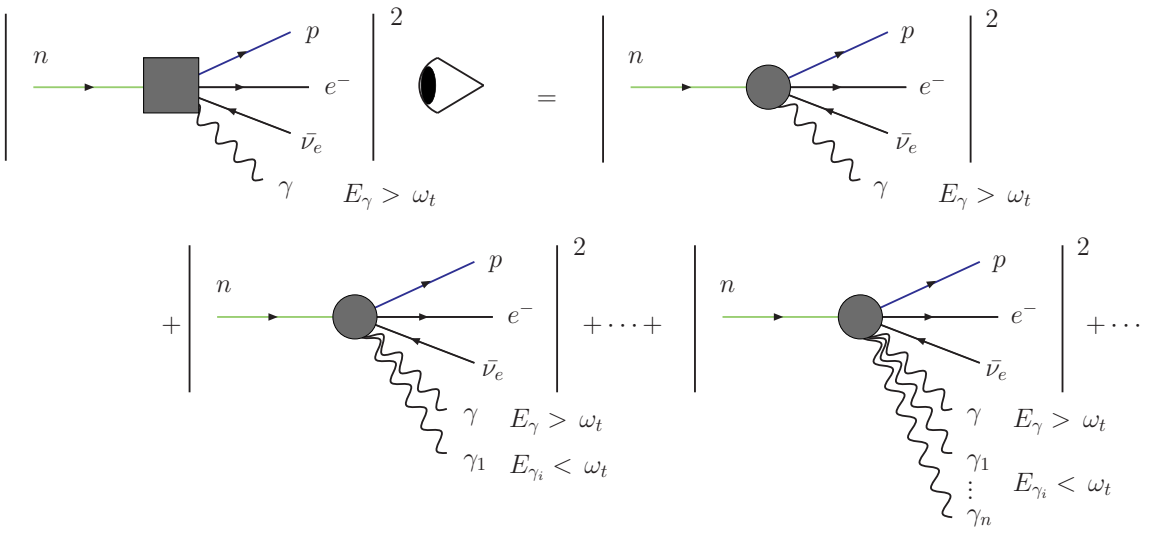

Figure 2.6: An experiment that is sensitive to photons with energy $\omega > \omega_t$ sees only a single photon in the final state for the following configurations. The matrix elements can not be added together since each final state is different. The dark box on the left-hand side is the incoherent sum of rates in an experiment, while the dark circles are a coherent sum of matrix elements with the same final states. An expansion in α results in small corrections due to canceling infinities.

conserves angular momentum since the photon has spin $J_\gamma = 1$ and the neutron, proton, electron, and antineutrino have spin 1/2. This allows dipole radiation to be the dominant contribution. Parity violation requires this radiation to be an incoherent sum of $E1$ and $M1$ radiation. This process leaves the photon circularly polarized, and near the photon energy endpoint, the polarization is fully left-handed [54]. The helicity transfer from the electron to the photon is discussed further in section 2.4.

The differential photon intensity spectrum as a function of photon solid angle $d\Omega_\gamma$ and photon frequency $d\omega$ for a given electron velocity β is [55],

$$\frac{d^2 I}{d\omega_\gamma d\Omega} = \frac{e^2}{4\pi^2 c} \frac{\beta^2 \sin^2 \theta_{e\gamma}}{(1 - \beta \cos \theta_{e\gamma})^2} \tag{2.25}$$

where $\theta_{e\gamma}$ is defined as the angle between the emitted photon and electron. The numerator $\sin^2 \theta$ is typical for dipole radiation, and the denominator $(1 - \beta \cos \theta)$ accounts for retardation effects from relativistic electrons. By integrating over solid

angle and using $N(\hbar\omega)\,\hbar\omega\,d(\hbar\omega) = I(\omega)d\omega$ as the conversion from intensity to number of photons, the number of photons in a unit energy region is,

$$N(\hbar\omega) = \frac{\alpha}{\pi}\left(\frac{1}{\hbar\omega}\right)\left[\frac{1}{\beta}\ln\left(\frac{1+\beta}{1-\beta}\right) - 2\right]. \tag{2.26}$$

Here β is a parameter that should be averaged over the entire electron spectrum to generate the classical radiation distribution.

Knipp and Uhlenbeck [34] and Bloch [35] applied QED as a perturbation to Fermi's weak theory of beta decay. Both treatments use Fermi's theory to calculate the decay matrix element that makes a transition to an arbitrary electron state. This arbitrary electron states actually both spin states of the electron and positron. The positron states are useful in understanding radiative decay in atomic matter with bound electron states (radiative electron capture). QED is then used to calculate the transition from this arbitrary electron / positron state to the physically observable electron and a quantum of light. These treatments are consistent with each other, and predict many of qualitative features of radiative decay. The total radiative decay rate [35] is

$$\frac{d\Gamma}{d\omega d\Omega dE_e} = A\frac{E_{\bar{\nu}}^2}{\omega}\frac{\beta}{(1-\beta\cos\theta)^2}\left[(\hbar\omega)^2(1-\beta\cos\theta) + E_e(E_e+\hbar\omega)\beta^2\sin^2\theta\right] \tag{2.27}$$

where factor A is given in equation 16 of Bloch's treatment. A includes the effects of the weak interaction coupling constant G_F, the fine structure constant α, and the wavefunction overlap of the resulting proton with the initial neutron. This overlap is complete for the neutron and mirror nuclei, but it is generally incomplete for arbitrary nuclear systems [56]. As the photon energy ($\hbar\omega$) goes to zero, deviations from the classical result in equation 2.25 can be attributed to the inclusion of Fermi's theory of weak interactions.

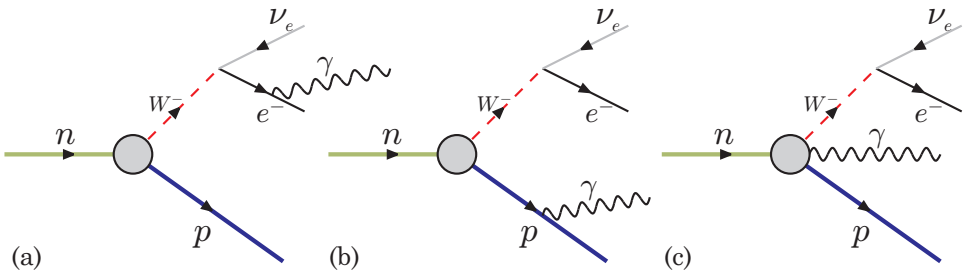

Figure 2.7: Feynman diagrams for radiative decay, (a) electron bremsstrahlung, (b) proton bremsstrahlung, and (c) bremsstrahlung from weak vertex.

2.3.3 Field theory treatment

In this section, the Feynman diagrams for photon IB can be solved in a relativistically covariant way with quantum field theory. Then, the matrix element for electron and proton bremsstrahlung is derived. Section 2.2.3 motivated that it is the dominant contribution while vertex bremsstrahlung is negligible. The leading order differential decay rate for an unpolarized neutron is calculated, and a survey of the calculation techniques is given.

The Feynman diagrams for the radiative decay process are shown in figure 2.7. The first two diagrams are IB from the electron and proton and can be calculated with QED [57, 58, 59]. The QED matrix element for an unpolarized neutron decaying to a proton, electron, anti-neutrino and a single photon is

$$\begin{aligned}\mathcal{M} = i\frac{eg_V}{\sqrt{2}}\Bigg[&\bar{u}_e\left(\frac{2p_e\cdot\epsilon^* + \not{\epsilon}^*\not{k}}{2p_e\cdot k}\right)\gamma_\mu(1-\gamma_5)v_{\bar{\nu}}\bar{u}_p\gamma^\mu(1+\lambda\gamma_5)u_n \\ &-\bar{u}_e\gamma_\mu(1-\gamma_5)v_{\bar{\nu}}\bar{u}_p\left(\frac{2p_p\cdot\epsilon^* + \not{\epsilon}^*\not{k}}{2p_p\cdot k}\right)\gamma^\mu(1+\lambda\gamma_5)u_n\Bigg]\end{aligned} \tag{2.28}$$

where the explicit momentum dependence of the spinors has been suppressed. The photon polarization 4-vector ϵ is transverse to the photon momentum, $k\cdot\epsilon = \mathbf{k}\cdot\epsilon = 0$. This matrix element incorporates no physics beyond the SM.

The electron bremsstrahlung diagram dominates due the light mass of the electron. Its dominant contribution is inversely proportional to photon energy $(1/\omega)$. When

squaring the matrix element, the rate due to the interference term is reduced by approximately (m_e/m_p). The proton contribution also has a $1/\omega$ bremsstrahlung spectrum, though its rate is reduced by approximately $(m_e/m_p)^2$. Bremsstrahlung from the weak vertex is model dependent and, by Low's theorem, is negligible.

Using heavy baryon chiral perturbation theory (HBχPT), an explicit calculation has been performed by Bernard et al. [60, 61] which includes diagrams occurring at next to leading order ($\mathcal{O}(m_e/m_N)$) including explicit Δ degrees of freedom. HBχPT is an effective field theory which utilizes the symmetries of QCD to integrate over the high momentum quark degrees of freedom to calculate meson and heavy baryon couplings. It is a choice of model to calculate model dependent corrections and vertex bremsstrahlung. By including all next to leading order contributions (proton bremsstrahlung, vertex bremsstrahlung, weak magnetism, and recoil order terms), the total contributions of the higher order corrections is $\mathcal{O}(0.5\%)$.

The leading order differential decay rate for the matrix element in equation 2.28 can be solved, and neglecting recoil order terms, differential decay rate is

$$\begin{aligned}(2.29)\qquad \frac{d\Gamma}{dE_e d\omega d\Omega_e d\Omega_{\bar{\nu}} d\Omega_\gamma} &= -\alpha \frac{g_V^2 |\mathbf{p_e}| E_{\bar{\nu}} \omega}{(2\pi)^7}(1+3|\lambda|^2) \times \\ &\left[E_{\bar{\nu}}\left(\frac{1}{\omega}+\frac{E_e}{\omega^2}+\frac{m_e^2(E_e+\omega)}{(p_e\cdot k)^2}-\frac{(2E_e+\omega)}{(p_e\cdot k)}-2\frac{E_e^2}{(p_e\cdot k)\omega}\right)\right. \\ &\left. + a\mathbf{p}_{\bar{\nu}}\cdot\left(\frac{\mathbf{p_e}}{\omega^2}+m_e^2\frac{(\mathbf{p_e}+\mathbf{k})}{(p_e\cdot k)^2}-\frac{(\mathbf{p_e}+\mathbf{k})}{(p_e\cdot k)}-E_e\frac{(2\mathbf{p_e}+\mathbf{k})}{(p_e\cdot k)\omega}\right)\right] \\ &= \alpha g_V^2(1+3\lambda^2)\left[f_1(X)+a f_2(X)\right].\end{aligned}$$

X represents the 8 kinematic variables, electron energy and direction E_e and Ω_e, photon energy and direction E_γ and Ω_γ, and the neutrino direction Ω_ν. A direction Ω is ϕ and $\cos\theta$. The correlation coefficient a is defined the same as for non-radiative decay in equation 2.9. The calculation of the leading order functions $f_i(X)$ has been performed and agrees with those calculated in references [57, 60, 61]. This result is

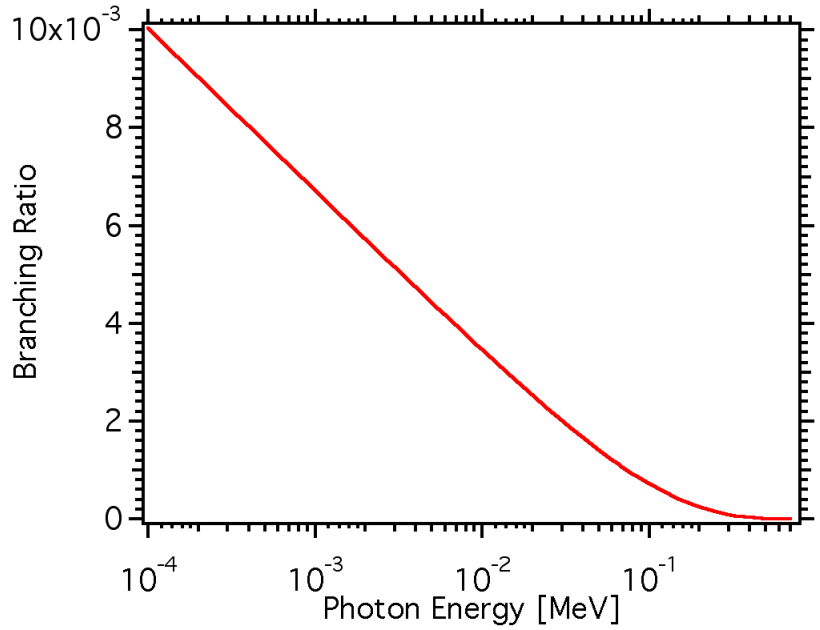

Figure 2.8: Branching ratio for photon production above the specified energy to the photon energy endpoint. This result is from a numerical integration of equation 2.29.

central to the Monte Carlo simulation described in chapter V. Equation 2.29 can be integrated to give the branching ratio for photon production for a given energy to the endpoint energy. This was done numerically, and the result is shown on a log plot in figure 2.8

Equation 2.29 is the lowest order result, and it can be calculated in a standard way as outlined in any quantum field theory text [43]. The photon polarization sum can be calculated in two ways. The first method explicitly defines the photon polarization vectors ϵ_μ, and the photon polarization sum is done directly. For a photon with energy ω and 3-momentum $\mathbf{k}$ in the $+z$ direction, the four momentum is $k^\mu = (\omega, 0, 0, |\mathbf{k}|)$. The circular polarization 4-vectors are $\epsilon^\mu_\pm = (0, 1, \pm i, 0)/\sqrt{2}$. The light mass of the electron implies that this sum only requires the electron bremsstrahlung diagram in figure 2.7 (the first term in equation 2.28). This procedure yields the correct answer to leading order. This method is useful for calculating the photon polarization in section 2.5.

The second method is to use the photon polarization sum rule from QED [43],

$$\sum_i \epsilon_i^{\mu *} \epsilon_i^{\nu} \rightarrow -g^{\mu\nu}. \tag{2.30}$$

The proton bremsstrahlung matrix element scales as $1/m_p$ (versus $1/m_e$ for the electron bremsstrahlung) due to the $(p_p \cdot \epsilon)/(2p_p \cdot k)$ term in the matrix element in equation 2.28. It is expected that when the matrix element is squared, the proton should contribute $\mathcal{O}(1/m_p^2)$. When the photon polarization sum rule is applied, the proton amplitude is an $\mathcal{O}(1)$ contribution, but an incorrect result is found when applying this formalism to only the electron bremsstrahlung diagram.

The QED sum rule must be applied to both the electron and proton bremsstrahlung diagrams to reproduce the explicit polarization vector sum. The resolution is that the gauge invariance procedure requires a gauge invariant set of diagrams. The photon couples to all external charged particles by charge conservation, and both electron and proton bremsstrahlung diagrams are required to reproduce the correct result. This was noticed by and commented upon in Bernard et al. [60].

2.4 Correlation Coefficients in Radiative Decay

The angular correlation coefficient a occurs in the radiative differential decay rate, and this system provides a new way to measure it. Extracting the same parameter from both radiative and non-radiative decays could result in different numeric values due to differing higher-order corrections (see figures 2.3 and 2.6). The angular correlation coefficient a is used as an example. Finally, more angular correlation coefficients arise when a polarized neutron is considered.

2.4.1 Parameter measurements

Any parameter extracted from a neutron beta decay experiment is a result of inputs at the Lagrangian level. Let λ be the experimentally extracted parameter,

and let λ_0 be the input into the Lagrangian. In fact, $\lambda_0 = -1$ at the quark level of QCD.

A non-radiative decay process occurs at $\mathcal{O}(1)$ in α, and its radiative corrections occur at $\mathcal{O}(\alpha)$. This measurement is then corrected by all the diagrams in figure 2.2. Furthermore, because the non-radiative experiment is insensitive to photons (ideally), it integrates over the entire photon spectrum without regard for a photon detection threshold ω_t. An experiment that is sensitive to photons in the final state occurs at $\mathcal{O}(\alpha)$, and its radiative corrections occur at $\mathcal{O}(\alpha^2)$. This experiment is now sensitive to the threshold ω_t, and the radiative corrections are now a function of ω_t. There is no reason to assume that λ extracted from radiative and non-radiative neutron decay experiments should be the same because of potentially different radiative corrections.

The differences in radiative corrections are expected to be very small (there is no current calculation of the of the corrections to radiative decay) so it is useful to consider a radiative decay extraction of a. The method of extracting a from equation 2.8 can be generalized to radiative decay, and it is described below.

Extracting a from equation 2.8 requires sensitivity to $\mathbf{p_e} \cdot \mathbf{p}_{\bar{\nu}}/E_{\bar{\nu}}E_e$. With 4-vectors,

$$(p_e + p_{\bar{\nu}})^2 = m_e^2 + 2p_e \cdot p_{\bar{\nu}} = m_e^2 + 2E_eE_{\bar{\nu}} - 2\mathbf{p_e} \cdot \mathbf{p}_{\bar{\nu}} \tag{2.31}$$

since $m_{\bar{\nu}}^2 = 0$. Conservation of momentum can be applied to the left-hand side, and in the neutron rest frame,

$$(p_e + p_{\bar{\nu}})^2 = (p_n - p_p)^2 = m_n^2 + m_p^2 - 2m_nE_p. \tag{2.32}$$

Combining these equations, the correlation term is,

$$\begin{aligned} \frac{\mathbf{p_e} \cdot \mathbf{p}_{\bar{\nu}}}{E_eE_{\bar{\nu}}} &= 1 - \frac{1}{2E_eE_{\bar{\nu}}}\left(m_n^2 + m_p^2 - m_e^2 - 2m_nE_p\right) \\ &= 1 - \frac{2m_n\left(E_p^{\max} - E_p\right)}{2E_eE_{\bar{\nu}}} \end{aligned} \tag{2.33}$$

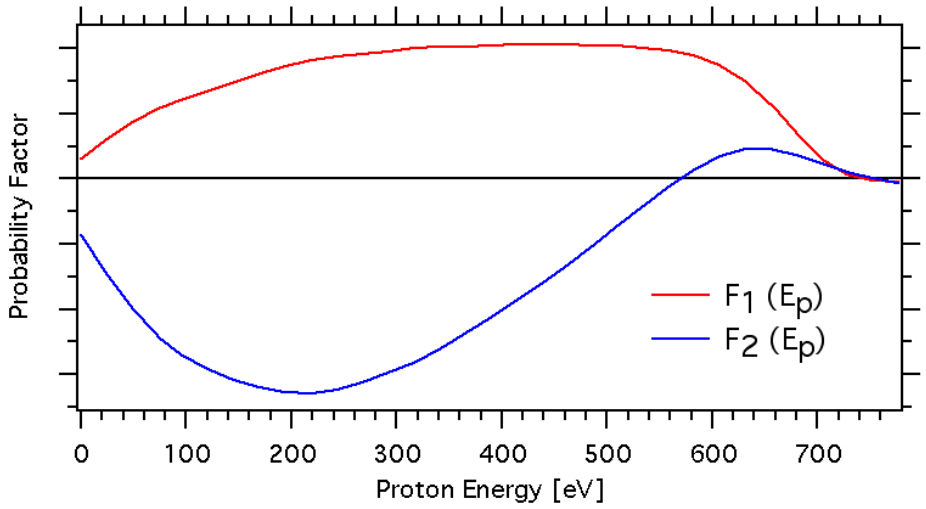

Figure 2.9: The proton energy dependence of $F_1(E_p)$ and $F_2(E_p)$. The terms are integrated over all variables but proton energy in Monte Carlo.

The denominator $E_e E_{\bar{\nu}}$ isn't an explicit singular function of the proton energy / momentum, but there is a strong correlation with proton energy. Therefore, an experiment that is sensitive to proton energy is a candidate for a a measurement.

In equation 2.29, the a term is not simply $\mathbf{p_e} \cdot \mathbf{p}_{\bar{\nu}} / E_{\bar{\nu}} E_e$, but it is a function of other angular correlations. It is still sensitive to proton energy, and equation 2.29 can be integrated over all variables and cast as a function of proton energy

$$F_i(E_p) = \frac{d}{dE_p} \int dX \, f_i(X). \tag{2.34}$$

Figure 2.9 shows that the functions $F_1(E_p)$ and $F_2(E_p)$ from equations 2.29 and 2.34 vary with proton energy. The full proton spectrum $F(E_p)$ is created from the combination $F(E_p) = F_1(E_p) + aF_2(E_p)$. The figure also demonstrates the distinctiveness of the spectra shapes. This allows a least squares fit to be used to extract a from a proton energy spectrum without knowing the electron and neutrino momenta to reconstruct $\mathbf{p_e} \cdot \mathbf{p}_{\bar{\nu}} / E_e E_{\bar{\nu}}$. This method has been used to measure a in non-radiative neutron decay [62, 63].

2.4.2 Polarized neutron radiative decay

Other correlation coefficients at leading order can measured by introducing the neutron spin polarization. To incorporate the neutron spin polarization $\mathbf{J_n}$, the neutron spinor u_n is modified,

$$u_n \to (1+\gamma_5 \not{J}_n)u_n. \tag{2.35}$$

For polarization in the $+z$ direction, the polarization 4-vector is $J_n^\mu = (0,0,0,1)$. The decay rate is modified by the neutron polarization $\mathbf{J_n}$ and is

$$\begin{aligned}
\frac{d\Gamma}{dE_e d\omega d\Omega_e d\Omega_{\bar\nu} d\Omega_\gamma} &= -\alpha \frac{g_V^2 |\mathbf{p_e}| E_{\bar\nu}\omega}{(2\pi)^7}(1+3|\lambda|^2)\times \\
&\left(E_{\bar\nu}\left(\frac{1}{\omega}+\frac{E_e}{\omega^2}+\frac{m_e^2(E_e+\omega)}{(p_e\cdot k)^2}-\frac{(2E_e+\omega)}{(p_e\cdot k)}-2\frac{E_e^2}{(p_e\cdot k)\omega}\right)\right. \\
&+a\mathbf{p}_{\bar\nu}\cdot\left(\frac{\mathbf{p_e}}{\omega^2}+m_e^2\frac{(\mathbf{p_e}+\mathbf{k})}{(p_e\cdot k)^2}-\frac{(\mathbf{p_e}+\mathbf{k})}{(p_e\cdot k)}-E_e\frac{(2\mathbf{p_e}+\mathbf{k})}{(p_e\cdot k)\omega}\right) \\
&\frac{\mathbf{J_n}}{|J_n|}\cdot\left[A\mathbf{p_e}E_{\bar\nu}\left(-\frac{1}{\omega^2}-\frac{m_e^2}{(p_e\cdot k)^2}+\frac{1}{(p_e\cdot k)}+\frac{2E_e}{(p_e\cdot k)\omega}\right)\right. \\
&+B\mathbf{p}_{\bar\nu}\left(\frac{1}{\omega}+\frac{E_e}{\omega^2}+\frac{m_e^2(E_e+\omega)}{(p_e\cdot k)^2}-\frac{(2E_e+\omega)}{(p_e\cdot k)}-\frac{2E_e^2}{(p_e\cdot k)\omega}\right) \\
&+A\mathbf{k}E_{\bar\nu}\left(-\frac{m_e^2}{(p_e\cdot k)^2}+\frac{1}{(p_e\cdot k)}+\frac{E_e}{(p_e\cdot k)\omega}\right) \\
&+D(\mathbf{p_e}\times\mathbf{p}_{\bar\nu})\left(-\frac{1}{\omega^2}-\frac{m_e^2}{(p_e\cdot k)^2}+\frac{1}{(p_e\cdot k)}+\frac{2E_e}{(p_e\cdot k)\omega}\right) \\
&\left.\left.+D(\mathbf{p}_{\bar\nu}\times\mathbf{k})\left(\frac{m_e^2}{(p_e\cdot k)^2}-\frac{1}{(p_e\cdot k)}-\frac{E_e}{(p_e\cdot k)\omega}\right)\right]\right) \\
&= (1+3\lambda^2)\left[f_1(X)+af_2(X)\right. \\
&+\mathbf{J_n}\cdot(Af_3(X)\mathbf{p_e}+Bf_4(X)\mathbf{p}_{\bar\nu}+Af_5(X)\mathbf{k} \\
&\left.+Df_6(X)(\mathbf{p_e}\times\mathbf{p}_{\bar\nu})+Df_7(X)(\mathbf{p}_{\bar\nu}\times\mathbf{k}))\right],
\end{aligned} \tag{2.36}$$

where the new correlation coefficients A, B, and D are defined in the same way as non-radiative decays 2.11, 2.12, and 2.13. Aside from generalizing λ to accommodate time-reversal violation, this result does not incorporate physics beyond the SM. The

original angular correlations from equation 2.8 exist with modifications for the photon in the final state. The new photon-neutron spin correlation is proportional to A because the photon originates from electron bremsstrahlung at leading order. A new time-reversal violation term $\mathbf{J_n} \cdot (\mathbf{p}_{\bar{\nu}} \times \mathbf{k})$ is now present that correlates the antineutrino-photon-neutron spin.

2.5 Photon Polarization

In section 2.3.2, it was stated that near the photon endpoint energy, the electron's helicity is completely transfered. The polarization of the photon at leading order is easily calculated explicitly with $\epsilon_{\pm}$. By letting $d\Gamma_+(\omega)$ and $d\Gamma_-(\omega)$ be the decay rate for a left- and right- handed photon to be emitted as a function of photon energy ω, the photon polarization P_γ is

$$P_\gamma(\omega) = \frac{d\Gamma_+(\omega) - d\Gamma_-(\omega)}{d\Gamma_+(\omega) + d\Gamma_-(\omega)}. \tag{2.37}$$

The polarization can be calculated numerically, and this result is shown in figure 2.10. The photon polarization approaches -1 as the photon energy approaches the endpoint, and this result was first calculated by Bernard *et al.* [60, 61]. The analytic, leading order result for $d\Gamma_\pm/dX$ is given in Appendix A.

The photon polarization can be measured near the photon energy endpoint to measure the effect of right-handed currents ($V + A$). In a completely right-handed interaction, the photon polarization in figure 2.10 is flipped by a sign. IA small admixture χ of right-handed currents can be introduced in the leptonic current, and it is

$$\gamma_\mu(1-\gamma_5) \rightarrow \gamma_\mu(1-\gamma_5) + \chi\gamma_\mu(1+\gamma_5). \tag{2.38}$$

Because the left-handed and right-handed pieces do not interfere, the measured photon polarization is scaled by $(1-\chi^2)$ from figure 2.10. A measurement of the photon

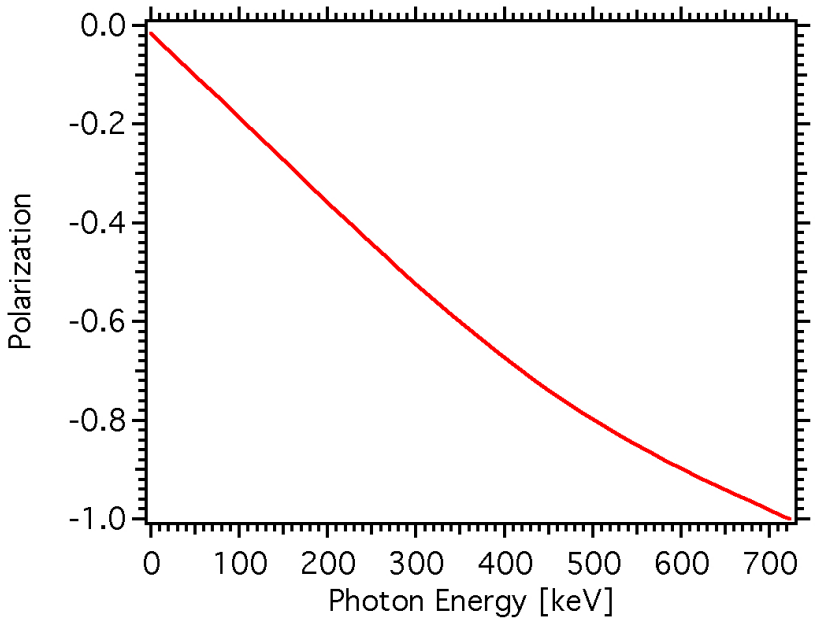

Figure 2.10: The photon polarization as a function of emitted photon energy. The photon polarization is left-handed at the photon energy endpoint.

polarization can thus set a limit on right-handed currents.

CHAPTER III

Experimental Setup

To observe radiative decay, the high energy photon must be observed and correlated to a neutron decay. Conceptually, a photon singles experiment could be performed, but it would suffer from a severe background rate in any real experiment. The approach of this experiment is to correlate the photon with the observed electron and proton. Beta decay has been observed for quite some time, and the dearth of evidence for radiative neutron decay is due to the complications a photon measurement entails.

In section 3.1, the difficulties of measuring radiative decay are discussed. A description of the experiment's mode of operation is also given. Section 3.2 discusses the production and delivery of the neutron beam to the experimental apparatus. Section 3.3 describes the detection of the charged particles, and section 3.4 describes the unique photon detector employed in the experiment. Section 3.5 describes the unique data acquisition system which utilizes recorded oscilloscope waveform data over traditional nuclear counting techniques.

3.1 General Description

The observation of radiative decay must overcome several difficulties. The neutrons produced at the neutron source have a low probability of decaying inside the

apparatus because the neutron lifetime is nearly 15 minutes. A large number of neutrons are required to attain an appreciable decay rate within the experimental apparatus. A large experimental decay region with slow neutrons also maximizes the decay probability. Related to the long neutron lifetime is the rarity of the radiative decay mode to produce observable, high energy photons. The branching ratio to produce photons above 15 keV in energy is approximately 3×10^{-3}, and this low photon production rate must be distinguished from the high rate of background photons characteristic of neutron production facilities. These background photons are produced by neutron capture and activation of the surrounding materials.

An experiment to measure the radiative decay mode of the free neutron commenced in January of 2004 and operated until November of 2005 at the National Institute of Standards and Technology (NIST) in Gaithersburg, Maryland. To distinguish radiative decay photons from uncorrelated background photons, the photon was correlated with the electron and proton in a triple coincidence measurement. The neutron beam was sent through the long bore of a superconducting magnet where the strong magnetic fields constrain the charged particle motion to cyclotron orbits. The decay region is large (approximately 0.5 m in length) which increases the decay probability. The charged particles undergoing cyclotron motion are guided to the charged particle detector which is discussed in section 3.3.

The detection of photons must reject the background photons while maximizing the detection efficiency for correlated radiative decay photons. A large area photon detector is required to maximize the solid angle for photon detection because the photons are unaffected by the magnetic field. The chose of photon detector also maximizes the photon energy range which the detector is sensitivity. The detector must also optimize its timing resolution to distinguish correlated, radiative decay

photons from uncorrelated, background photons. A detailed description of the photon detector and its components is given in section 3.4.

3.2 Neutron Beam Line

The radiative beta decay experiment was operated at the endstation of the NG-6 cold neutron beam line at the NIST Center for Neutron Research (NCNR) [64]. The previous experiment on this beam line was the second run of the emiT experiment to measure the D coefficient in neutron beta decay as a test of time-reversal violation [66, 65]. Most of the components from the emiT experiment were retained for the radiative decay experiment. This section describes the production and transport of neutrons from the NCNR research reactor to the experimental apparatus through the emiT beam line.

The NCNR operates a 20 MW split-core research reactor providing fission neutrons at both thermal and cold energies. Cold neutrons are those that have a kinetic energy corresponding to temperatures less than 60 K. The high energy neutrons from fission reactions are thermally moderated with heavy water (D_2O) in the reactor coolant. An ellipsoid cold source filled with 20 K liquid hydrogen further cools the thermal neutrons to roughly 40 K [67]. While the neutrons don't completely thermalize with the 20 K liquid hydrogen, they do attain a roughly Maxwellian distribution. Figure 3.1 shows a measurement of the cold neutron spectrum entering the NG-6 experiment area. This measurement was performed with a time of flight procedure and is detailed in C.E.H. Mattoni's thesis [2]. The spectrum is peaked for a neutron velocity of approximately 1000 m/s or equivalently, 4 $\mathring{A}$. The large number of cold neutrons exit the reactor beamport and are transported through the cold neutron guides towards the experiment.

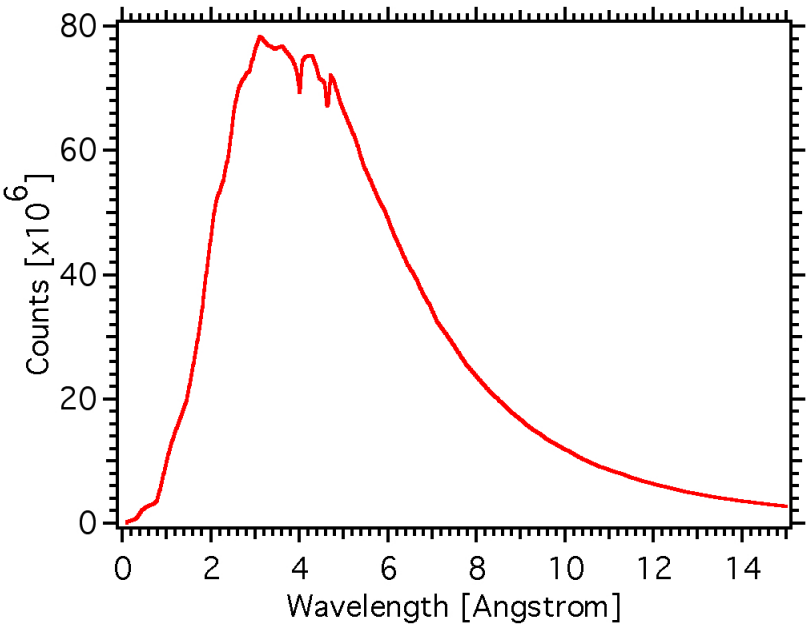

Figure 3.1: The cold neutron spectrum entering the experiment's beam line. This spectrum was from a time of flight measurement, the details of which are found in C.E.H. Mattoni's thesis [2].

^{58}Ni coated neutron guides with an area of 6 cm $\times$ 15 cm transport the cold neutrons from the cold source to the apparatus which is 60 m downstream. The neutron wavelength is approximately 4 $\mathring{A}$, and when it scatters from the ^{58}Ni by a spin-spin interaction, it interacts with many nuclei because of its long wavelength. The neutron's interaction can be approximated by Fermi pseudopotential $V = (2\pi\hbar/m_n)Na_c$ where m_n is the mass of the neutron (939.565 MeV), N is the number density of scattering nuclei, and a_c is the coherent scattering length for the neutron on the scattering nuclei. The neutron trajectory can be modeled with geometric optics with an index of refraction of the scattering material

$$n = \sqrt{1 - \lambda^2 N a_C/\pi} \tag{3.1}$$

where λ is the wavelength of the incoming neutron. For ^{58}Ni, $a_c = 14$ fm and $N = 6.59$ cm^3 mol^{-1} implying $n < 1$. The critical angle for total external reflection within the neutron guide is $\theta_c = 2$ milliradians per Angstrom. Even for a beam of

well collimated neutrons satisfying the total external reflection condition, there are still transport losses due to imperfections in the specular reflections [68].

The neutron beam exits the ^{58}Ni guides and passes through a thin Mg window. It continues through 79 cm of air to a beam-reducing, cylindrical aperture which is 6 cm in diameter. The local neutron beam shutter for the NG-6 endstation is located at this point and 1 m of air follows. The beam then enters a cryogenically cooled, 15 cm thick beam filter constructed from blocks of single-crystal bismuth. This filter scatters the fast neutrons out of the beam and absorbs the background photons from the reactor. Cooling the filter suppresses losses from cold neutron - phonon scattering.

The beam passes through a 5.08 cm diameter Li-glass collimator C0 before entering 2 m of Be-coated neutron guide tube (see figure 3.2). The guide tube has an over-pressure of helium gas to prevent neutron scattering in air, and this tube is sealed at each end by 0.5 mm thick single-crystal silicon. The beam then passes through 1 m of uncoated, evacuated guide tube. Evacuation also prevents losses from neutron scattering in air. The next 2 m of guide are defined at each end with Li-glass collimators C1 and C2. Collimator C1 is 2.5 cm in diameter defines the entrance to the guide tube, while collimator C2 is 1.5 cm in diameter and defines the exit of the guide. At 40 cm, 80 cm, 120 cm, 150 cm, and 175 cm, LiF scrapers S1, S2, S3, S4, and S5 clean the beam of divergent and scattered neutrons. The scrapers S1, S2, S3, S4, and S5 have diameters 5.898 cm, 5.700 cm, 5.507 cm, 5.344 cm, and 5.319 cm respectively. Finally, 57 cm of uncoated guide have a Li-glass collimator C3 of diameter 2.3 cm at the end to define the beam entering the experiment. All of the collimators are backed with lead, and the vacuum components are coated with LiF to absorb stray neutrons and gammas. Boroflex is added around the outer edges of

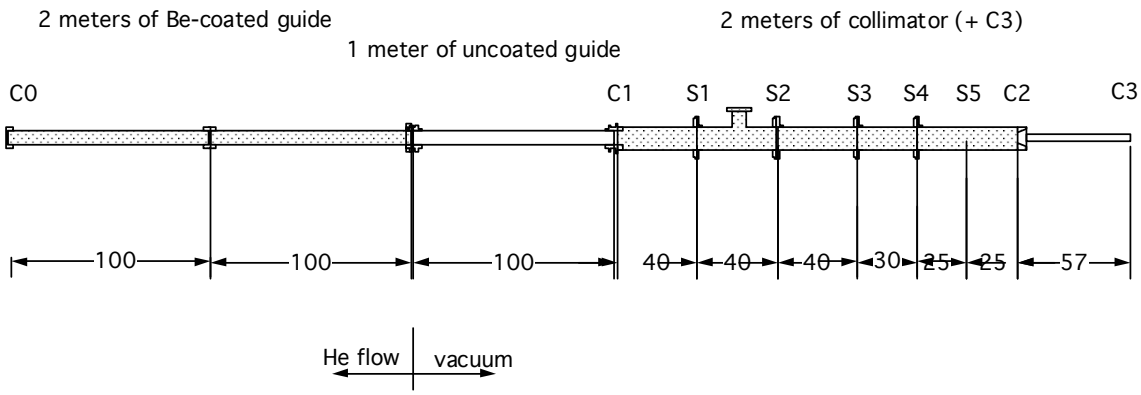

Figure 3.2: A schematic illustration of the guide tubes and collimation system that delivers the cold neutron beam to the radiative beta decay experiment. All collimators and scrapers are backed with lead to absorb stray neutrons and gamma rays.

the experiment to further absorb stray neutrons. Boroflex is a neutron absorbing silicon rubber with boron carbide homogeneously mixed in the matrix. Figure 3.2 shows the collimation and guide tube system.

Images of the beam were made with a dysprosium foil placed downstream from collimator C3 at the exit of the magnet bore. The neutrons are captured on ^{164}Dy and subsequently beta decay. The activated transfer foil then exposes a photographic plate that is sensitive to the beta decay electrons from the dysprosium. The exposed photographic plate is then read by a sensitive image reader which has pixel resolution of 0.2 mm by 0.2 mm. A false color image of the beam is shown in figure 3.3.

3.3 Proton and electron detection

This section describes the charged particle detection (electrons and protons) in the high magnetic field. An important feature of this apparatus is the ability to change the effective decay phase space that is detectable with an electrostatic mirror. The combination of the electrostatic mirror and the magnetic field have a complicated interplay on the precise tracking of the charged particles. This is the primary moti-

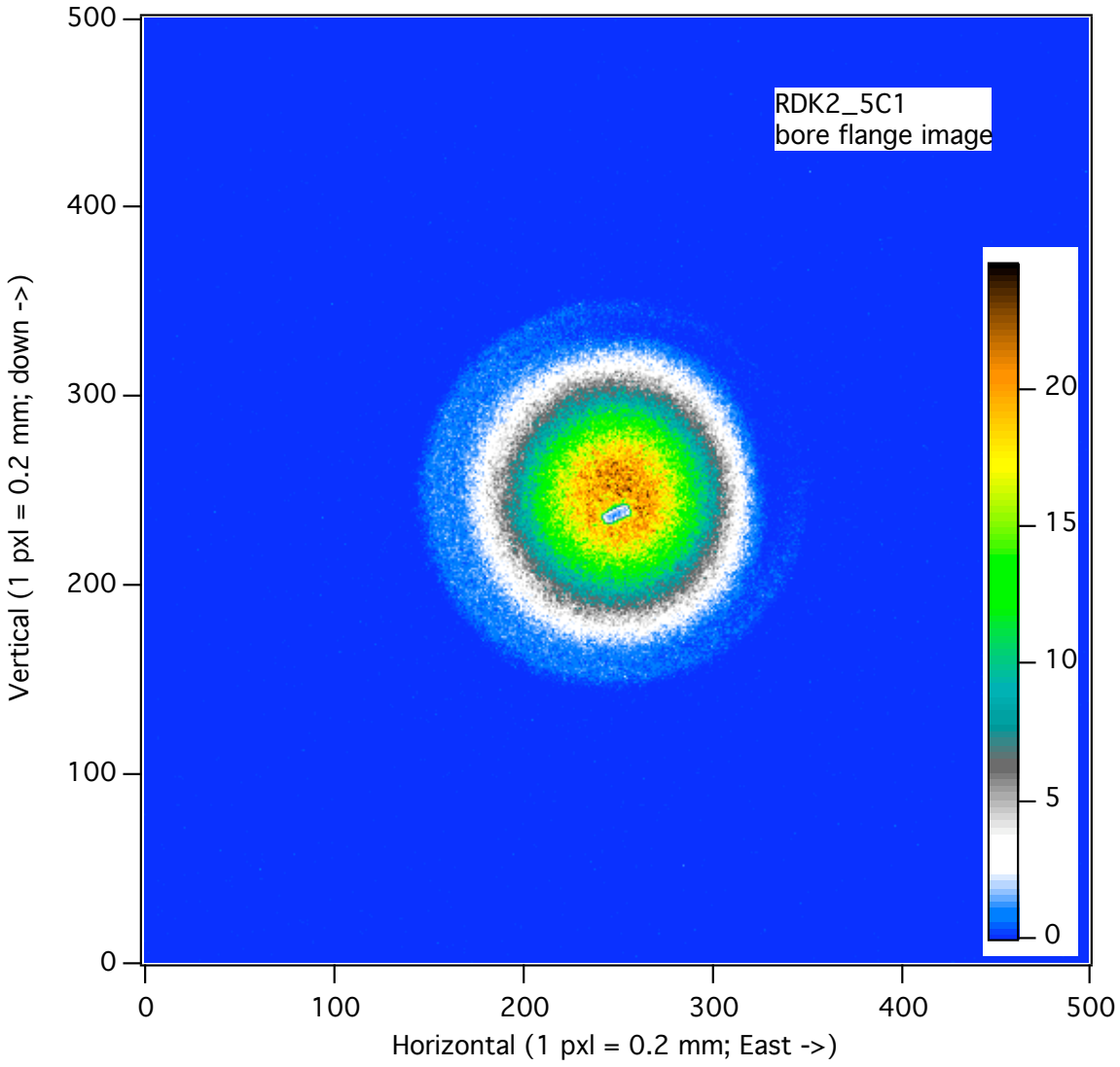

Figure 3.3: Photographic transfer of a neutron activated dysprosium foil. The feature in the center is a cadmium marker for orientation purposes.

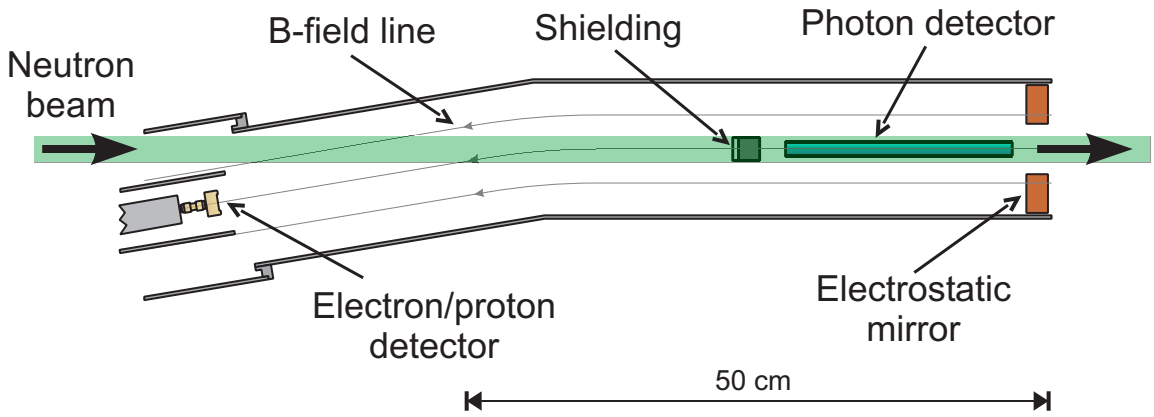

Figure 3.4: A top view illustration of the detection scheme for measuring the radiative decay of the neutron. The shielding and detector lie below the neutron beam.

vation for the Monte Carlo (MC) simulation discussed in chapter V.

The cold neutron beam enters the apparatus parallel to a 4.6 T magnetic field from a superconducting solenoid. This apparatus has previously been applied in experiments to measure the neutron lifetime [27, 69] and the electron-antineutrino angular correlation coefficient (a) in neutron decay [62]. The solenoid has a 9.5° bend in the upstream direction where the charged particle detector is situated. Therefore, the detector lies out of the beam path and is spatially removed from the main decay region. Figure 3.4 shows a schematic drawing of the experimental apparatus.

When a neutron decays in the main decay region, the emitted charged particles are confined to tight, cyclotron orbits around the magnetic field line. Given the average mass and energy of the electron and proton, these particles are confined to orbits less than 1 mm in diameter. The initial, longitudinal component of momentum determines whether the particle is guided upstream or downstream while the transverse components are confined to cyclotron orbits. Particles with longitudinal momentum oriented downstream tend to be guided out of the apparatus and are undetected. Particles with longitudinal momentum oriented upstream tend to be guided into the 9.5° bend towards the charged particle detector. At the entrance

and exit of the magnet, the solenoid magnetic field falls off in magnitude, and the magnetic field lines necessarily diverge. Decays occurring where the magnetic field drops off are lost because of the magnetic mirror effect, and this is elaborated upon in chapter V.

The charged particle detector is a silicon, surface-barrier detector (SBD) from ORTEC. The SBD is 600 mm^2 in area and 1 mm thick with a 40 μg / cm^2 gold layer serving as the positive contact on the front ($\approx$ 20 nm thick) [70]. A SBD is a semiconductor in the p-i-n configuration, and it is operated with reverse bias to develop a large depletion zone which serves as the active detection region [70, 71, 72].

The maximum proton kinetic energy is 751 eV, and they do not possess enough energy to pass through the SBD dead layer and deposit energy in the SBD. The SBD is held at -25 kV to accelerate these low energy protons through the SBD dead layer. The dead layer causes the 25 keV protons to lose approximately 5 keV of energy before the protons deposit energy. The higher energy electrons do not experience appreciable loss in the dead layer, and the energy spectra from the SBD are calibrated by using features from only the electron spectra. This calibration procedure is discussed in chapter VI.

The SBD and its onboard preamplifier extend into the superconducting magnet assembly and are cooled to low temperature ($\approx$ 150 K). This improves the noise characteristics and allows the accelerated protons to be resolved. The SBD is biased at -25 kV to accelerate the protons into the detector. An electrically isolated cage houses the SBD electronics and power supply (at -25 kV) while the apparatus is grounded. The SBD is powered by onboard batteries since the use of an isolation transformer introduced noise into the SBD signals. The gain of the SBD changed slightly during the life of the batteries, but the change was slow and accounted for

during the calibration (see chapter VI). The onboard preamplifier is a design similar to that used in the emiT experiment, and its construction is documented in detail elsewhere [66, 65]. A fiber optic driver couples the preamplifier signal to the grounded electronics rack, and the remaining electronics are described in section 3.5.

The electrons have low mass and possess a few hundred keV of energy. Their transit time from decay to detector is approximately a few nanoseconds. The protons have much lower energy are delayed from the electron by a few microseconds. The timing resolution on the SBD is sufficient to resolve the proton signal from the electron signal. The detection of a high energy electron signal followed by a delayed proton represents the trigger to the data acquisition system (DAQ). Section 3.5 discusses the triggering and DAQ in more detail.

In neutron decay, the electron and proton are preferentially emitted in opposite directions. Without apparatus modification, only events where the proton and electron are emitted in the same upstream hemisphere are detected. The proton energy is less than 1 keV so 1 kV electrostatic fields are sufficient to reflect protons emitted downstream back towards the SBD. An annular, electrostatic mirror which permits the free passage of the neutron beam through its center was placed downstream to reflect these "wrong-way" protons. The voltage applied to the electrostatic mirror is a free parameter, and by adjusting the voltage, the detectable phase space for decays is changed. The background rate versus mirror voltage behaves differently from the radiative decay event rate, and the mirror represents a way to distinguish these rates.

The computation of the exact solid angle for charged particle detection is complicated by the non-uniformity of the magnetic fields coupled with the complicated electrostatic mirror potential. The effective decay region has a smaller area than the 600 mm^2 subtended by the SBD because the magnetic field drops off at the

SBD. Within the effective decay region, the apparatus accepts approximately 2π solid angle for electrons and up to 4π solid angle for protons at full mirror potential. MC is necessary to yield a precision calculation of the solid angle as a function of electrostatic mirror voltage.

3.4 Photon detection

The detection of the radiative beta decay photons requires a detector that has a large active area for detection and sufficient timing resolution to correlate the photon with the electron-delayed proton trigger. It must operate in an extreme environment which is the cryogenic, high-magnetic field region of the superconducting magnet bore. In this section, the motivating factors are discussed for the choice of detector. A description of the main components is made in sections 3.4.1 and 3.4.2. Section 3.4.3 describes the photon detector assembly that was used in the experimental run.

The detector was a large-area scintillator crystal coupled to a photodetector to collect the scintillation light. The high magnetic field prevents using a photomultiplier tube (PMT) to collect the scintillation light inside of the magnet bore because the strong magnetic fields affect the trajectories of the secondary electrons between the PMT dynodes. Fields as low as 0.1 mT adversely affect a PMT's performance.

The scintillator was a pure, inorganic crystal of bismuth germanate ($Be_4Ge_3O_{12}$) coupled to a silicon avalanche photodiode (APD). This scheme of using a solid state photodetector inside of the superconducting magnet bore was chosen in lieu of the traditional method of piping the light outside of the apparatus with a light guide (e.g. acrylic) to a photomultiplier tube (PMT). Additionally, the bismuth germanate (BGO) scintillation light is centered at 480 nm where the PMT has a 20 % quantum efficiency compared to 50% for an APD [4, 73]. The operation of this photon

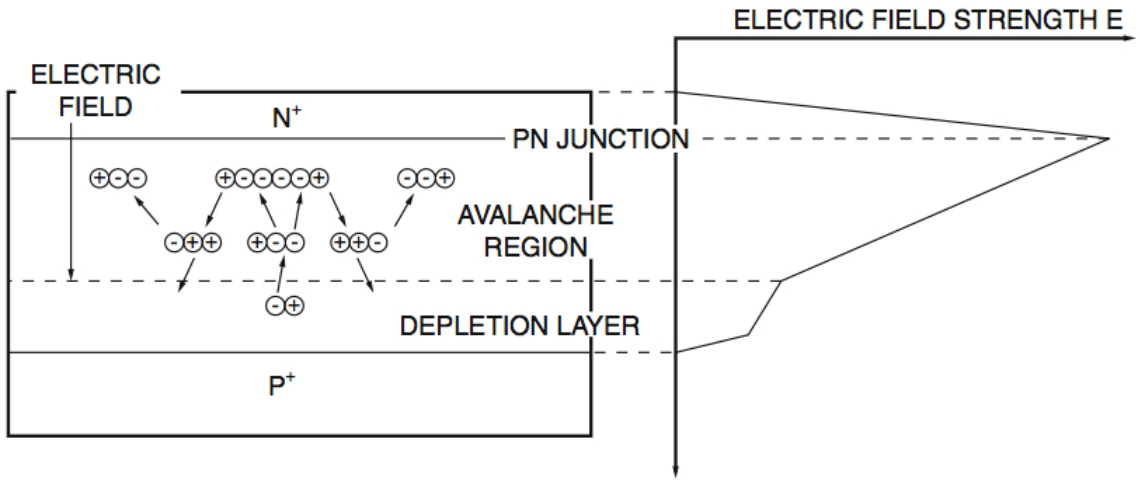

Figure 3.5: Semiconductor layout for a typical APD with the internal electric field felt by the resulting carriers [3].

detection scheme is described below, and it has also been described elsewhere [74, 75].

3.4.1 Avalanche photodiodes

An APD is a very thin, heavily-doped semiconductor photodiode in the p-n configuration (the heavily doped regions are labeled p^+ and n^+). By applying reverse bias to the photodiode, the depletion zone can be made large enough to absorb the energy of incident photons. The thinness, heavy doping, and large reversed bias generate a large internal electric field near p-n junction [76]. A schematic of the APD and the internal electric field are shown in figure 3.5 [3]. The operation, noise characteristics, and experimental performance of the APD are described below. There exist a wealth of papers on applications and characterization of APDs, the following references are just a few [3, 4, 73, 77, 78, 79, 80, 81, 82].

When a photon enters the APD, it deposits its energy in the depletion zone and creates electron-hole pairs. These carriers are accelerated by the large electric field inside of the APD. At higher reverse bias, the carriers collide with the crystal lattice, and these collisions liberate secondary carriers. This process creates an avalanche of

carriers which amplifies, with high gain, the original signal at high enough reverse bias. The electron amplification process in an APD occurs over a distance on the order of 10 μm versus the larger distance secondary electrons travel between dynodes in a PMT, and the APD is unaffected by large magnetic fields [78].

At room temperature, APDs have a markedly worse signal-to-noise ratio (S/N) than do PMTs. The total noise σ_n has contributions from dark currents I_d, thermal noise, and shot noise. The dark current contributes a constant noise for current components that travel parallel $I_{d\|}$ to the semiconductor junction and are not multiplied. Dark current components that are perpendicular $I_{d\perp}$ to the junction are multiplied, contributing noise that proportional to G^2 where G is the gain. The thermal noise is the dominant source of noise at room temperature and is greatly reduced at cryogenic temperatures. The shot noise in an APD is worse than that from a non-multiplying, photodiode with the same bandgap, and this excess noise is given by F. The total noise per unit bandwidth B is

$$\frac{\sigma_n^2}{2eB} = (I_0 + I_{d\perp})G^2F + I_{d\|} + \frac{2k_BT}{eR} \tag{3.2}$$

where I_0 is the photocurrent for $G = 1$, k_B is Boltzmann's constant, T is the temperature, and R is the load resistance. The excess noise factor is a consequence of Poisson statistical fluctuations in the multiplication process. The excess noise factor $F = \mathcal{O}(1)$, and its value depends upon the gain G and relative ionization rate for electrons and holes [3, 73, 82]

The dark currents have a strong temperature dependence due to thermal vibrations in the crystal lattice. Interactions with lattice phonons are suppressed at cryogenic temperatures, and the multiplication process improves. APD S/N is improved by both an increase in gain and a dramatic decrease in noise as the temperature decreases [83, 84]. This improvement seems to saturate from 40 K to 77 K, and

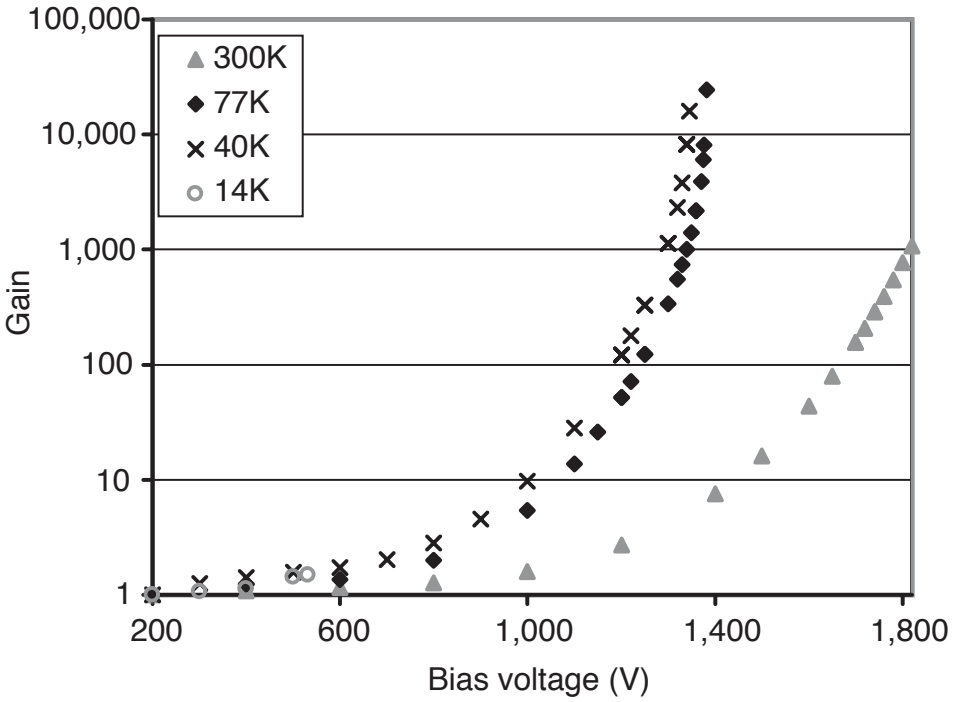

Figure 3.6: APD gain as a function of reverse bias for four temperatures. This image is reproduced from Yang et al. [4].

below 40 K, a dramatic loss of gain is attributed to carrier freeze-out [4]. Figure 3.6 has been reproduced from reference [4] and shows the APD gain versus operating voltage for four operating temperatures.

The APD used in the experiment was a Radiation Monitoring Devices model S1315 large area APD (13.5 mm $\times$ 13.5 mm active area) [77]. From room temperature to liquid nitrogen temperature 77 K, the breakdown voltage dropped from over 1800 V to approximately 1400 V. At room temperature the voltage where avalanche breakdown occurs is not well defined, but at 77 K, this transition is very dramatic and can be measured to $\pm$ 0.5 V. Near 77 K, the change in the breakdown voltage changes by 6 V for every 5 K change in temperature. Near 77 K and at 25 V below breakdown, the APD gain changes by 4.7 % for every 1 K temperature change. Near 77 K and at 25 V below breakdown the APD gain is approximately 10^3. The total

capacitance for this APD is approximately 120 pF.

3.4.2 Scintillators

BGO was the scintillator selected for the photon detector in the experiment. Below, the properties of the most common scintillators are compared to needs for the experiment. A general comparison is made to aid in scintillator selection for experiments that are similar to this radiative decay experiment. The specific properties of BGO that make it the scintillator choice for the experiment are reviewed. There is a wealth of scintillator data in the literature, and much of the remaining discussion derives from these basic references (including vendors) [71, 72, 85, 86, 87, 88, 89, 90].

The ideal scintillating crystal for this experiment must have a high light yield and short decay time constant at 77 K. It is preferable to use dense materials to absorb as much radiation as possible, especially at higher energies. A high-Z material improves the efficiency for photoproduction by the photoelectric effect and suppresses Compton scattering conversion of the incident energy. A scintillator may produce copious amounts of scintillation very fast, but the wavelength of this light must couple to a photodetector, e.g. PMT or APD. The effective light yield is the result of the convolution of the scintillator wavelength spectrum with the quantum efficiency of the photodetector as a function of wavelength.

To detect a large number of photons, large area scintillators are required (and at a reasonable cost). A large index of refraction n ensures that the scintillator can act as a light guide in order to transport the scintillation light to a photodetector [91]. Other important properties include mechanical ruggedness, low concentration of radioactive impurities during scintillator production, and being non-hygroscopic. The selection is further complicated by the cryogenic temperature requirement. There is extensive data for most scintillators at room temperature, but there can be a dearth of data

	NaI(Tl)	CsI(Tl)	CsI(na)	CsI(pure)	BGO	CaF_2(Eu)
Light Yield (photons / keV) 300 K	38	54	41	2	8-10	19
Light Yield at 77 K relative to 300 K	$< 1^*$	$< 1^*$	$< 1^*$	10	3	n/a
Emission wavelength (nm)	415	550	420	315	480	435
Primary Decay Time (ns) 300 K	250	1000	630	16	300	940
Density (g/cm^3)	3.67	4.51	4.51	4.51	7.13	3.18
Index of Refraction	1.85	1.79	1.84	1.95	2.15	1.47
Hygroscopic	yes	slightly	yes	slightly	no	no

Table 3.1: Properties of the most common inorganic, crystal scintillators. This list is not expected to be comprehensive. *-The doped scintillators are known to have a dramatic reduction in light yield. The light yield for CaF_2(Eu) at 77 K was not immediately found in the literature.

at 77 K.

Inorganic, crystal scintillators are known to be excellent photon scintillators, especially the alkali halides (NaI, CsI, etc). Many of these scintillators are doped with carrier trapping centers that produce the scintillation. Doped scintillators generally have high light yield at room temperature, but the light yield tends to saturate and fall off as the temperature falls. On the other hand, pure alkali halides and BGO tend to have a large increase in light yield as the temperature drops. The scintillation time slows for most inorganic crystals. The spectral response and scintillation timing for many crystals have a fast (1 ns -10 ns at room temperature) component and a slow, afterglow component (a few μs). The important properties for the most common scintillating crystals is reported in table 3.1.

BGO and pure CsI are very good candidates for numerous reasons. Both have large light yields at 77 K; CsI yields approximately 20 photons / keV [92, 93], and BGO yields approximately 28 photons / keV [94, 95, 96]. Unfortunately, both crystals' scintillation decay time slows; CsI is approximately 1 ns, and BGO is approx-

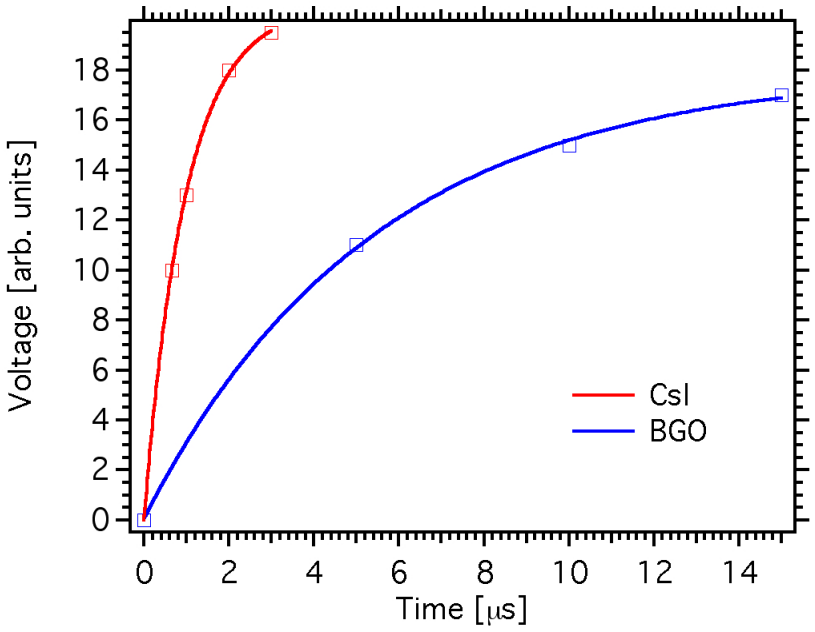

Figure 3.7: Measured rise times for BGO and pure CsI at 77 K.

imately 6 ns. The scintillation process in BGO results in a hole in the 6s level of Bi^{3+} and an excited electron in the 6p level. The luminescence from these levels is spin forbidden and responsible for the slowed light emission from the scintillator. At room temperature, competing non-radiative modes account for the reduced light output but faster decay time [85, 95]. A similar mechanism is responsible for the CsI slowdown [93]. The rise times in the collected signal are shown in figure 3.7. BGO has a larger atomic number ($Z = 83$ for bismuth) than CsI and a higher efficiency for photoelectric effect energy conversion (less Compton) . Finally, the slight hygroscopic nature of pure CsI has been linked to a spatial dependence in detector response. Additional data for CsI is contained in the references of [97], and there are tests with wavelength shifters on CsI [98].

The scintillation response for radiative decay photons ($\omega < 782$ keV) are primarily photopeak. Figure 3.8 shows total photon absorption cross section for BGO, and it is broken up into the contributing modes of absorption. The data are collected from

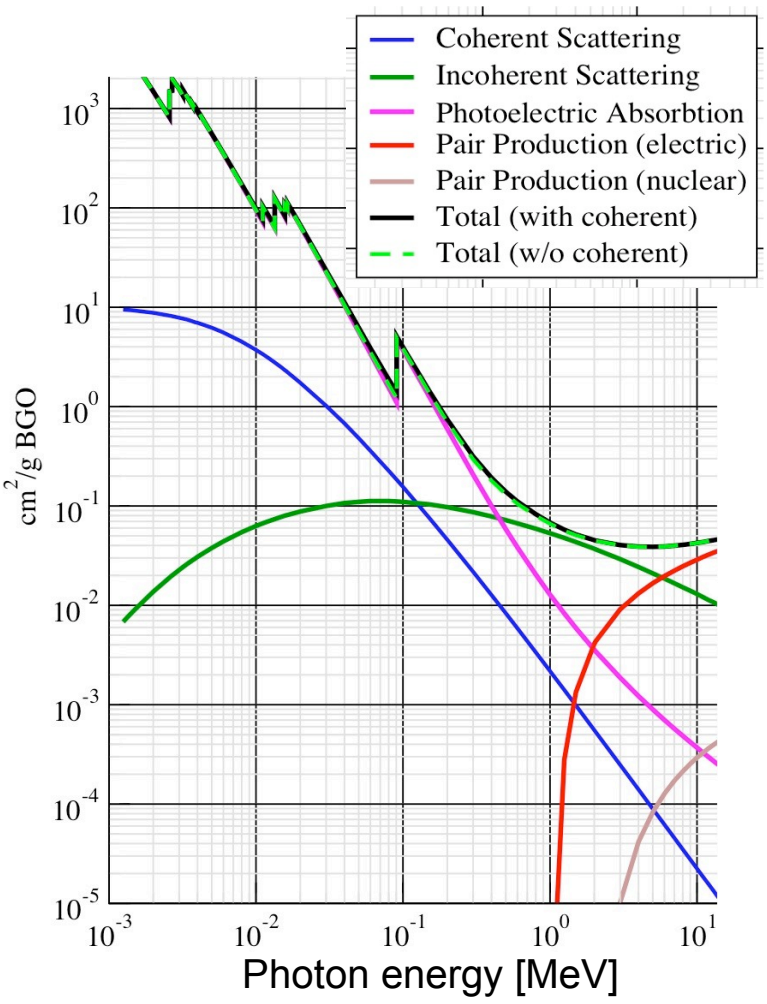

Figure 3.8: Total photon absorption cross section for BGO. The various mechanisms for photon interaction are plotted separately; the photoelectric effect dominating for the energy range of interest in the experiment. The plot is generated from the NIST Physics Laboratory XCOM photon cross sections database [5].

the NIST Physics Laboratory XCOM photon cross sections database [5].

3.4.3 Detector assembly

In the experiment, a 1.2 cm × 1.2 cm × 20 cm long BGO crystal [90, 99] was wrapped with a single layer of teflon tape and then wrapped with in a thin, reflecting layer of aluminum. The teflon and aluminum provide a protective, reflecting layer that does not significantly alter the incoming photon spectrum. One end (1.2 cm × 1.2 cm face) of the crystal was left open, and the other end was covered in teflon

and aluminum as a rear reflector. The covering does not wet the surface, and the crystal's high index of refraction interfaces with the vacuum. Approximately 10 % of the total scintillation light produced is collected by the APD. Considering the excess noise factor and quantum efficiency of the APD, the measured energy resolution is consistent with prediction [91].

The crystal was mounted in an aluminum holder and precisely located below the neutron beam in the downstream end of the decay region. The face of the crystal (1.2 cm $\times$ 20 cm) directed towards the neutron beam was placed 3.82 cm from the center of the bore. The APD was placed in direct contact with the open end of the BGO at the downstream end. The APD was operated with a reverse bias of 1378 V during the experiment's operation. This voltage is approximately 20 V below breakdown which was found to maximize S/N of the APD. The breakdown voltage can be measured to within $\pm$0.5 V, but the breakdown voltage slowly drifted by a few volts over the course of the experimental operation.

The signals from the APD were transmitted outside of the apparatus with stainless steel wires to a Canberra proportional counter preamplifier - model 2006. Stainless steel was used to reduce the heat load from outside (300 K) onto the APD because the breakdown voltage is strongly temperature dependent. The voltage output from the preamplifier is proportional to the charge collected. A pulse of charge on the preamplifier decays with an RC time constant of 50 μs. The gain on the preamplifier was set to the highest setting, 235 mV / million-ion-pairs [100]. The preamplifiers were placed outside of the superconducting magnet at room temperature as close to the apparatus as possible to reduce the noise. The output signals were sent to a spectroscopy amplifier and a multi-channel analyzer during off-line cryostat tests. During the experimental, better timing resolution was possible with sharp, leading

edge of the preamplifier signal.

Extensive testing of the detector was performed in a cryostat setup with the use of external sources. A ^{241}Am source (60 keV gamma rays) and ^{137}Cs source (662 keV gamma rays) were used to test the detector response. Using a lead collimator, source gamma rays are applied to specific areas of the scintillating crystal detector. The S/N was optimized in the cryostat while the timing and pulse shape of photon events were recorded and analyzed. These pulse shape studies factored in the analysis of the runtime data. One of the most important tests was that of spatial dependence.

Spatial dependence of the crystal was checked in 3 positions, the center and approximately 5 cm from each end. In BGO, there was no appreciable spatial dependence at the level of sensitivity in the experiment. A more detailed study where the sources were translated by 1 cm confirmed very little spatial dependence in the bulk of the crystal. CsI, on the other hand, showed a strong spatial dependence that was affected by polishing the crystal. A wavelength shifting paint was added to CsI and a spatial dependence was introduced where none existed previously. Removal of the paint did not remove the spatial dependence though. The unresolved nature of CsI spatial dependence was one of the main reasons it was rejected for the experiment. The cryostat testing is described in more detail elsewhere [101].

The photon energy detection threshold was measured to be 15 keV by calibration with an ^{241}Am gamma ray source. The calibration was also monitored during the run with spectrum features which is described in chapter VI. The 60 keV photon peak had 22 keV full-width-at-half-maximum (FWHM), and this width is dominated by the statistics of the electron-hole pair generation and multiplication in the APD [79]. Over the course of several months of experimental running, the gain of the photon detector was found to be stable to within 10 % of the average gain. The detector

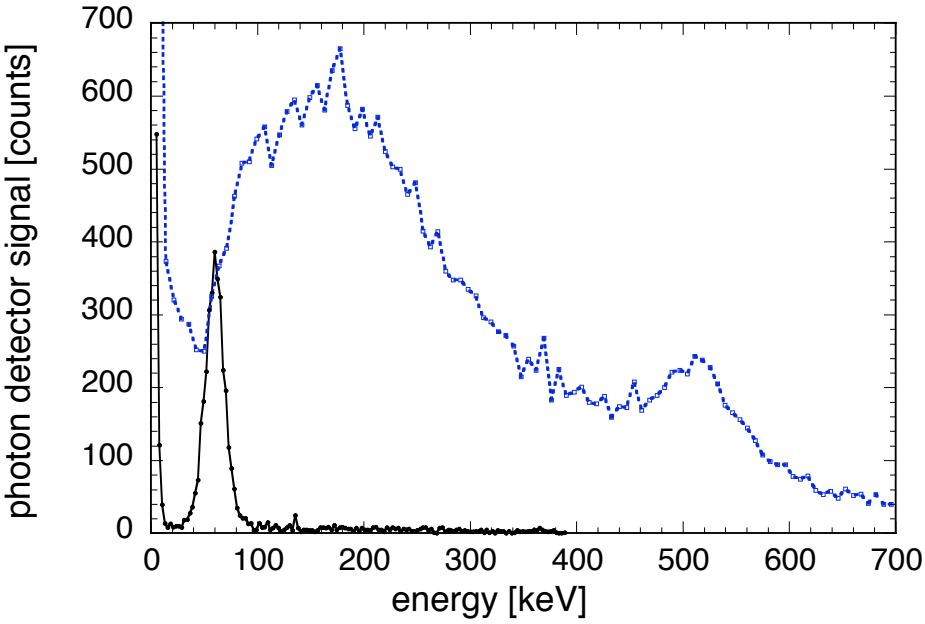

Figure 3.9: Detector response to ^{241}Am source (black) and the raw photon spectrum. The broad peaks used for gain monitors are at 160 keV and 511 keV (blue).

response to the ^{241}Am source and beam features is shown in figure 3.9.

3.5 Data Acquisition System

In hardware, the data acquisition system searches for an electron signal, followed by a delayed proton signal to act as a trigger to the data acquisition system (DAQ). The signal from the SBD and its onboard preamplifier was coupled via a fiber optic cable to low voltage electronics where it was split, and each line was amplified by a spectroscopy amplifier. A fiber optic line was necessary to bring signals from the SBD biased at -25 kV to low voltage. Each line was analyzed with a single-channel-analyzer (SCA) to search for an electron and proton signal.

The SCA window to search for an electron start pulse was set to approximately 35 keV to approximately 800 keV, the electron endpoint kinetic energy. The SCA window to look for the proton was set to encompass the entire 25 keV proton peak. The lower threshold on the electron SCA was set so that no proton signal could

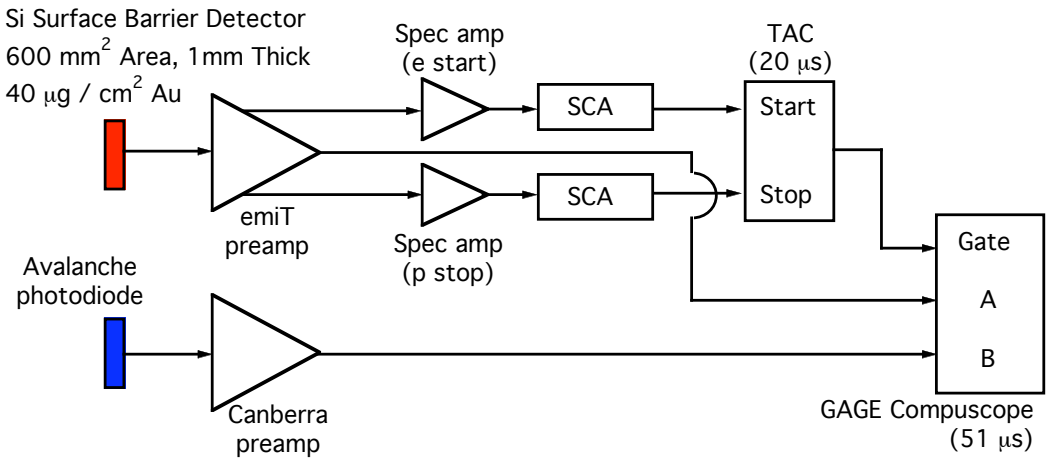

Figure 3.10: Schematic of the data acquisition system used in the experiment. The SBD signal was split and amplified. Start and stop pulses corresponding to an electron and delayed proton are sent to a TAC which triggers the oscilloscope card to record both the SBD signal and the photon detector preamplifier signal.

accidentally trigger the electron SCA. Any SBD gain shift causes the SCA windows to shift slightly, and it is most pronounced on the 35 keV electron energy threshold. chapter VI describes the systematic uncertainty due to this small shift.

The fast timing output from electron SCA window provides a start pulse to a time-to-amplitude converter (TAC), and the fast timing output from the proton SCA window provides the stop pulse to the TAC. If the delayed proton SCA stop pulse occurred within 20 μs of the electron SCA start pulse, the TAC sent out a conversion signal that triggered a computer-based digital oscilloscope card to record the amplified SBD signal and the preamplifier output of the APD. A schematic of the data acquisition system is shown in figure 3.10

A GaGe 82G oscilloscope card in the PCI slot of a computer recorded both the SBD amplifier signal and the APD preamplifier signal. The oscilloscope card is capable of recording two channels of bipolar data with 8 bits of resolution at a sampling rate of up to 1 GHz. The card can also store long strings of samples in memory, and it can buffer to memory and record pre-trigger data.

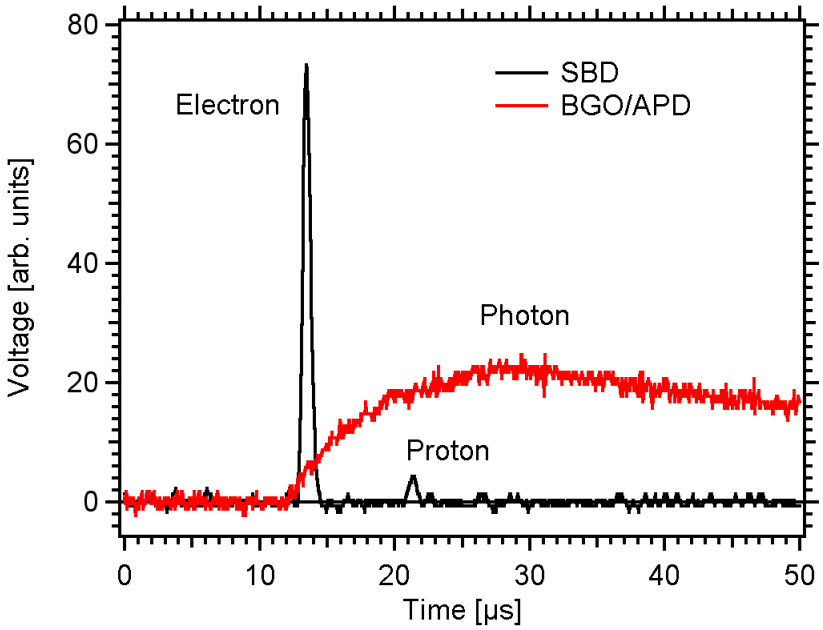

Figure 3.11: Sample waveforms collected from a valid electron-delayed proton trigger. The surface barrier detector has Gaussian peaks for the electron and the proton (red). The preamplifier pulse from the APD shows a slow rising photon signal (blue).

During experimental operation, the oscilloscope card recorded 1024 samples for both the APD and SBD channels simultaneously at a sampling rate of 20 MHz (50 ns / sample). To examine the uncorrelated photon background, approximately 14 μs of the waveform data are pre-trigger data. Figure 3.11 shows a candidate radiative beta decay event consisting of a prompt electron and photon followed by a delayed proton. The electron-delayed proton trigger is independent of the photon detector, and an analysis in software determines the photon content.

3.6 Rate Estimates

Before concluding the chapter, it is useful to make an estimate of the measured decay rates to understand the experiment. This discussion is useful as a guide towards future upgrades to the experiment. The total decay rate of neutrons Γ_0 in the decay

region is approximately

$$\Gamma_0 \approx \Phi_n A_d \frac{\ell_d}{v_n \tau_n}. \tag{3.3}$$

The neutron beam flux Φ_n delivered to the experimental apparatus on the NG-6 beam line is approximately 5×10^7 s^{-1}·cm^{-2}. The average velocity v_n of the neutrons in the beam is 10^5 cm·s^{-1}. The effective area for detection A_d is approximately 3 cm^2 despite the beam area being larger. The decay region length ℓ_d is approximately 40 cm. The neutron lifetime τ_n is approximately 885 s. With these parameters, the total neutron decay rate in the detection region is approximately 70 s^{-1}.

Half of these decays can't be detected because half of the electrons are emitted away from the SBD, and with the electrostatic mirror at full potential (all of the protons), the electron-delayed proton detection rate is approximately 35 s^{-1}. The solid area for photon detection is approximately 1 %, and the production of photons is suppressed by approximately 3×10^{-3}. This yields an electron-delayed proton-photon detection rate of up to 10^{-3} s^{-1}.

During the experiment, the singles rate for photon detection was approximately 100 s^{-1}. Assuming a 20 s^{-1} electron-delayed proton detection rate, and that the window for detection of a photon is open for 50 μs at every electron-delayed proton trigger, the total photon detection rate is 0.1 s^{-1} (uncorrelated and correlated). All of the rates estimated are consistent with the measured rates as shown in table 4.2.

CHAPTER IV

Analysis

Data was collected on a series by series basis where a series is defined as a set of consecutive runs consisting of 10^5 electron-delayed proton trigger events with the same runtime parameters (e.g. mirror voltage). A series had between 15 and 65 such runs, and the voltage was changed between each series. All of these events were stored and analyzed offline in software.

The software analysis is an iterative procedure that extracts the timing and energy of the electron, proton, and photon. Cuts in the timing and energy are made to select photons that are correlated with the electrons. Because the neutron flux was not measured, a ratio of the radiative decay rate to non-radiative decay rate is used to extract the branching ratio. The analysis utilizes the fact that the electrostatic mirror voltage is varied throughout the experiment.

For every electron-delayed proton hardware trigger, the SBD waveform data and the APD waveform data are recorded. Figure 3.11 shows sample data from the SBD and APD channels due to a hardware trigger. The SBD data are two Gaussian peaks which occur at approximately 15 μs from the start of the waveform because pre-trigger data were recorded. If a photon exists in the APD waveform data, it has a slow rise time due to the cold BGO and a long tail due to the preamplifier. Because

the photon waveform does not factor into the trigger logic, an existing photon signal may not be correlated to the electron-delayed proton trigger. All recorded data is the result of an electron-delayed proton hardware trigger, and no single particle data were recorded.

4.1 Data Reduction

The first step of the analysis is to extract the timing and energy of each particle, i.e. to reduce the waveform data to a few parameters. Because of "pathological" background events, a crude shape analysis is performed. Before analyzing the waveform data, the raw data must be must be corrected in software for a small baseline bias that can occur. Because the SBD has Gaussian peaks at 15 μs, an average of the first 5 μs of the pre-trigger data is averaged to correct for the baseline bias. Because the photon pulse shape is so wide and its location unknown, correcting the photon baseline is more complicated. An average of the first and last 5 μs of the waveform are made. The photon signal's baseline is corrected by the minimum of these averages.

4.1.1 First iteration

At the first iteration, the energy and onset time of the electron and proton are extracted. The photon is neglected at this level of analysis. Since there are over 10^7 total electron-delayed proton triggers, this iteration must be computationally quick.

To analyze the electron, the peak height and peak location were found by analyzing a window around the prompt timing location in the SBD waveform. The electron energy is estimated by integrating over a $\pm 1.2\,\mu$s window around the peak location. This analysis window was optimized by considering many sample pulses for varying window sizes. The accelerated proton is also identified by a peak in the waveform

occurring after the electron pulse. Similarly, the energy of the proton is found by integrating over a $\pm 0.75\,\mu$s window around the proton peak.

The electron and proton onset times are estimated from the peak location, and the timing difference is calculated. Because the Gaussian peaks have a non-trivial width, the peak does not accurately reflect the actual incidence time for the particles. The origin of this effect can be understood by considering two electron pulses with the same onset time, but different energy. The peaks will appear to be shifted, despite having the same onset time. A slewing correction is made which was optimized by analysis of many electron pulses. The slewing correction is required for an accurate comparison to the MC.

4.1.2 False triggers

It can happen that a high energy background particle can strike the SBD and leave a distorted pulse with a long tail. A sample of this "pathological" event is shown in figure 4.1. Typically, such events were due to beam-related gamma rays and comprised up to 10 % of the electron-delayed proton trigger rate prior to the application of the cuts. The hardware trigger incorrectly identifies this event as an electron and a proton with a very small time difference. When the geometry and kinematics are considered, the majority of events have an electron-delayed proton time difference that is greater than 2.5 μs. Therefore, real electron-delayed proton events have an electron pulse which rises to its peak value and returns to the baseline before the proton pulse occurs.

At this stage of the analysis, the minimum bias that occurs between the electron and proton peaks is recorded. A cut can be made on this value, where events failing the cut are rejected as not being a real electron-delayed proton event. The value used in the final determination of the branching ratio is 0, meaning that the electron pulse

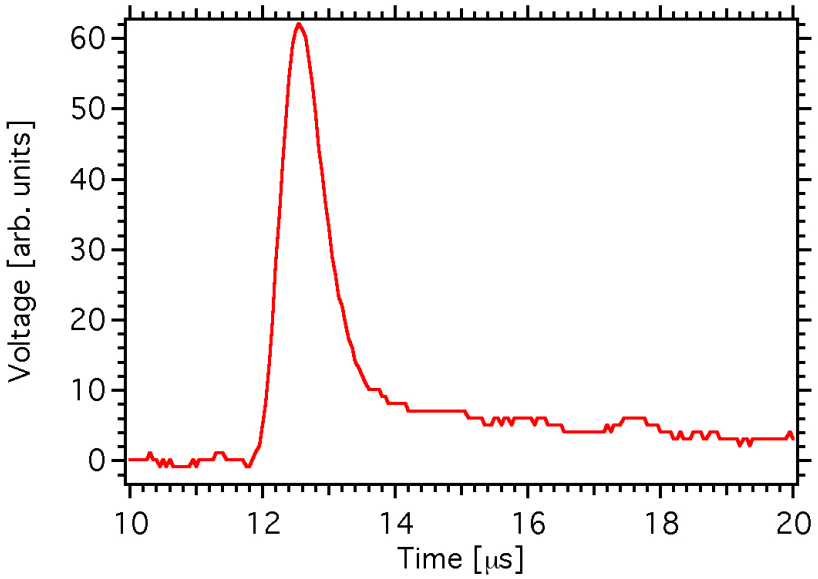

Figure 4.1: A "pathological" event that satisfies the hardware trigger conditions but is not a real electron-delayed proton event. These events are high energy background particles that deposit a large amount of charge which saturates the SBD. The SBD then takes a few microseconds to recover.

must return to the baseline value. This cut is also referred to as the the baseline cut.

4.1.3 Photon analysis and second iteration

The second iteration of analysis is performed only if a photon signal exists in the APD waveform. The presence of a photon is inferred from an overall increase in the bias of the photon waveform in time. If a photon arrives at any time in the recorded waveform, the bias of the pulse shape increases at later times because of the long RC time constant (50 μs) of the preamplifier. By averaging the first 1 μs, last 1 μs, and the entire pulse, the presence of the photon within the timing window is inferred from an overall increase in the total bias when compared to the beginning and end. This test serves a flag for further refinement of the timing and energy of the electron and photon.

The timing and energy of the photon are found with a template fit to the waveform. A template fit uses a least square procedure to fit the data to a model waveform

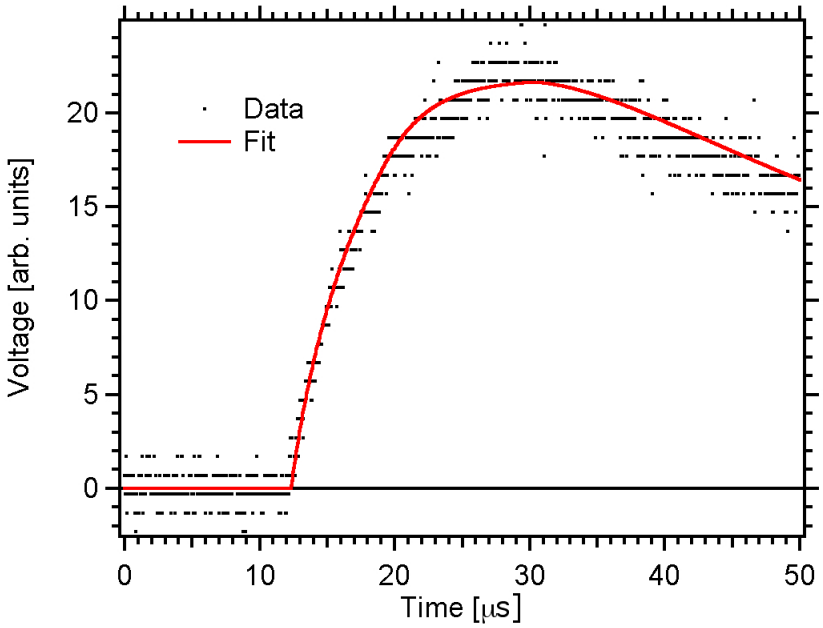

Figure 4.2: Sample photon pulse data with the template fit from analysis. The banded structure of the data is due to the 8-bit voltage resolution and selected voltage range for the oscilloscope card.

shape. This model is modified by translation, scaling, and time scaling (stretching in time, like an accordion), and it was optimized by studying photon signals collected during experimental operation and from cryostat test data. The translation fit parameter corresponds directly to the photon incidence time, and the amplitude fit parameter is proportional to the photon energy. A sample photon pulse and the template fit are shown in figure 4.2.

A 4-parameter, modified gaussian with a tail is fit to the electron peak if a photon is observed in order to refine its timing and energy measurements [102]. The functional form is

$$\frac{A}{2\tau}\exp\left(\frac{-(x-x_0)}{\tau}+\frac{\sigma^2}{2\tau^2}\right)\mathrm{erfc}\frac{-(x-x_0-\sigma^2/\tau)}{\sqrt{2}\sigma}, \tag{4.1}$$

where τ and σ are width parameters, A is an overall scaling, and x_0 is the onset time. The onset time fit parameter directly corresponds to to the electron incidence time, and no slewing correction is needed. The functional form can be integrated yielding

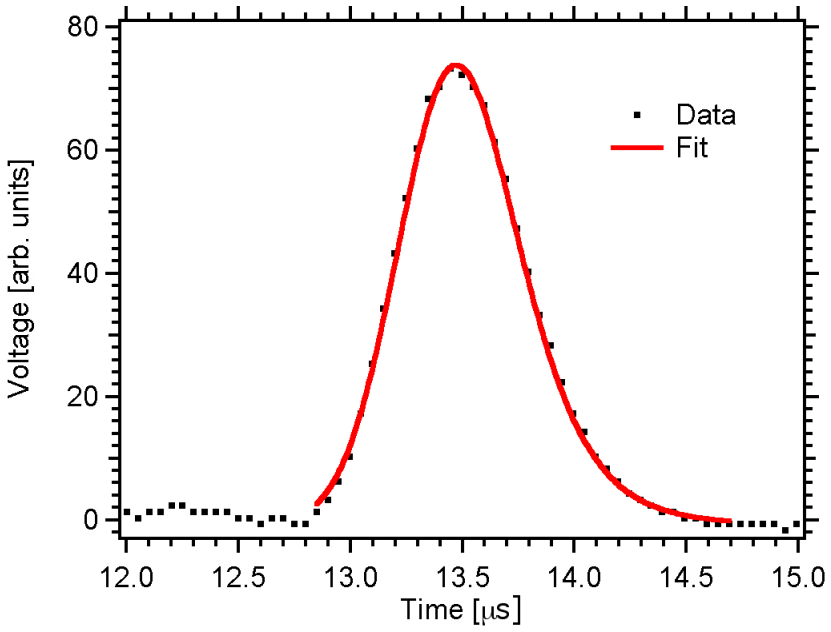

Figure 4.3: Sample electron waveform with fit function.

the area of the electron pulse which is proportional to the electron energy. A sample electron waveform with fit is shown in figure 4.3. Before applying analysis cuts to the reduced data set, it is useful to examine the raw timing and energy spectra.

4.1.4 Raw energy spectra

Figure 4.4 shows the raw, uncalibrated, proton area spectrum, and it is the histogram of the proton area calculated in the first iteration. The Gaussian peak is centered at 20 keV since the 25 keV protons lose approximately 5 keV in the SBD dead layer. This was found after calibration which is described in detail in chapter VI. The width of the Gaussian is dominated by SBD noise, but the decay spectrum and straggling also contribute.

Figure 4.5 shows the raw electron spectrum for all electron events above the hardware threshold of approximately 35 keV at 0 V applied to the electrostatic mirror. The features that occur at an electron area of 400 and 1100 (arbitrary units) are found to disappear when the baseline cut is used. The skew shape of the raw

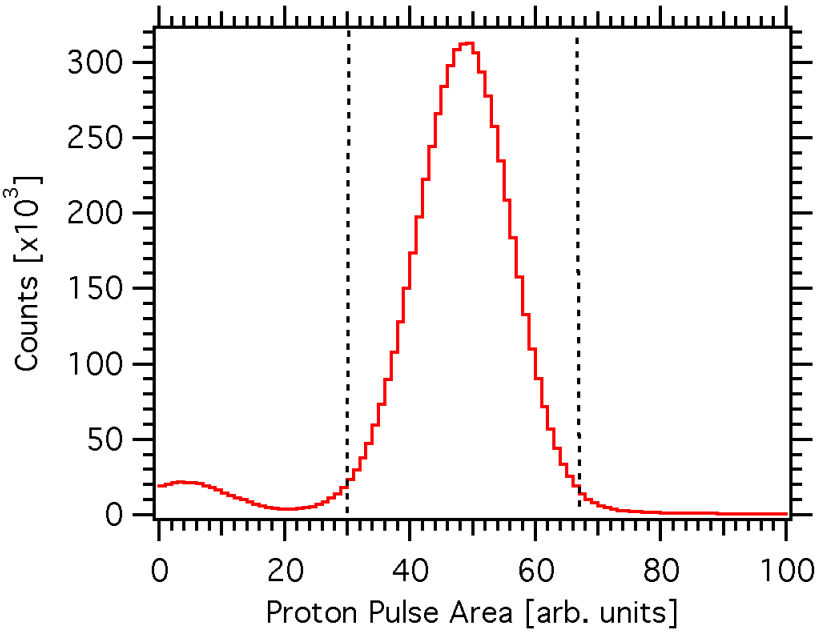

Figure 4.4: Histogram of the proton area from valid electron-delayed proton coincidence events. The pulse area is calculated by integrating the digital waveforms relates to the proton energy. The center of the peak is at approximately 20 keV, while the width is almost entirely from the SBD, not the proton energy distribution. The vertical lines are where 2 FWHM cuts are made.

spectra is primarily due to electron backscatter. The electrons strike the SBD at an angle which increases the backscatter probability which leads to an incomplete deposit of electron energy [103, 104]. This effect is partially ameliorated by the conversion of some of the transverse momentum to longitudinal momentum as the magnetic field diverges. The electrons are created in the decay region at a magnetic field of 4.5 T and are transported to the SBD which has a magnetic field of 2.6 T. The -25 kV bias field is a complicating factor that must also be accounted for when simulating the electron backscatter.

Figure 4.6 shows the raw photon spectrum derived from the electron-delayed proton triggers for all runs. This figure shows all of the photon events collected during the experiment's operation. The photon events are those that occur within a 20 μs window of the electron-delayed proton trigger (again, no photon singles data). The

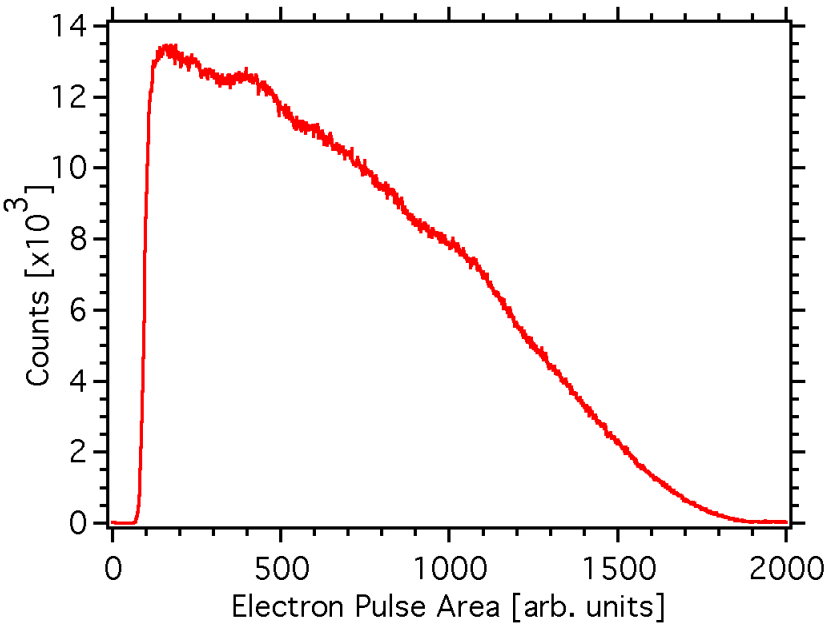

Figure 4.5: Histogram of the electron area from valid electron-delayed proton trigger events. This area is relatable to the electron energy deposited in the SBD. The skew shaped is due to electron backscatter. The features at channels 400 and 1100 are believed to be photon backgrounds.

raw spectrum has two features that aid in calibration and detector gain monitoring; a broad, backscatter peak at approximately 160 keV and a 511 keV pair production photon peak. The calibration procedure and its systematic effect on the branching ratio is described in detail in chapter VI.

4.2 Analysis Cuts

At this point in the analysis, the timing and energy have been extracted for all of the particles. The baseline cut removes the "pathological" trigger leaving real electron-delayed proton events. The baseline cut is different from the other analysis cuts because it rejects events that are not real electron-delayed proton events. The remaining cuts are used to select events where the photon is correlated in time with an electron-delayed proton events. The cuts can be split into energy and timing cuts, and further separated into those that only affect electron-delayed proton events and

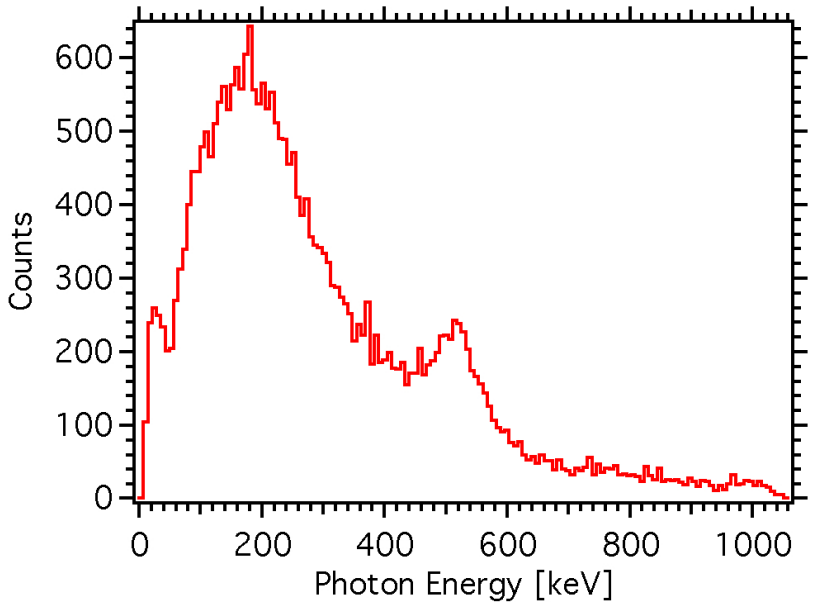

Figure 4.6: Histogram of the photon area which is relatable to the photon energy. The broad feature at 160 keV is the backscatter peak, and there is also the 511 keV pair production photon peak.

electron-delayed proton-photon events. The application of cuts introduces systematic uncertainties, and a detailed account of these is given in chapter VI.

4.2.1 Electron-delayed proton cuts

The energy spectra of each particle requires calibration. The electron energy spectrum is calibrated by the SBD response to a 60 keV gamma ray from ^{241}Am and from the electron energy endpoint in the raw spectrum (782 keV). The proton energy spectrum was not calibrated nor used as a calibration point for the SBD. The calibration procedure is explained in detail in chapter VI.

The raw proton area spectrum is a Gaussian peak whose width is dominated by the detector noise. A Gaussian fit was made to the raw proton area spectrum. Given the width generated from the fit, a 2 FWHM cut was made around the peak of the proton area spectrum, and these cut lines are shown in figure 4.4. No explicit cut on the electron energy was made, although the SCA window on the electron

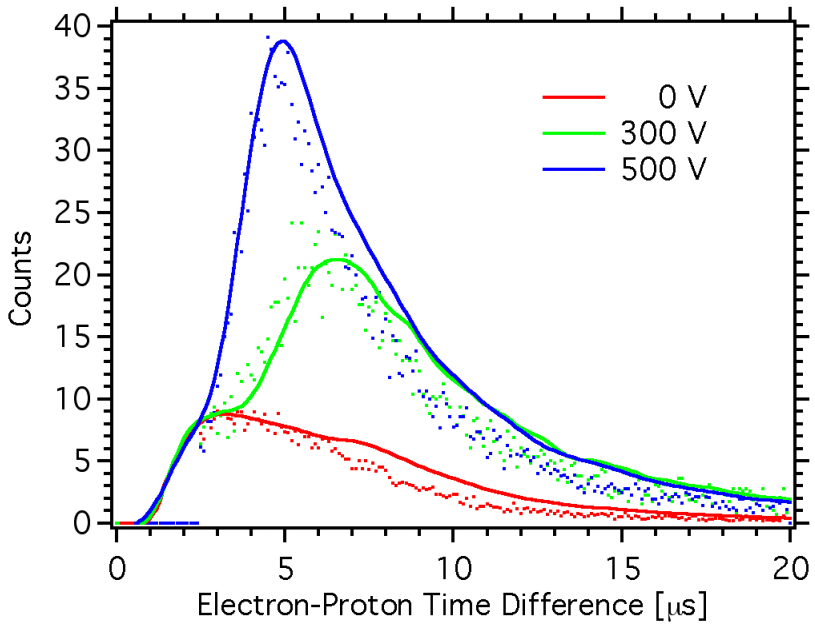

Figure 4.7: Histograms of the electron-delayed proton time delay data in the 2.5 μs to 20 μs timing window for electrostatic mirror voltages of 0 V, 300 V, and 500 V. The experimental timing spectrum is compared to MC simulation, and the agreement is good.

pulse corresponds to an approximately 35 keV threshold. For each series, the actual electron energy thresholds are reported in table 4.2.

A lower time cut of 2.5 μs is made on the electron-delayed proton time difference in software. The lower timing limit further suppresses the influence of the false triggers from "pathological" events. The TAC effectively puts a hardware cut of 20 μs on the data, beyond which, very few electron-delayed proton events occur. The electron-delayed proton time difference spectrum for various electrostatic mirror potentials is shown in figure 4.7. A MC simulation of electron-delayed proton time difference is also shown, and the agreement with the experimental data is good.

The electron energy spectrum after calibration and application of the cuts is shown in figure 4.8. The experimental data is the sum of all experimental data for the electrostatic mirror set to 0 V and over 700 V. The relative increase in the number of high energy electrons for mirror voltages above 700 V is due to the conservation of

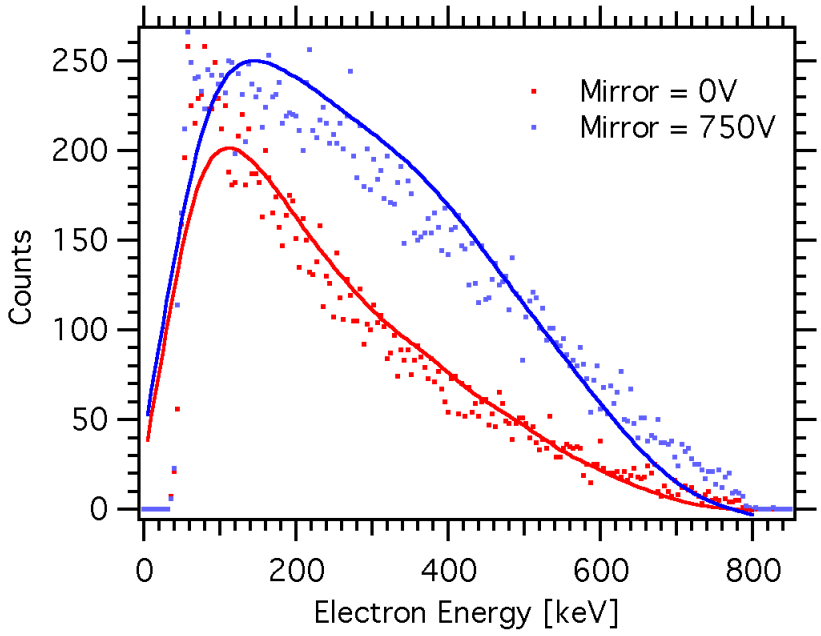

Figure 4.8: The calibrated electron energy spectrum after all the analysis cuts for mirror voltage held at 0 V (red) and over 750 V (blue).

momentum. High energy electrons must recoil off the proton which requires the proton to be emitted in the opposite hemisphere from the electron. Because the mirror voltage is above 700 V, these anti-correlated protons can be reflected and detected. This means that the high energy electrons are associated a delayed proton that is detected, and a valid trigger occurs. The detector response to the electron energy spectra is simulated in the MCNP5 Monte Carlo package [105]. The Monte Carlo simulation (MC) is discussed in connection to the electron backscattering systematic in chapter VI. Backscattering tends to skew the electron energy spectrum to lower energy. The MC simulation is compared to data at 0 V and 750 V electrostatic mirror potential in figure 4.8.

4.2.2 Photon cuts

A spectrum of the electron-photon time difference was created for photons that arrive within $\pm 10\,\mu$s window around the electron incidence time. A sample electron-

photon timing spectrum for a three-day period is shown in figure 4.9. Correlated photon events, which include correlated background photons and radiative decay photons, are centered at Δt = -1.25 μs. This time delay is due to electronic delays between the SBD and APD channels which is confirmed with pulser tests. The 1 μs width of the timing peak is due to the uncertainty in measuring the photon pulse's onset time which is dominated by noise in the APD signal.

The number of correlated photon events is found with a Gaussian fit of the electron-photon timing spectrum. A flat background was added to the Gaussian to subtract the uniform, uncorrelated photon background from the correlated peak. After background subtraction, a window was placed around the electron-photon timing peak sum all of the correlated events (correlated background and radiative decay signals). The signal-to-background for most runs was approximately 1/2. Calculation of the correlated backgrounds is discussed in chapter VI.

The photon energy spectrum is calibrated with ^{241}Am gamma ray and with the 511 keV peak in the raw spectrum. No lower photon energy cut was made, but the photon detector had a 15 keV detection threshold. A 340 keV upper energy cut was imposed because the photon event rate beyond 340 keV is dominated by background photons.

After application of the cuts and background subtraction described above, the rate of electron-delayed proton events R_{ep} and electron-delayed proton-photon events $R_{ep\gamma}$ is extracted. A summary of all of the cuts is given in table 4.1.

4.3 $R_{ep\gamma}/R_{ep}$ Ratio Extraction

The neutron beam delivered to the experiment can vary in magnitude, especially between beam cycles and periodic maintenance. There was no flux monitor installed

Cut	Range
Proton energy	2 FWHM
Electron energy	$\geq$ 35 keV
Photon energy	15 keV - 340 keV
electron-delayed proton time difference	2.5 μs - 20 μs
Electron-photon time difference	$>$ 2 FWHM
Electron-delayed proton baseline cut	Waveform returns to baseline

Table 4.1: Summary of all the cuts, hardware and software, used to extract R_{ep} and $R_{ep\gamma}$.

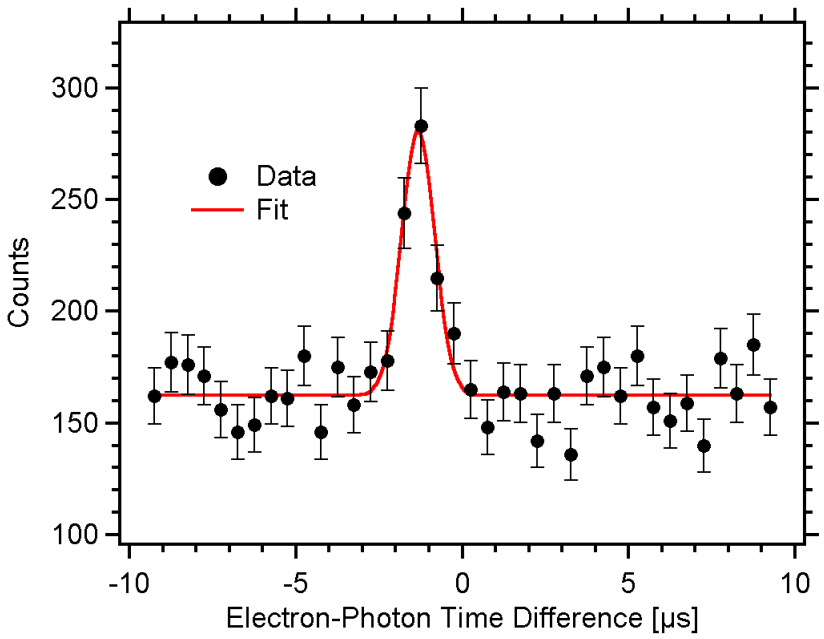

Figure 4.9: The electron-photon timing spectrum for a three-day run with the mirror at 1000 V. The spectrum shows all photons in a $\pm 10\,\mu$s window around the electron pulse. The peak is shifted from 0 time difference because of electronic delays between the APD and SBD. This is confirmed with pulser testing.

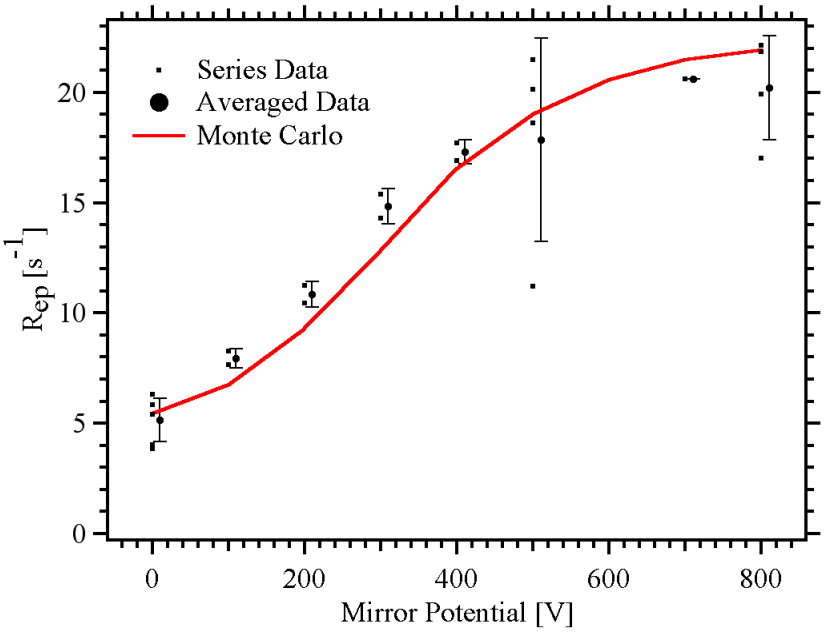

Figure 4.10: R_{ep} versus applied mirror voltage and the MC. The data are combined in a weighted average. The small dots are the series data, and because there are so many electron-delayed proton events, the statistical uncertainty is very small. The larger data point slightly to the right is the average of these points. The uncertainty for this point is the width of the distribution. Obviously, this is dominantly a systematic uncertainty and not statistical.

on the apparatus to measure the neutron flux rate. The rates R_{ep} and $R_{ep\gamma}$ are proportional to the $1/v$-weighted neutron flux where v is the neutron velocity. The weighting almost perfectly scales the decay probability within the finite decay region. Despite this difficulty, it is useful to compare the measured decay rates versus electrostatic mirror voltage to MC. Figure 4.10 shows R_{ep} versus applied mirror voltage, and figure 4.11 shows $R_{ep\gamma}$ versus applied mirror voltage. The values at each voltage are a weighted average, and all data above 750 V was averaged together at 800 V.

The $R_{ep\gamma}/R_{ep}$ ratio is created to eliminate the dependence on neutron flux seen in the absolute rates. The ratio method can cancel a constant detection efficiency in the SBD $\langle\epsilon_{\mathrm{SBD}}\rangle$. In reality, the efficiency for detection is a function of incident energy and impact angle $\epsilon(E_e, \theta)$, and a detailed simulation is required to calculate the detector response (such as in figure 4.8).

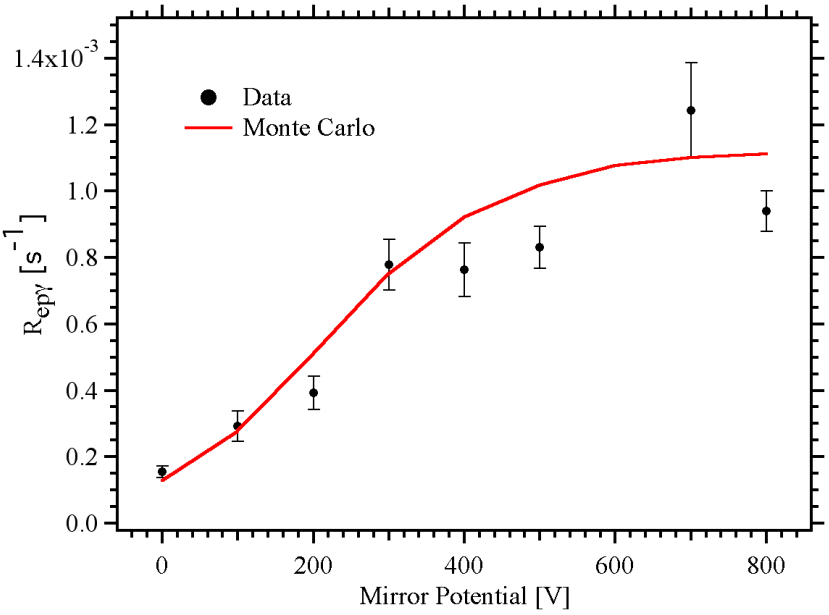

Figure 4.11: $R_{ep\gamma}$ versus applied mirror voltage and the MC. Due to the small number of events, the uncertainties are dominantly statistical.

The ratio was created for all 23 series, where each series was run at different electrostatic mirror potentials. Runs of the same the mirror potentials were repeated, sometimes several weeks apart. The ratio was determined at each voltage by a weighted average, and all runs with an electrostatic mirror voltage above 750 V were combined into the 800 V data point. The ratio data versus electrostatic mirror voltage was compared to MC, and this comparison is shown in figure 4.12. The generation of the MC data is discussed in chapter V.

As the electrostatic mirror voltage is increased, $R_{ep\gamma}$ and R_{ep} both increase due to the reflection of more protons that are anti-correlated to the detected electrons (figures 4.10 and 4.11), the ratio also increases (figure 4.12). When the electrostatic mirror is off, the detected electron and proton must to be correlated in emission direction since the mirror can't reflect the anti-correlated protons. The neutrino and photon are kinematically required to be emitted in the opposite hemisphere to conserve momentum. As the mirror voltage increases, the detected proton can now

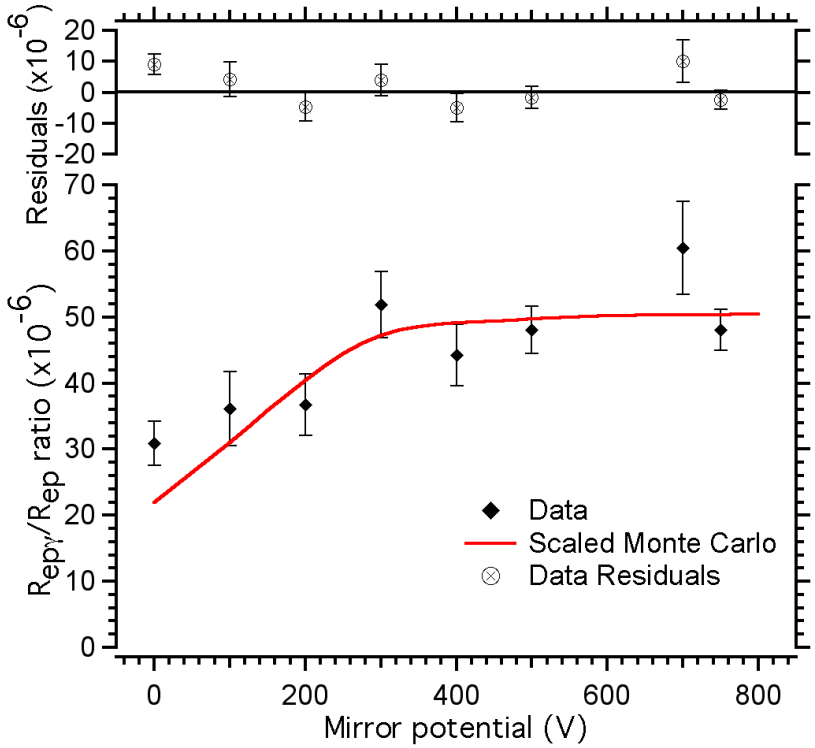

Figure 4.12: Plot of the ratio of the total number of electron-delayed proton-photon events above background to the total number of electron-delayed proton event versus the mirror potential.

be anti-correlated to the electron, which helps conserve momentum. This frees the photon from kinematic constraint. Furthermore, the dynamics of QED suggest that the angle between the emitted photon and electron peaks at 55° (in general photon production of forward-peak at all electron energies). At lower voltages, dynamic suppression occurs while at higher voltages, the photon is no longer constrained to be emitted opposite the electron (the primary source of IB).

The MC shape in figure 4.12 serves as a 1-parameter template to fit to the data. This parameter is an overall scaling factor which is the branching ratio for radiative decay. The fit to the ratio data yields a branching ratio of 3.18 $\times 10^{-3}$. The χ^2 for the fit is 12.8 per 7 degrees of freedom where the largest contribution to the χ^2 is the 0 V data. The uncertainty at 0 V is correlated to the potential from the 1400 V biased APD leaking into the decay region and causing electrostatic reflection of the protons. Another hypothesis is that the ratio is due to an uncorrelated background which implies that the ratio is flat. The χ^2 per degree of freedom for this hypothesis 3.2 versus 1.83 for the MC. The MC spectrum is the more likely of the two hypotheses.

The radiative decay, photon energy spectrum from 15 keV to 340 keV of the events that occur in the electron-photon timing peak may be determined by subtracting the photon energy spectrum of the background from that of the peak. The on-peak spectrum was obtained by summing the photon energy spectrum over the timing window peak in figure 4.9. The off-peak, background, photon energy spectrum was summed from the region outside of the timing window, and it was subtracted from the on-peak photon energy spectrum. Figure 4.13 shows the resulting photon energy spectrum after the subtraction. No corrections have been applied to these data to incorporate the photon detector response, but the deviation incurred is small. The uncorrected spectrum is in good agreement with theoretical predictions [57, 60].

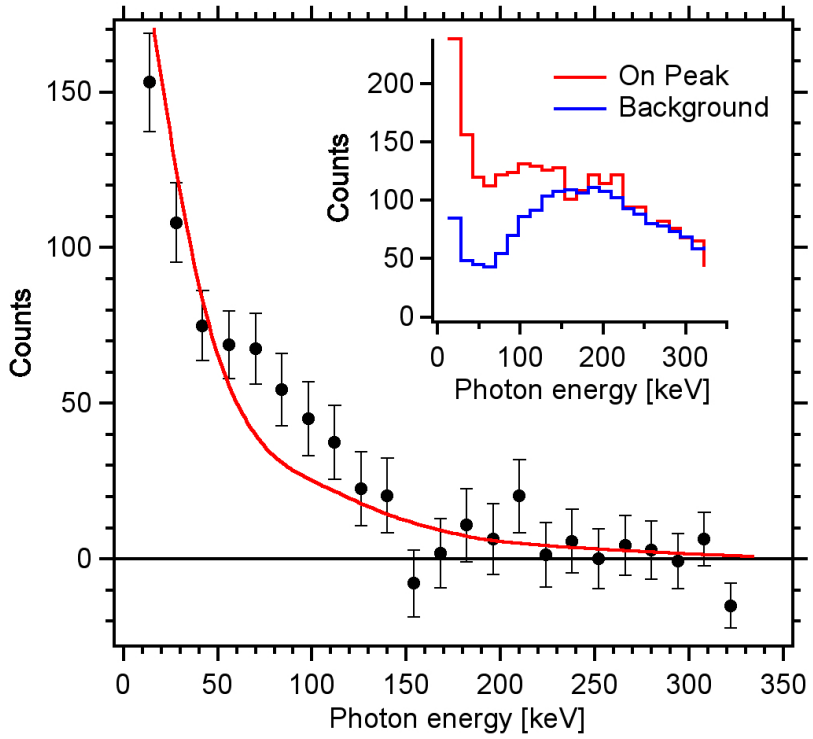

Figure 4.13: The photon energy spectrum that results from subtracting the off-peak energy spectrum from the on-peak energy spectrum. The inset shows the shape of the on-peak and off-peak spectra prior to the subtraction.

Series	V_{Mirror} (V)	Livetime (d)	e^- thresh. (keV)	$\langle R_{ep} \rangle$ (s^{-1})	$\langle R_\gamma \rangle$ (s^{-1})	$\langle R_{ep\gamma} \rangle$ ($\times 10^{-5}$ s^{-1})	Ratio ($\times 10^{-6}$)
87	0	5.7	40.8	5.40	0.030	23.2 ± 4.3	42.9 ± 7.9
92	0	2.8	41.1	5.42	0.029	19.7 ± 5.8	36.3 ± 10.7
93	200	4.2	40.3	10.44	0.053	30.9 ± 6.6	29.6 ± 6.4
94	300	1.9	40.2	14.28	0.071	76.8 ± 12.2	53.8 ± 8.5
96	400	2.4	39.2	16.91	0.083	69.5 ± 11.5	41.1 ± 6.8
97	500	2.2	37.4	18.63	0.091	92.8 ± 13.0	49.8 ± 6.9
99	1500	3.1	36.4	19.92	0.103	89.1 ± 11.1	44.7 ± 5.6
103	0	5.7	39.0	3.85	0.015	14.9 ± 4.0	38.7 ± 10.3
104	1500	2.9	35.5	17.00	0.061	60.7 ± 11.5	35.7 ± 6.8
105	0	8.6	41.3	4.03	0.016	10.7 ± 3.1	26.6 ± 7.8
106	500	2.3	43.7	11.20	0.039	61.3 ± 11.0	54.8 ± 9.8
110	1600	2.8	31.6	21.85	0.075	113.0 ± 13.7	51.7 ± 6.3
111	500	3.0	32.9	20.15	0.070	95.2 ± 12.9	47.3 ± 6.4
112	0	6.9	32.6	5.84	0.023	15.3 ± 4.3	26.3 ± 7.3
114	0	6.5	31.8	6.32	0.023	14.8 ± 4.5	23.5 ± 7.0
115	500	2.3	32.1	21.47	0.073	94.5 ± 14.7	44.0 ± 6.8
119	200	4.1	35.8	11.26	0.039	51.1 ± 7.9	45.4 ± 7.0
122	100	5.8	32.4	8.26	0.030	28.1 ± 5.6	34.0 ± 6.7
123	1000	2.9	32.2	22.12	0.075	129.9 ± 13.8	58.7 ± 6.2
124	300	3.9	35.8	15.39	0.054	78.4 ± 9.6	50.9 ± 6.3
125	700	2.5	36.6	20.61	0.072	124.4 ± 14.4	60.4 ± 7.0
126	400	3.2	33.9	17.70	0.059	83.1 ± 11.2	46.9 ± 6.3
127	100	3.0	37.3	7.66	0.029	31.2 ± 7.5	40.8 ± 9.9

Table 4.2: Characterization of the 23 data series used in the experiment. V_{Mirror} is the voltage applied to the electrostatic mirror; the lifetime is reported in total days; e^- thresh. is the measured electron threshold in keV for the series; $\langle R_{ep} \rangle$ is the average rate of valid electron-delayed proton triggers; $\langle R_\gamma \rangle$ is the average rate of photon events that have a valid electron-delayed proton trigger within a 51 μs window; $\langle R_{ep\gamma} \rangle$ is the average rate of photon events in the electron-photon timing window with a valid electron-delayed proton trigger after background subtraction (the rate of events in the peak of figure 4.9). The ratio $R_{ep\gamma}/R_{ep}$ is reported in the last column, and these values at the same voltage are averaged together to produce the data in figure 4.9.

CHAPTER V

Simulations

Calculation of the effective solid angle for proton, electron, and photon detection is complicated by the interplay of the electromagnetic fields. The crude estimate of a constant magnetic field and the electrostatic mirror being a perfectly narrow peak can reproduce the bulk features of the detector response, but misses subtleties important in a precision extraction of the branching ratio. This chapter focuses on the Monte Carlo (MC) simulation of the detector. The MC method is composed of three components: event generation, event tracking, and detector response. First, the decay particles must be generated based on the differential decay rates, and these rates were calculated in chapter II. Next, these generated particles, which are both relativistic and non-relativistic, must be tracked through the electromagnetic fields of the apparatus to the detectors. Finally, particles reaching their respective detector are counted, and any modification due to detector response must be simulated.

Each section focuses on these three parts of the MC method. Section 5.1 presents two methods of event generation whose results are very similar. Section 5.2 presents two methods of tracking charged particle motion through the electromagnetic fields. Each method can be applied, albeit with modification, to both the relativistic electron and the non-relativistic proton. Section 5.3 describes the methods used to

calculate the electromagnetic fields. Section 5.4 describes the software packages used to simulate the detector response. Finally, in section 5.5, some results of the MC method are shown. The MC can be used to explore different aspects of radiative decay that can be measured in the experiment, and aids in the development of future radiative decay experiments.

5.1 Event Generation

The differential decay rate is the rate that the neutron decays into a specified final state configuration. For example,

$$\frac{d^2\Gamma(x,y)}{dx\,dy} = P(x,y) \tag{5.1}$$

describes a hypothetical differential decay rate into a configuration given by x and y with bins of width dx and dy. In general, the differential decay rate is a function of n variables. For radiative decay $n = 8$, and for non-radiative decay $n = 5$. The total decay rate can calculated by integrating the n-dimensional differential decay rate over all parameter space. By normalizing the differential decay rate by the total decay rate, an n-dimensional probability distribution function (n-D PDF) is formed. Random events are require that properly sample the n-D PDF. There are a number of ways to sample the PDF, and two methods were employed in this analysis. Conditionally integrated sampling and von Neumann rejection were both used to generate events from the n-D PDF in the MC. This section describes these methods of event generation, and the output from each is very similar.

5.1.1 Conditionally integrated sampling

Conditionally integrated sampling seeks to generate n 1-D PDFs from the n-D PDF. The construction of each 1-D PDF is conditional to the selection of parameters

from the the previous 1-D PDFs. In conditionally integrated sampling, the n-D PDF (P_n) is integrated over all but one parameter, say x_n. A value x_n^* is sampled from this 1-D PDF by whatever method is most convenient e.g. von Neumann rejection, inverting the integral, etc. [6]. The next step is to integrate the n-D PDF over the remaining parameters (except x_{n-1} and x_n) conditional to the selection of $x_n = x_n^*$, leaving a 1-D PDF for x_{n-1}. This process is repeated until all n parameters are selected. The construction of the n 1-D PDFs (P_1) is

$$
\begin{aligned}
P_1(x_n) &= \left(\prod_{i=1}^{n-1}\int dx_i\right) P_n(x_1,\ldots,x_n) \\
P_1(x_{n-1}|x_n^*) &= \left(\prod_{i=1}^{n-2}\int dx_i\right) P_n(x_1,\ldots,x_{n-1},x_n^*) \\
&\vdots \\
P_1(x_1|x_2^*,\ldots,x_n^*) &= P_n(x_1,x_2^*\ldots,x_n^*).
\end{aligned}
\tag{5.2}
$$

This method is particularly useful for the lowest order non-radiative decay rate in equation 2.8. The radiative decay rate is complicated, and an exact analytic form for the 1-D PDFs is difficult to obtain by direct integration. With approximations though, these integrals can be formed [106]. It turns out that these approximations are valid, as the spectra derived from this method are similar to von Neumann rejection, described below.

5.1.2 von Neumann rejection

The von Neumann rejection is very simple to implement, but can be inefficient for PDFs with large peaks in the accepted phase space of events. The simplest application of von Neumann rejection is to reject events against a constant value, the upper bound for the n-D PDF. Because there is a photon energy threshold ω_t, the n-D PDF given in equation 2.29 has an upper bound M

To generate MC data, a sample event is generated uniformly in the available phase space, subject to conservation of energy / momentum. For radiative decay, the differential decay rate is

$$\frac{d^8\Gamma}{dE_e d\Omega_e d\omega d\Omega_\gamma d\Omega_{\bar{\nu}}} = P_8(E_e, \cos\theta_e, \phi_e, \omega, \cos\theta_\gamma, \phi_\gamma, \cos\theta_{\bar{\nu}}, \phi_{\bar{\nu}}). \tag{5.3}$$

To generate events uniformly in phase space, the electron, photon, and neutrino directions are each distributed uniformly into 4π solid angle. This requires that the cosine of the azimuth angle θ is uniformly distributed in range $[-1, 1]$, and that the axial angle ϕ is uniformly distributed in range $[-\pi, \pi]$. The electron energy is distributed uniformly from m_e to its endpoint energy E_0 where

$$E_0 = \frac{m_n^2 - m_p^2 + m_e^2}{2m_n} \approx 1.3\text{MeV}. \tag{5.4}$$

The photon energy ω is distributed uniformly in the range $[\omega_t, \omega_{\max}]$ where ω_t is the detector's lower threshold and $\omega_{\max}$ is the upper limit. With these parameters selected, the neutrino energy can be calculated,

$$E_{\bar{\nu}} = \frac{m_n^2 - m_p^2 + m_e^2 - 2m_n(E_e + \omega) - 2|\mathbf{p}_e|\omega\cos\theta_{e\gamma}}{2(m_n - E_e - \omega + |\mathbf{p}_e|\cos\theta_{e\bar{\nu}} + \omega\cos\theta_{\bar{\nu}\gamma})}, \tag{5.5}$$

where θ_{ij} is the angle between species i and j. This result is valid for non-radiative decays by setting $\omega = 0$. For a given E_e, the condition that $E_{\bar{\nu}} \geq 0$ is satisfied for ω below some upper limit. The numerator of equation 5.5 can be written as $A - B\omega$ where $A, B \geq 0$. The denominator is never singular because $m_n \gg E_0, \omega$, and the upper limit on ω is easily calculable. Because the denominator is never singular, the upper limit on ω is easily calculable. The conservation of energy / momentum can be used to calculate the proton energy and momentum. The kinematics analysis is easily generalized to any number of photons in the final state.

This procedure samples the kinematically available phase space uniformly, and the probability P is calculated from equation 5.3. The ratio $P/M \leq 1$, and a random number $r \in [0, 1]$ is generated and used to accept (reject) the candidate event.

5.2 Tracking

The trajectories of the electron, proton, and photon are calculable, but each particle requires its own, distinct tracking routine. The trajectories of the electron and proton are dependent upon the strong electromagnetic fields in the apparatus, but the photon travels in straight line paths that are undeviated by these fields. In this section, two separate tracking methods for the electron and proton are discussed.

A particle's trajectory can be calculated by integrating its differential equations of motions given its initial starting position, energy, and emission direction. Integrating the differential equation can be made arbitrarily precise by taking smaller time steps in the trajectory calculation. A 4^{th}-order Runge-Kutta is used to integrate the equations of motion. This method can be made very accurate by taking very small time steps, but this occurs at the expense of computation time.

There is an alternative to a brute force integration of the equations of motion. The charged particles are in cyclotron orbits around the magnetic fields which constrains the transverse components of momentum. The particles can be assume to travel on a magnetic field line with the longitudinal momentum being determined from a 1-D potential. This approximation works if the change in the field is small over the period of a cyclotron orbit. This method is also computationally less intensive, but second order drift effects are neglected in this approximation.

5.2.1 Runge-Kutta

A differential equation for the function $x(t)$

$$\frac{dx(t)}{dt} = f(t,x) \quad \text{with} \quad y(t_0) = y_0 \tag{5.6}$$

as initial conditions can be solved by evaluating the finite difference approximation of the derivative at small time steps h and calculating the new $x(t+h)$. The differential equation can be solved with a 4^{th}-order Runge-Kutta. The solution to the sample differential in equation 5.1 is

$$\begin{aligned} k_1 &= hf(t,x) \\ k_2 &= hf(t+h/2, x+k_1/2) \\ k_3 &= hf(t+h/2, x+k_2/2) \\ k_4 &= hf(t+h, x+k_3) \\ x(t+h) &= \frac{1}{6}(k_1+2k_2+2k_3+k_4). \end{aligned}$$

This solution is easily realized in software [107]

Because the proton's kinetic energy < 1 keV, the equations of motion are the non-relativistic Lorentz force law, and its equations of motion in the lab frame are

$$\begin{aligned} \frac{d\mathbf{v}}{dt} &= \frac{q}{m}(\mathbf{E} + \mathbf{v} \times \mathbf{B}) \\ \frac{d\mathbf{x}}{dt} &= \mathbf{v}. \end{aligned} \tag{5.7}$$

The position $\mathbf{x}$ and velocity $\mathbf{v}$ can be solved by inputting parameters q and m which are the charge and mass of the proton and $\mathbf{E}$ and $\mathbf{B}$ which are the electric and magnetic fields. The relativistic electron can also be solved with 4^{th} order Runge-Kutta, but the Lorentz equation must be modified (in the lab frame). To derive the appropriate equations of motion, the relativistically covariant formulation is required [55],

$$\frac{dU^\alpha}{d\tau} = \frac{q}{mc} F^{\alpha\beta} U_\beta \quad \text{where} \quad U^\alpha = \left(U^0, \mathbf{U}\right)^{\mathrm{T}}. \tag{5.8}$$

The matrix components in terms of laboratory measurable parameters are

$$F^{\alpha\beta} = \begin{pmatrix} 0 & -E_x & -E_y & -E_z \\ E_x & 0 & -cB_z & cB_y \\ E_y & cB_z & 0 & -cB_x \\ E_z & -cB_y & cB_x & 0 \end{pmatrix} \quad \text{and} \quad U^{\alpha} = \gamma \begin{pmatrix} c \\ v_x \\ v_y \\ v_z \end{pmatrix}. \tag{5.9}$$

where $\gamma = 1/\sqrt{1 - v^2/c^2}$. These equations can be written out in time and space components,

$$\begin{aligned} \frac{d\mathbf{U}}{d\tau} &= \frac{q}{mc}\left(U^0\mathbf{E} + \mathbf{U}\times c\mathbf{B}\right) \\ \frac{dU^0}{d\tau} &= \frac{q}{mc}\left(\mathbf{U}\cdot\mathbf{E}\right) \end{aligned} \tag{5.10}$$

where τ is the proper time (time in particle's rest frame) and t is the lab time. The times are related by $t = \gamma\tau$. Replacing $d/d\tau$ with $\gamma d/dt$ and the 4-velocity terms with 3-velocity terms and canceling factors of c and γ, we have

$$\begin{aligned} \frac{d}{dt}(\gamma\mathbf{v}) &= \gamma\frac{d\mathbf{v}}{dt} + \frac{d\gamma}{dt}\mathbf{v} = \frac{q}{m}\left(\mathbf{E} + \mathbf{v}\times\mathbf{B}\right) \\ \frac{d\gamma}{dt} &= \frac{q}{mc}\left(\mathbf{E}\cdot\frac{\mathbf{v}}{c}\right). \end{aligned} \tag{5.11}$$

Substituting the second equation into the first, the relativistically modified Lorentz force law in the lab frame for a charged particle is

$$\begin{aligned} \frac{d\mathbf{v}}{dt} &= \frac{q}{m\gamma}(\mathbf{E} - (\mathbf{E}\cdot\frac{\mathbf{v}}{c})\frac{\mathbf{v}}{c} + \mathbf{v}\times\mathbf{B}) \\ \frac{d\mathbf{x}}{dt} &= \mathbf{v}. \end{aligned} \tag{5.12}$$

The integration of the 4^{th}-order Runge-Kutta with an accurate electromagnetic field map automatically incorporates all the drifts mechanisms of the cyclotron center of motion such as $\mathbf{E}\times\mathbf{B}$, $\nabla\mathbf{B}$, etc. These drift mechanisms are included in the integrated solution, but the majority can safely be neglected. By neglecting the drifts, a new tracking algorithm presents itself.

5.2.2 Adiabatic transport

A charged particle in cyclotron motion rotates around a magnetic field line, and any component of momentum along this field line tends to transport the particle longitudinally along the field line. An alternative to integration of the equations of motion is to trace the magnetic field line to determine its possible trajectory. A charge in cyclotron motion can be considered an electrical current loop with a magnetic moment μ associated with it, but μ should not be confused with the intrinsic magnet moment of the particle. The parameter μ is an adiabatic invariant because the magnetic field in the apparatus is non-zero and very uniform over a cyclotron orbit. The particle's longitudinal motion along the magnetic field line can be described with a 1-D potential.

The adiabatic invariant for the proton is

$$\mu = \frac{p_{\perp}(\mathbf{x})^2}{2mB(\mathbf{x})} \tag{5.13}$$

where $p_{\perp}(\mathbf{x})$ is the magnitude of the momentum (non-relativisitic) perpendicular to the magnetic field [55]. The adiabatic condition implies that μ is constant for the entire trajectory, and μ can be evaluated at the proton's initial position $\mathbf{x_0}$. The 1-D potential for the longitudinal momentum is

$$p_{\parallel}^2(\mathbf{x}) = 2m\left[E_0 - \mu B(\mathbf{x}) - qU(\mathbf{x})\right] \tag{5.14}$$

where $U(\mathbf{x})$ is the electrostatic potential, and E_0 is the proton's initial kinetic energy.

The adiabatic invariant μ can also be defined for the relativistic electron, and a 1-D longitudinal potential can be created. The relativistic electron's adiabatic invariant is $\mu = p_{\perp}(\mathbf{x})^2c^2/B(\mathbf{x})$ where the momentum is relativistically correct [55]. Again, because μ is considered invariant, it can be evaluated at the electron's initial

position $\mathbf{x_0}$. The potential is

$$p_{\parallel}(\mathbf{x})^2c^2 = E(\mathbf{x})^2 - \mu B(\mathbf{x}) - m^2c^4. \tag{5.15}$$

For an electron originating at $\mathbf{x_0}$, the energy of the particle $E(\mathbf{x}) = E_0 - qU(\mathbf{x})$ where $E_0 = \sqrt{|\mathbf{p}(\mathbf{x_0})|^2 + m^2c^4} + qU(\mathbf{x_0})$ is the initial total energy.

The total energy in a magnetic field is conserved because it does no work on a particle. Therefore, the total energy in the longitudinal component and the transverse component is conserved. If μ is constant (adiabatic), then a particle traveling towards a region of higher magnetic field gains energy in its transverse mode from the longitudinal mode. A large enough magnetic field change requires the complete loss of energy in longitudinal mode, and the particle changes direction. This effect is the magnetic mirror effect.

Conversely, a particle traveling into a weaker magnetic field requires that the longitudinal component gains energy from the transverse component. Traveling into a weak enough magnetic field effectively transfers all of a particle's energy from the transverse mode to the longitudinal mode. Incidentally, transferring energy to the longitudinal mode is an effective way to reduce particle backscattering from detectors [103, 104].

Transferring a particle's energy to its longitudinal mode (and vice versa) can be understood with Gauss' Law. For a uniform magnetic field in the $+z$ direction, a particle undergoes cyclotron motion in the $r - \theta$ plane, and the component of momentum in the z direction is uncoupled from the magnetic field. When the magnetic field increases (decreases) in magnitude, $\nabla \cdot \mathbf{B} = 0$ requires radial components of the magnetic field to exist to converge (diverge) the magnetic field lines. These radial components couple the transverse mode to the longitudinal mode.

5.2.3 Drift mechanisms

The center of the cyclotron motion follows the magnetic field line in the adiabatic limit, but it can drift to other field line through drift forces. A discussion of the drift mechanisms is most transparent in the non-relativistic limit. Any force field $\mathbf{F}$ can be split into components that are parallel and perpendicular to the magnetic field direction, $\mathbf{F}_{\parallel}$ and $\mathbf{F}_{\perp}$. The equation of motion is,

$$\frac{d\mathbf{v}}{dt} = \mathbf{F}_{\parallel} + \mathbf{F}_{\perp} + q\mathbf{v} \times \mathbf{B}. \tag{5.16}$$

$\mathbf{F}_{\parallel}$ accelerates the particle along the direction of $\mathbf{B}$ (assuming the velocity remains non-relativistic). $\mathbf{F}_{\perp}$ tends to accelerate the particle perpendicular to $\mathbf{B}$, contributing to the $\mathbf{v} \times \mathbf{B}$ term. The particle maintains its cyclotron motion but its center of rotation drifts with velocity $\mathbf{v_d}$. It is

$$\mathbf{v_d} = \frac{1}{q}\frac{\mathbf{F} \times \mathbf{B}}{|\mathbf{B}|^2}. \tag{5.17}$$

$\mathbf{F}$ can be any force acting on the charged particle such as the electric field ($\mathbf{F} = q\mathbf{E}$), gravity, centripetal forces, and magnetic field gradients ($\mathbf{F} = -\mu\nabla\mathbf{B}$). Magnetic field gradients along the direction of the magnetic field have already been considered and result in the magnetic mirror effect.

5.3 Electromagnetic Field Calculation

Simulation of the electron and proton trajectories requires an accurate, fine mesh field map for the magnetic field and the electrostatic field. The magnetic field is calculated with a commercial software package Biot-Savart [108]. The software operates by numerically integrating the Biot-Savart law over a set of specified coil and wire configurations. The calculation is very accurate because there are no magnetic materials in the magnet bore. The coil configurations are known very precisely from the

magnet construction drawings. The coil configuration for the superconducting magnet is given in Appendix B. To calculate the electrostatic fields from the electrostatic mirror, a solver was written from first principles, and it is described below.

In the experimental setup, the superconducting magnet bore is evacuated, and no significant free charge is expected to accumulate anywhere. Laplace's equation can be used to solve for the electrostatic potential from the electrostatic mirror. The 9.5° bend at the upstream end of the bore is far enough from the electrostatic mirror, and cylindrical symmetry is assumed a good symmetry.

To solve Laplace's equation, a finite differences method (FDM) approach was pursued due to its simplicity and rapid prototyping ability. This is in contrast to other, mature solution techniques such as finite element analysis or boundary element analysis. FDM discretizes the solution space and approximates the derivatives as finite differences between grid points. The application of boundary conditions leads to a linear system that is completely specified and yields a unique solution. FDM method requires the geometry to be bounded to ensure convergence.

Laplace's equation in cylindrical coordinates with cylindrical symmetry (no θ dependence) is

$$\nabla^2\phi = \frac{1}{\rho}\frac{\partial\phi}{\partial\rho} + \frac{\partial^2\phi}{\partial\rho^2} + \frac{\partial^2\phi}{\partial z^2} = 0. \tag{5.18}$$

where $\phi \equiv \phi(\rho, z)$ is the electrostatic potential. To numerically solve Laplace's equation, the 2-D space is first discretized onto a grid over ρ and z. The grid can be variable in size with spacings $\Delta\rho(\rho, z)$ and $\Delta z(\rho, z)$ that are a function of position, but this discussion assumes the spacings $\Delta\rho$ and Δz are constant.

Symmetric finite differences are used to approximate the derivatives, and these are applied to equation 5.18. The discretized Laplace's equation valid for non-boundary,

interior points is

$$\begin{aligned}\nabla^2\phi(\rho,z) &\approx \frac{1}{2\rho\Delta\rho}\left(\phi(\rho+\Delta\rho,z)+\phi(\rho-\Delta\rho,z)\right)\\ &+ \frac{1}{(\Delta\rho)^2}\left(\phi(\rho+\Delta\rho,z)+\phi(\rho-\Delta\rho,z)-2\phi(\rho,z)\right)\\ &+ \frac{1}{(\Delta z)^2}\left(\phi(\rho,z+\Delta z)+\phi(\rho,z-\Delta z)-2\phi(\rho,z)\right)=0. \qquad (5.19)\end{aligned}$$

Points at $\rho = 0$ present a problem due to $1/\rho$ divergence, but the potential remains finite and continuous. Evaluating the inner boundary at $\rho = \epsilon$ for $\epsilon \ll \Delta\rho$ and using continuity, the potential is

$$\phi(\epsilon,z) \approx \phi(0,z) + \epsilon\frac{\partial\phi(0,z)}{\partial\rho}. \qquad (5.20)$$

Now, the second line in equation 5.19 is negligible, and using the one-sided derivative, Laplace's equation at $\rho = \epsilon$ is

$$\begin{aligned}\nabla^2\phi(\epsilon,z) &\approx \frac{1}{\epsilon\Delta\rho}\left(\phi(\epsilon+\Delta\rho,z)-\phi(\epsilon,z)\right)\\ &+ \frac{1}{(\Delta z)^2}\left(\phi(\epsilon,z+\Delta z)+\phi(\epsilon,z-\Delta z)-2\phi(\epsilon,z)\right)=0. \qquad (5.21)\end{aligned}$$

Figure 5.1 shows the cylindrical geometry with grid spacings and $\rho = \epsilon$ condition. Laplace's equation has been transformed into a set of linear equations where the potential at a given point $\phi(\rho, z)$ is a function of its nearest neighbors. The solution is found by simultaneously solving these linear equations with the boundary conditions.

5.3.1 Implementing dielectrics

Equation 5.18 can be generalized to incorporate dielectric materials. Assuming the dielectric is a linear material with dielectric constant ϵ, the electromagnetic displacement $\mathbf{D}$ is related to the electric field by $\mathbf{D} = \epsilon\mathbf{E}$. In a charge-free region, Gauss's law is $\nabla \cdot \mathbf{D} = 0$. Because the electric field is derivable from a potential (even inside of materials), the modified Laplace's equation is

$$\nabla\left[\epsilon(\mathbf{x})\nabla\phi(\mathbf{x})\right] = \epsilon(\mathbf{x})\nabla^2\phi(\mathbf{x}) + \nabla\epsilon(\mathbf{x})\cdot\nabla\phi(\mathbf{x}) = 0. \qquad (5.22)$$

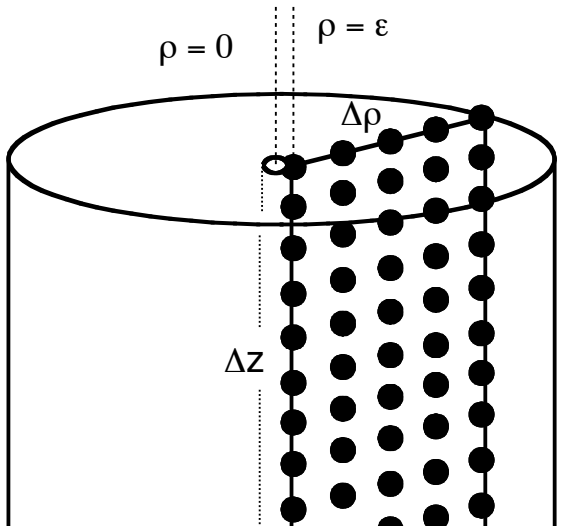

Figure 5.1: The 2-dimensional, axially symmetric, cylindrical geometry applicable to the experiment.

To incorporate dielectrics into the program, the dielectric fills the volume that is defined by the neighboring potential grid points. The value of the dielectric at a particular grid point is the volume average of the surrounding dielectric neighborhoods. Cylindrical geometry requires a radial weight when calculating the dielectric at a grid point, and this geometry is shown schematically in figure 5.2.

5.3.2 Solving the lattice

If all the points are enumerated from 1 to N, an $N \times N$ matrix can be created that represents the linear relationships resulting from equation 5.18 and equation 5.22. The matrix for the linear equations is sparsely non-zero because only nearest neighbors are considered. There is also a high degree of symmetry with non-zero elements forming diagonal bands in the matrix. Sparse, banded matrices are easily invertible, and with the surrounding boundary conditions, a solution is obtained.

N must be very large to cover the large volume and to calculate a high resolution field map, and the $N \times N$ matrix is very large. This requires $N \times N$ points to be stored in memory, most of them zero. An iterative approach that operates on only the N

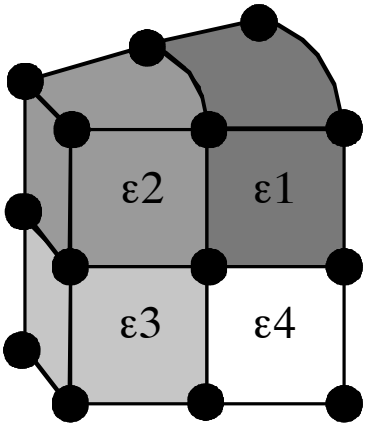

Figure 5.2: Schematic of the volume average dielectric constant for the center point. Despite reducing the problem to two dimensions, a proper cylindrical volume average must be used.

points is preferred for high resolution. One solution is to scan across the the N points, adjusting the potential at each point based on its nearest neighbors. Convergence is generally slow in this approach, but convergence speed can be improved by "over-relaxing."

Successive over-relaxation (SOR) is an iterative process where the correction added to the existing potential is over-estimated in order to speed up convergence [109]. At the i^{th} iteration, the existing potential is $\phi^i(\rho, z)$, and the calculated potential due to nearest neighbors is V. Using SOR, the value of the potential at the next step in the iteration is

$$\phi^{i+1}(\rho, z) = \phi^i(\rho, z) + \lambda \left(V - \phi^i(\rho, z)\right) \tag{5.23}$$

where $\lambda \in [1, 2)$. The value λ that gives the best convergence is generally a complicated function of the geometry and spacing.

5.4 Detector Response

The lowest order MC simulation of the experimental apparatus assumes an ideal detector response. This means that the detector has 100 % efficiency, perfect timing resolution, and perfect energy resolution. The lowest order MC does not incorporate the effects of backscattering, Compton scattering, etc. An event that crosses into the detector deposits the entirety of its energy into the detector. The analysis cuts in the MC are hard cuts with no detector resolution or uncertainty. For example, the photon energy cut (15 keV to 340 keV) is implemented in MC by only generating photon events in this energy region. In reality, it is possible that some 13 keV photons are detected because of the detector resolution.

A variety of MC packages are used to simulate the departures from an ideal detector. To consider the electron energy deposit spectrum and backscattering, the SBD is simulated with both MCNP5 and Penelope. For the proton energy deposit spectrum and backscattering, SRIM-2006 [110] was used to simulate the SBD. Because the photons are not constrained by the magnetic field, they can scatter off all extraneous material before depositing energy in the BGO. MCNP5 is used to calculate the systematic correction to the total energy deposit spectrum.

Because the uncertainties are of the order of 1 %, the higher order resolution and scattering effects are not incorporated in the MC that generates the $R_{ep\gamma}/R_{ep}$ ratio. These effects are included as systematic corrections and uncertainties. The description of the detector response MC used to calculate the systematic uncertainties is discussed in chapter VI.

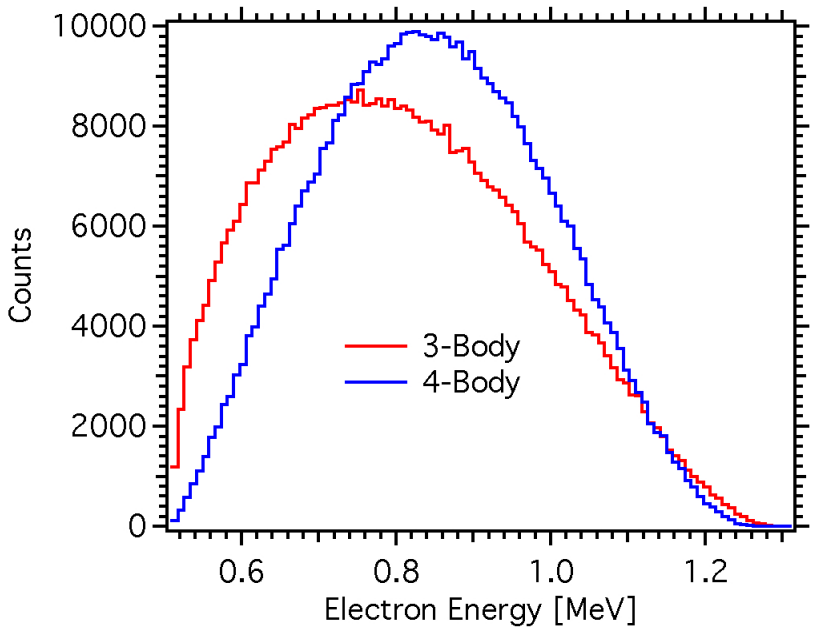

Figure 5.3: Decay energy spectrum of the electron for radiative and non-radiative decays calculated with MC. It is noted that this is the total energy of the electron; the spectrum starts at the electron rest energy 0.511 MeV.

5.5 Results

In this section, the MC is used to investigate various features of the decay. It does not attempt to be comprehensive, but it is instructive to understanding the salient differences (and similarities) between the non-radiative and the radiative decays. All the 4-body events are generated for photons with energy 15 keV to 340 keV which corresponds to the photon energy sensitivity of the photon detector.

The radiative and non-radiative differential decay rates in equations 2.29 and 2.8, respectively, can be integrated with the MC to produce the decay energy spectrum for each particle. The decay energy spectrum for the electron (figure 5.3), proton (figure 5.4), and antineutrino (figure 5.5) were generated from 5×10^5 total MC events. It is interesting to note how the much the electron (and antineutrino) spectrum changes when going from non-radiative to radiative decays while the proton spectra are very similar.

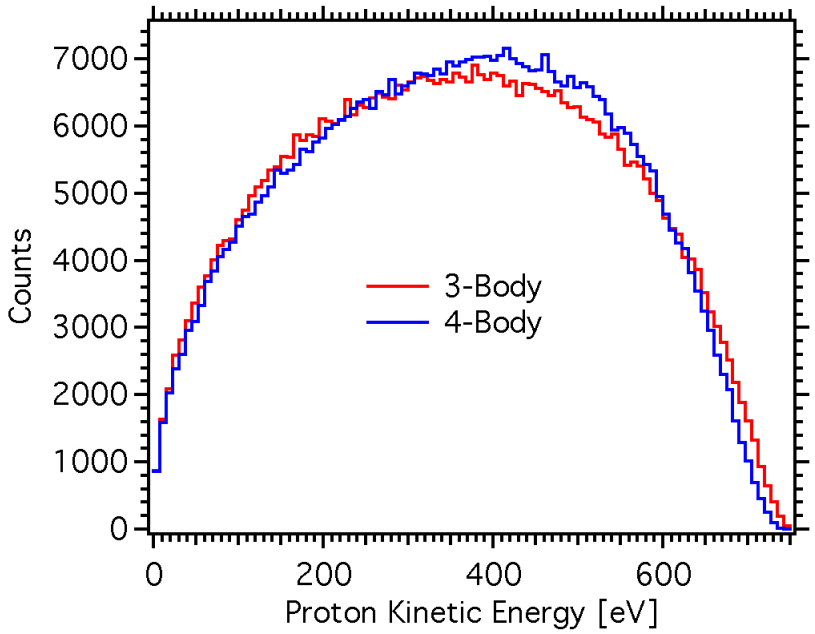

Figure 5.4: Decay kinetic energy spectrum of the proton for radiative and non-radiative decays. The centroids of these spectra are shifted by only 0.5 eV.

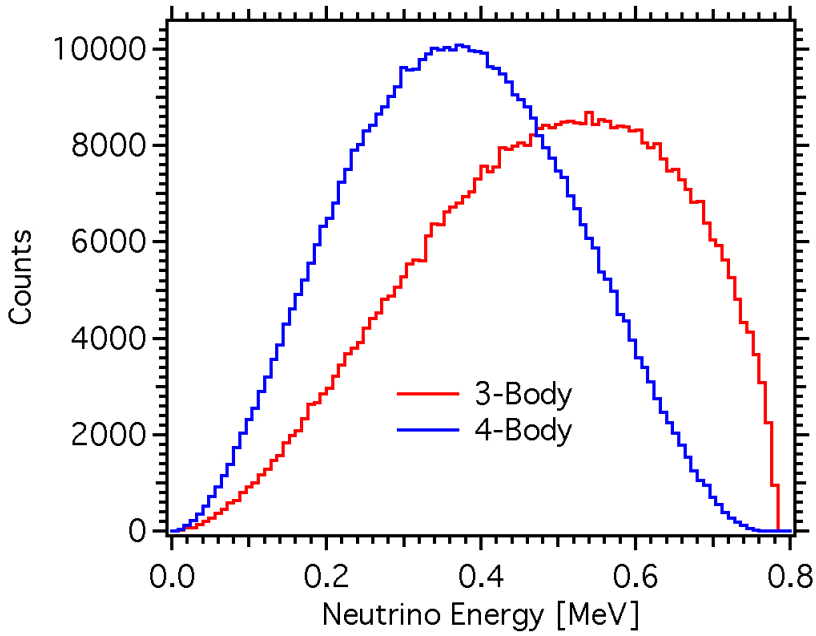

Figure 5.5: Decay energy spectrum of the antineutrino for radiative and non-radiative decays calculated with MC.

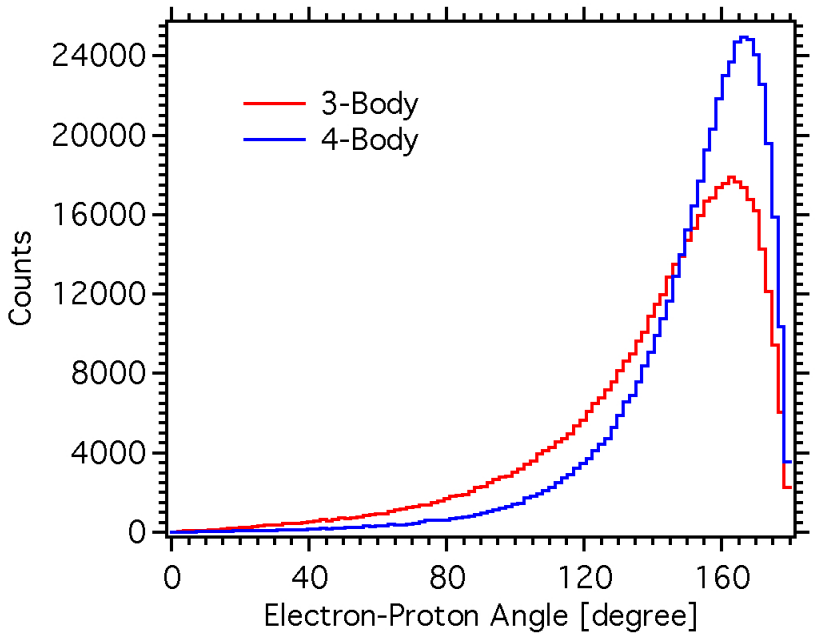

Figure 5.6: Electron-delayed proton emission angle for radiative and non-radiative decays. The radiative decays are peaked at a larger angle than the non-radiative decays. This leads to an increasing $R_{ep\gamma}/R_{ep}$ ratio for increasing electrostatic mirror voltage.

The heavy, recoil proton is important in conserving momentum for the decays despite having very little kinetic energy. The opening angle between the electron and proton is an important parameter in both radiative and non-radiative decays. These angular distributions have an important connection to the shape of the $R_{ep\gamma}/R_{ep}$ ratio. The MC calculating the distribution of opening angles and is shown in figure 5.6. The electron-proton opening angle in radiative decays are are more probable at larger angles than non-radiative decays. This means that as the electrostatic mirror voltage is increased, the detection rate for radiative decays increases faster than the detection rate for non-radiative decay. The shape of the $R_{ep\gamma}/R_{ep}$ ratio in figure 4.12 follows this trend.

The angular correlation of the electron and the photon is shown in figure 5.7. It peaks near 50° which agrees with the classical treatment in equation 2.25.

The experimental apparatus doesn't measure the decay spectrum shown in the

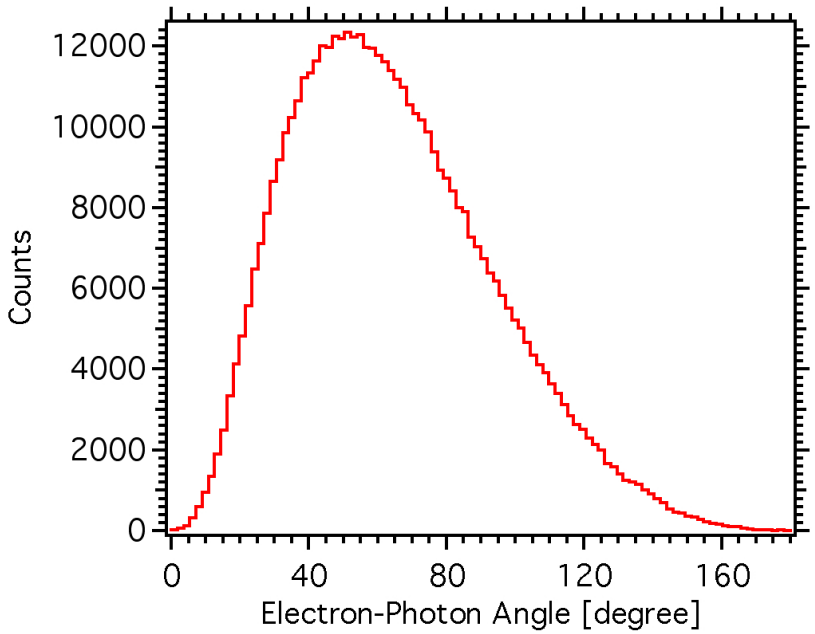

Figure 5.7: Electron-photon emission angle for radiative decays. These events are for photons with energies from 15 keV to 340 keV.

previous MC calculations. Figures 5.8 and 5.9 shows that the detected electron spectrum is a function of electrostatic mirror voltage for non-radiative and radiative decays, respectively. The measured electron spectrum is modified by detector response, but the measured spectrum is similar to the MC spectrum. Figure 5.10 shows the proton kinetic energy spectrum that gets accelerated into the SBD. The detector noise washes out any energy information, so the measured proton spectra do not resemble the raw MC spectra. These MC spectra are for valid electron-delayed proton events, and they are not particle singles simulations.

As the mirror voltage increases, the relative count rate for high energy electrons and protons increases. This is because the higher energy events must recoil at large angles off of each other. Because all of the electrons must be emitted upstream to be detected, the high energy protons must be emitted downstream. This requires a large electrostatic mirror voltage to reflect the protons. As the mirror voltage increases, the number of photon events increases, but the spectrum shape does not

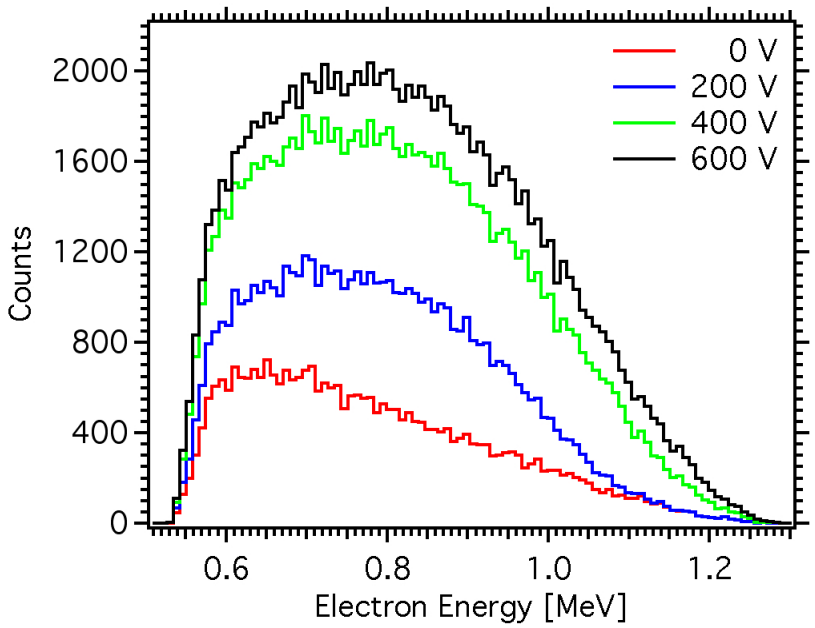

Figure 5.8: Non-radiative decay electron energy spectrum that enters the SBD as a function of applied electrostatic mirror voltage. No detector response has been incorporated in this lowest-order MC.

change significantly from the raw MC in figure 2.8.

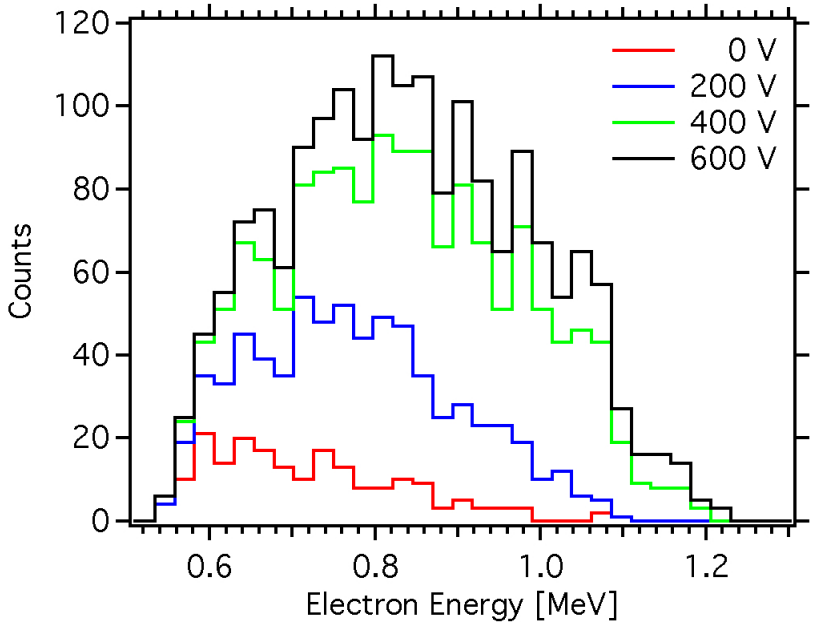

Figure 5.9: Radiative decay electron energy spectrum that enters the SBD as a function of applied electrostatic mirror voltage. No detector response has been incorporated in this lowest-order MC. The low number of events is because a photon is also required for an event to be counted.

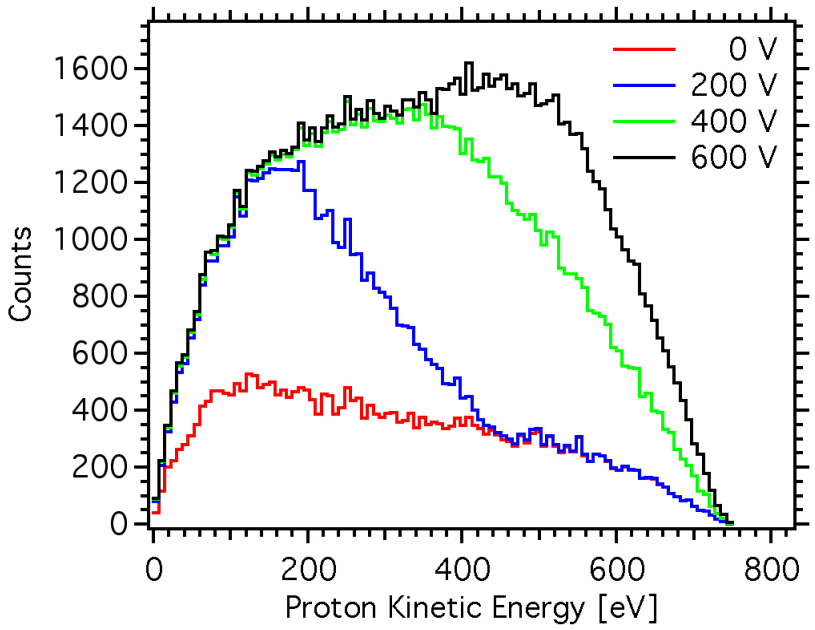

Figure 5.10: Non-radiative decay proton kinetic energy spectrum that strikes the SBD as a function of applied electrostatic mirror voltage. The radiative decay spectra versus electrostatic mirror voltage are very similar. The SBD noise washes out any spectral information in the measured spectra.

CHAPTER VI

Systematics

This chapter describes the systematic effects that affect the experiment. These systematic corrections and uncertainties modify the measured value of the branching ratio. The corrections are organized into five sections that discuss systematics related to the photon detector, SBD calibration, analysis cuts, correlated backgrounds, and the model used for the Monte Carlo simulation (MC). Table 6.1 summarizes the known systematic corrections, systematic uncertainties, and the section where each are discussed. The corrections and uncertainties are reported in percent of the measured branching ratio where the branching ratio was extracted in chapter IV from fitting the MC to the ratio data. Also, the uncertainty in the branching ratio from the fit was 3.4 %.

6.1 Photon Detector Uncertainties

The largest systematic uncertainty arises from the inexact knowledge of the behavior of the photon detector's low-energy threshold. The MC uses hard cuts and perfect resolution when calculating the $R_{ep\gamma}/R_{ep}$ ratio versus electrostatic mirror voltage which is used to extract the branching ratio. The real detector has resolution and gain drifts lead to an uncertainty in the actual value for the threshold. The detector does not have perfect efficiency which leads to incomplete energy deposition

Source of Uncertainty	Correction (%)	Uncertainty (%)	Section
Photon Detector			6.1
Gain drift & resolution	-2.5	7.0	6.1.2
Photon detector efficiency	+3.0	3.0	6.1.3
Charged Particle Energy			6.2
Electron energy threshold	0.0*	1.5	6.2.2
Proton energy	0.0*	< 0.05	6.2.3
Timing Cuts			6.3
Electron-delayed proton timing	0.0*	2.0	6.3
Electron-photon timing	0.0*	2.0	6.3
Correlated Backgrounds			6.4
Electron bremsstrahlung	-3.0	3.0	6.4.1
Electronic artifacts	-0.5	0.5	6.4.2
Model Uncertainties			
Beam divergence/profile	0.0*	3.0	6.5.1
B field registration	0.0*	2.0	6.5.1
Mirror registration	0.0*	1.0	6.5.1
APD bias leakage	0.0*	1.0	6.5.2
Electron backscattering	+0.2	0.5	6.5.3
Monte Carlo statistics	0.0*	2.0	6.5
Total Systematic	-2.8	9.8	
Fit Uncertainty		3.4	

Table 6.1: Summary of the systematic corrections and uncertainties for the measured branching ratio. The origin of each quantity is discussed in the section indicated in the table. 0.0* means that the systematic corrections are less than 0.05 % in magnitude but not identically zero.

for high energy photons. The detector also is surrounded by the magnet bore which scatter correlated photons back into the detector that should not have been counted.

The uncertainties in the photon detector can be separated into uncertainties at the 15 keV detector threshold and the detector efficiency. The threshold effects are intimately connected to the photon detector calibration which is described below in section 6.1.1. The threshold effects are due to gain drifts and the energy resolution and are discussed in section 6.1.2. Finally, the the detector efficiency is described in section 6.1.3.

6.1.1 Photon detector calibration

The gain of the photon detector varied from series to series during experimental operation, and this affects the measured lower energy threshold. Gain shifts occur primarily from the nonlinearity in the APD [4], and this gain is strongly affected by both the APD's bias voltage and surrounding temperature.

The photon detector energy response was calibrated *in situ* using the 60 keV line from ^{241}Am and the 511 keV line from pair production as shown in figure 3.9. The 511 keV photon is produced as a constant background from beam-related particles and served as a constant gain monitor throughout a run. A photon is only recorded with an electron-delayed proton trigger, and by examining table 4.2, the total photon rate is suppressed to approximately 0.5 s^{-1}. This low rate requires approximately one day to acquire enough counts to determine the calibration point. In addition to the 511 keV line, there is a broad 160 keV feature in the photon spectrum. This feature is primarily due to the backscattering of higher energy photons into the photon detector [71], and it was used as gain monitor with the 511 keV line.

The data were acquired using two photon energy windows. The runs from series 87 through 99 detected photons with energy up to approximately 800 keV. From series 103, the photon energy window was reduced to approximately 350 keV because there were no detectable events at those higher energies given the detector sensitivity. The smaller energy window improved the detector resolution, but the 511 keV line could no longer be used as a gain monitor. To use the backscattering peak as a gain monitor, the runs were summed by series to generate a photon energy spectrum. The backscatter peak was fit to a Gaussian despite not being symmetric. The detector resolution here is wide enough that a Gaussian is a reasonable approximation in the local neighborhood to reliably determine a calibration point from series to series.

The peak position from the fit served as a calibration point which was applied to all the runs in the series.

6.1.2 Threshold effects

The spread in the photon detector calibration factors is 13 % which corresponds to a ± 1 keV spread around the 15 keV threshold. At the 15 keV threshold, the photon detector resolution has a significant effect, and given the $1/\omega$ photon decay rate at threshold, the resolution is expected to lead to a net increase in photon counts above threshold. The resolution was measured to be about 35 % for the 60 keV ^{241}Am line. Assuming that the resolution width scales as $\omega^{-1/2}$, a 20 keV width at 60 keV is 10 keV at the 15 keV threshold.

To examine the threshold effects, a 10 keV width (FWHM) Gaussian (at the 15 keV threshold) was convoluted with the theoretical photon decay spectrum. This spectrum was integrated from 14 keV to 16 keV and compared to theoretical value of the branching ratio to estimate the variation of the branching ratio. This variation is the total uncertainty due to resolution and gain drift. This convoluted spectrum was also integrated from the 15 keV threshold and compared to the theoretically expected branching ratio to calculate the systematic correction.

Because the photon rate increases as the photon energy gets smaller, detector resolution causes more events with energies below threshold to be detected than those high energy events which are lost. Detector resolution causes the measured branching ratio from the data to be overestimated from the theoretical value. A systematic correction of -2.5 % is applied to the final branching ratio as a result of detector resolution at the 15 keV threshold. The total uncertainty from resolution and gain drift is estimated to be 7 %. Figure 6.1 shows the theoretical and convoluted spectrum used to estimate the systematic correction and uncertainty.

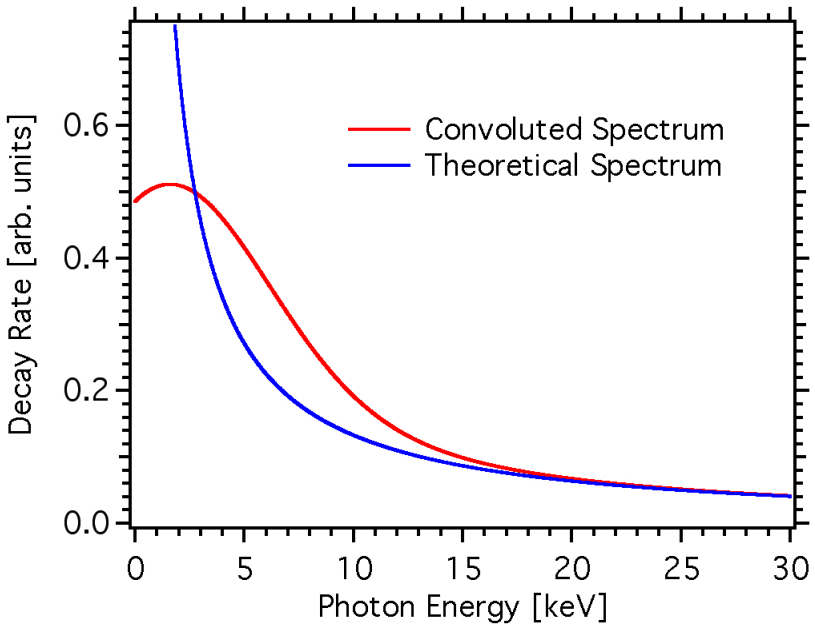

Figure 6.1: The theoretical photon energy spectrum and the blurred photon energy spectrum. The blurring is the result of a 10 keV FWHM gaussian being convoluted with theoretical energy spectrum near the 15 keV threshold. An excess of counts is observed as expected.

6.1.3 Photon detector efficiency

The MC which generates the $R_{ep\gamma}/R_{ep}$ ratio does not incorporate detector efficiency or a model of photon scattering. The measured branching ratio underestimates the correct branching ratio because the overall detector efficiency is less than unity, and it requires a positive correction to the branching ratio. Photon scattering from the magnet bore tends to increase the number of detected photons, and a negative correction is required. These competing effects must be examined together.

A second MC using MCNP5 modeled the experimental apparatus and the BGO crystal response to simulate the photon detector response to the theoretical photon energy spectrum. The measured branching ratio underestimates the theoretical estimate when both effects are combined. A systematic correction of +3 % is required, and a conservative approach was taken for uncertainty of this correction. The size of systematic uncertainty was set to the size of the systematic correction.

The MCNP5 result was corroborated with a simplified photon tracking code which utilizes photon interaction cross section data from NIST XCOM [5]. In this code, the photoelectric effect is modeled by 100 % energy deposition into the material and neglects X-ray fluorescence. The Klein-Nishina formula was used to calculate the angular dependence of Compton scattering, and all other mechanisms were neglected (the energy is too low for pair production and Rayleigh scattering was neglected).

Evaluating the correction to the branching ratio is straight-forward because it is an aggregate value over the entire, detected photon energy region. The analysis is more complicated when the photon energy spectrum is generated due to the energy dependence of the efficiency (see figure 3.8) and scattering.

6.2 Charged Particle Energy

The software analysis extracts the following parameters: photon energy, electron energy, proton energy, electron-delayed proton time difference, and electron-photon time difference. In the previous section, the photon energy and its systematic uncertainties were discussed. In this section, the systematic uncertainties connected to the energies of the charged particles are examined. The electron and proton energy cuts and analysis are intimately connected to the calibration of the SBD. After discussing the SBD calibration in section 6.2.1, the electron and proton energy systematic uncertainties are discussed in sections 6.2.2 and 6.2.3, respectively. The timing analysis cuts are deferred to section 6.3.

6.2.1 SBD calibration

The proton and electron energy calibration was periodically done *in situ* using an ^{241}Am source. One calibration serves for both particles because the SBD detects both the proton and electron. The cooled detector was mounted on a linear motion

feedthrough, and it could be retracted from the bore for calibration. The source was placed near to the SBD but outside the vacuum system. The vacuum walls were sufficiently thin that the 60 keV gamma rays would penetrate and be detected by the SBD whereas the alpha particles were absorbed. A second point was obtained using the 780 keV endpoint of the electron spectrum. The peak of the accelerated protons (accelerated to -25 keV) was not used as a calibration point because of the proton energy loss in the dead layer of the SBD. The typical energy resolution of the proton peak was 35 %, and the full-width at half-maximum was about 8 keV.

6.2.2 Electron energy threshold

The lower energy threshold on the electron spectrum was selected in hardware to be slightly above the proton peak to ensure that the electronics were not triggered by the accelerated protons. Using the calibration points, the average electron threshold for the data set was measured to be 36 keV. This value allows a margin of safety after taking into account the acceleration potential of the proton (-25 kV), the proton energy loss, and the detector resolution. Table 4.1 shows the measured electron thresholds for each series.

The MC was run with the experimentally determined electron energy threshold for each series to calculate the correction to its ratio. A weighted average of all the ratio values at each voltage was made yielding the total, voltage dependent correction to the ratio. After fitting this new MC result to the data, total systematic correction to the branching ratio was found to be less than 0.05 %. This correction is made by comparing the branching ratio from this modified procedure to the standard procedure which uses a hard 35 keV electron threshold. The total spread in the voltage dependent corrections is $\pm$ 1.5 % of the branching ratio, and this conservative estimate is used for the systematic uncertainty.

The 12 keV spread in the electron threshold values can be applied to the total number of electron events. This changes the total number of electron events by 2 % which is similar to the estimate made above. This procedure overestimates the uncertainty, though, because the ratio method tends to reduce sensitivity to systematic effects. Because the branching ratio is derived from a fit to the $R_{ep\gamma}/R_{ep}$ ratio, the previous calculation is used.

6.2.3 Proton energy spectrum

The proton endpoint energy is so small that the protons must be accelerated to be detected. This acceleration and the noise on the SBD eliminates the ability to extract proton energy information. The protons energy spectrum is a Gaussian peak centered at the acceleration potential minus the energy loss in the dead layer of the detector. The Gaussian response has a FWHM of approximately 8 keV. In the analysis, all events within 2 FWHM around the proton energy peak were accepted. This cut results in a loss of approximately 2 % of the detected protons.

To test for any systematic correction, the theoretical decay spectrum (see figure 5.4) was convoluted with a Gaussian of the same width as the experimental spectrum to simulate the detector response. The convoluted radiative and non-radiative spectra are shifted by 0.5 eV, the same as the raw spectra. The systematic shift in the $R_{ep\gamma}/R_{ep}$ ratio was found to be less than 10^{-3} and is negligible. The uncertainty was also negligible, and this exhibits the power the ratio method has in ameliorating the systematic effects.

Protons can also be lost through Rutherford backscattering from the surface of the silicon. This effect was calculated using SRIM-2006 [110] and 2 % of the protons are lost. It is still possible for backscattered protons to be detected due to the attractive potential on the SBD. Similar to the proton energy spectrum cut, the systematic

shift and correction both have a negligible effect on the extracted branching ratio.

The total correction and uncertainty for proton energy events is negligible because the raw proton energy spectrum is so similar for radiative and non-radiative events. This is not the case for the electron, where there is a significant spectrum shape change.

6.3 Timing Cuts

There are two timing cuts that are made on the data, the electron-delayed proton time difference and the electron-photon coincidence from which the number of correlated photons are extracted. Figure 4.7 shows the electron-delayed proton timing spectrum at several values of the mirror potential. The calibration for the timing spectrum came from the TAC, and it was checked against a time calibration module. The full timing window from the TAC was 20 μs, and the precision in the time calibration is known better than was needed.

The most significant contribution to the timing uncertainty arises from the determination of pulse onset time from the digitized waveforms. The onset time for the electron and proton must correctly be extracted for a correct comparison to MC. As described in the chapter IV, a slewing correction is applied to the time difference calculated from the electron and proton pulse peaks. The total uncertainty in determining the time difference is $\pm$ 200 ns.

In the MC and the data, the lower timing cut (2.5 μs) and the upper time cut (20 μs) were both varied by the timing uncertainty $\pm$ 200 ns. By calculating the branching ratio for each configuration of these cuts, there is no systematic correction, but there is a systematic of uncertainty of 2 %. The uncertainty is dominantly from the 2.5 μs timing cut, but the 20 μs does contribute slightly. The uncertainty

is reduced at higher electrostatic mirror voltage, and this can be understood by examining figure 4.7. At high electrostatic mirror voltage, the majority of events occur in the neighborhood of 5 μs, well within the timing cuts. Therefore, the cut removes a smaller fraction of the total events at high electrostatic mirror voltage.

Figure 4.9 shows a typical electron-photon time difference spectrum. The number of radiative decay photons is extracted from the uncorrelated background by summing all of the events in the correlated events peak and subtracting the uniform background. This procedure is described in section 4.3.

A window with a fixed width was applied to each series, and it encompassed nearly all of the Gaussian timing peak in the data. While the width of the peak did vary slightly from series to series, the window essentially covered the entire peak, and the variation in the peak width and data binning yields no systematic correction. It is possible, given the coarse binning and large background, that the window can be shifted. There can also be a systematic uncertainty in the extraction of the time difference, and possibly a small unaccounted non-uniformity in the background. In the fit, these factors can introduce a non-statistical uncertainty in the background subtraction. To account for these possibilities, a conservative approach yields a systematic uncertainty of 2 %.

6.4 Correlated Backgrounds

Correlated backgrounds are events with an electron-delayed proton trigger and a photon correlated to the trigger, but this photon is not from a radiative decay event. These are particularly nefarious as no simple cut can eliminate their effect.

6.4.1 External bremsstrahlung

The primary source of correlated background that can produce a coincidence peak in the electron-photon timing spectrum are decay electrons slowing down in the SBD. These produce external bremsstrahlung photons through atomic collisions, and the signature of such events is identical to that of a radiative decay event. The geometry of the apparatus dramatically reduces the probability of such photons reaching the BGO crystal. Furthermore, shielding composed of ^{6}Li-glass and 2 cm of lead partially occluded the direct line-of-sight between the two detectors. MCNP5 found that 3 % of the events attributed to radiative neutron decay could be due external bremsstrahlung. A -3 % correction is made to the branching ratio and the full value of the correction was taken as the uncertainty.

6.4.2 Electronic artifacts

There exist two sources of correlated background that occur as a result of real physical phenomena that produce electronic artifacts in the digitized waveforms. These events occur at a comparatively high rate, but are effectively eliminated by the cuts on the data because of their distinct waveform shapes. One mechanism for producing a correlated background of this type is a gamma-ray cascade that can occur when a cold neutron captures on material near the detectors and triggers the DAQ. When a high energy gamma-ray hits the SBD, it saturates the response of the detector and generates a large amplitude pulse with a long tail characteristic of the pathological event triggers. As part of the cascade, another photon may strike the BGO and be detected along with the SBD trigger. This sequence matches the same hardware conditions as for a radiative decay event and appears as a peak at the appropriate position in the timing spectrum.

The energies of the particles and pulse shape characteristics are so pathological, however, that they can be easily distinguished in software. The ability to discriminate these events was checked by acquiring data for two days with the beam on but the high voltage off. This eliminates the possibility of registering a true electron-delayed proton trigger but allows all other beam-related phenomena to trigger the electronics. In the two-day run, 63 events fell within the electron-photon timing window, but after the application of our standard set of cuts, no events survived.

A second potential source of correlated background event is associated with $-25\,\mathrm{kV}$ potential applied to the SBD. Occasional high voltage discharges can bleed off electrons into the vacuum where they can generate low energy x-rays. The waveform signatures of these events are similar to those generated in the beam-related background. The rejection efficiency of the analysis was tested by running the apparatus for almost eight days when the reactor was off. During that time, only 17 events fell with the electron-photon timing window, and one event survived the software cuts. Assuming that one event occurs every eight days, then 11 false events are expected in the cut data. Given that the data set contains nearly 4000 radiative decay events, this would contribute no more than 0.5 % to the signal. The systematic uncertainty was taken as the size of the correction.

6.5 Model Uncertainties

Examining some of the systematics in the analysis is straightforward, but understanding other systematics requires manipulation of equipment that is not possible to accomplish during experimental running. These include, but are not limited to, the registration of the detector with respect to the electromagnetic fields. In benchmarking tests, the MC accurately describes the observed behavior and can used to

estimate the effect of these systematic uncertainties (e.g. figures 4.7, 4.10, 4.11, and 4.12). The MC has been used previously to corroborate the estimates of the systematic uncertainties also examined with the data. Here, the MC is the only viable way to calculate these systematic uncertainties.

6.5.1 Registration uncertainties

The uncertainty of the photon detector placement with respect of the electromagnetic fields can be analyzed by shifting the electrostatic mirror field and the magnetic field in the MC and calculating the change in the extracted branching ratio. The uncertainty of the photon detector placement with respect the field coils and the electrostatic mirror is ± 1 mm. By shifting these fields in MC, the maximum deviation in the ratio is 1 % from shifting the electrostatic mirror and 2 % from shifting the magnetic field. The uncertainty of the absolute field strengths due to current or voltage uncertainties is negligible.

Placement and distribution of the neutron beam is also best analyzed in MC. An image of the neutron beam was made downstream of the main decay region. This beam image is shown in figure 3.3, and it is linearly scaled from the upstream defining aperture. The ratio versus mirror voltage was calculated with various modifications of the neutron beam. At the extremes of these modifications, the beam profile was tested with no beam divergence, and a uniform beam profile was tested with a diverging and a non-diverging beam. Also, beam alignment was tested with a tolerance of ± 1 mm around the center of the photon detector. The total systematic uncertainty due to the beam profile, divergence, and alignment was found to be 3 %.

6.5.2 APD bias leakage

The 3-dimensional, Cartesian electrostatics solver can be applied to the APD to calculate the leakage of the 1400 V bias which can affect charged particles. The maximum voltage seen by at the center of the beam is approximately 12 V. This bias leak has the largest effect when the electrostatic mirror is unbiased and is negligible when compared to higher electrostatic mirror voltages. The extracted branching ratio does not change appreciably despite a relatively large change at 0 V.

The geometry and high voltage composition of the APD are less well-known than the electrostatic mirror, but its total contribution is smaller than the electrostatic mirror. This leads to a systematic uncertainty of no more than 1 % (and no systematic correction). WIthout the APD bias leakage, the $R_{ep\gamma}/R_{ep}$ ratio value at 0 V is smaller. Because ratio is mostly unchanged at higher voltage, the branching ratio doesn't change, but the χ^2 of the fit gets larger. Without the APD bias leakage, the χ^2 per degree of freedom is 2.5 versus 1.5 with the APD.

6.5.3 Electron backscattering

The electron backscattering fraction from the SBD is dependent upon the incident electron's energy and is very sensitive its incident angle with respect to normal θ_{inc} onto the SBD. The backscatter fraction as a function of angle and incident energy was calculated in MCNP5 and Penelope [111]. The total backscatter fraction for electrons that are normally incident upon the SBD is shown in figure 6.2. For a given electron kinetic energy, the backscatter fractions increases rapidly with incident angle. This behavior is shown for a 100 keV electron in figure 6.3. The backscatter process modifies the energy that is deposited into the SBD by the electron, and these MC packages calculate this detector response.

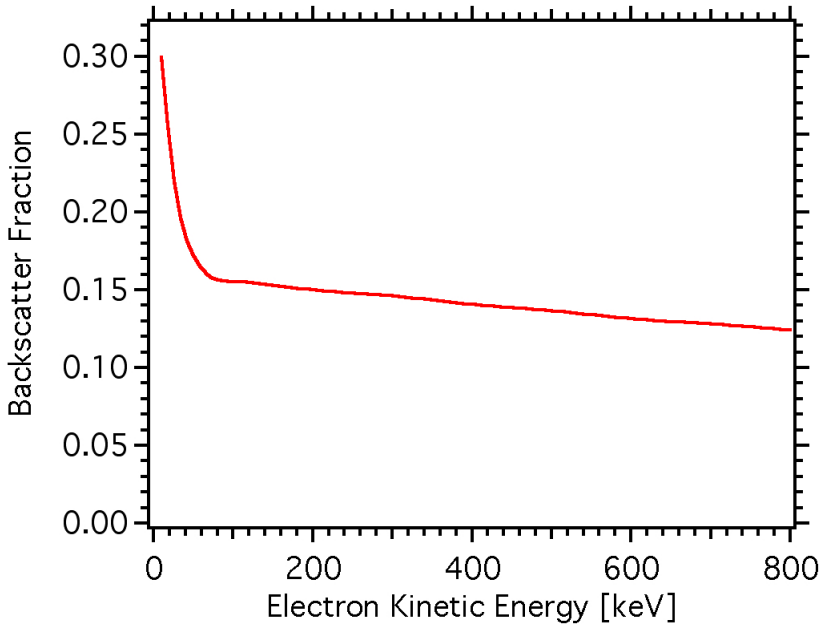

Figure 6.2: The total backscatter fraction for normally incident electrons onto the SBD as a function electron kinetic energy.

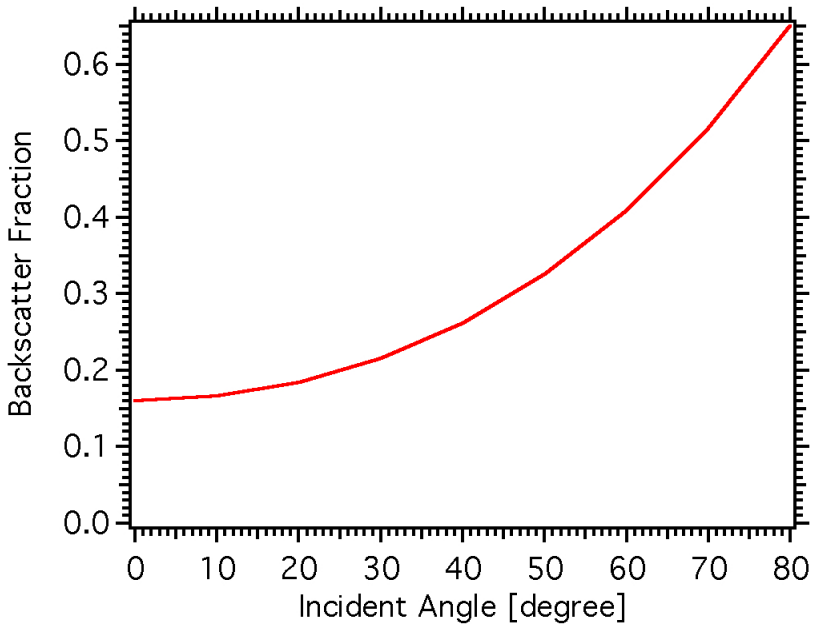

Figure 6.3: The total backscatter fraction for 100 keV electrons onto the SBD as a function incident angle. For energies above the electron threshold, the angular dependence of backscattering is the largest effect.

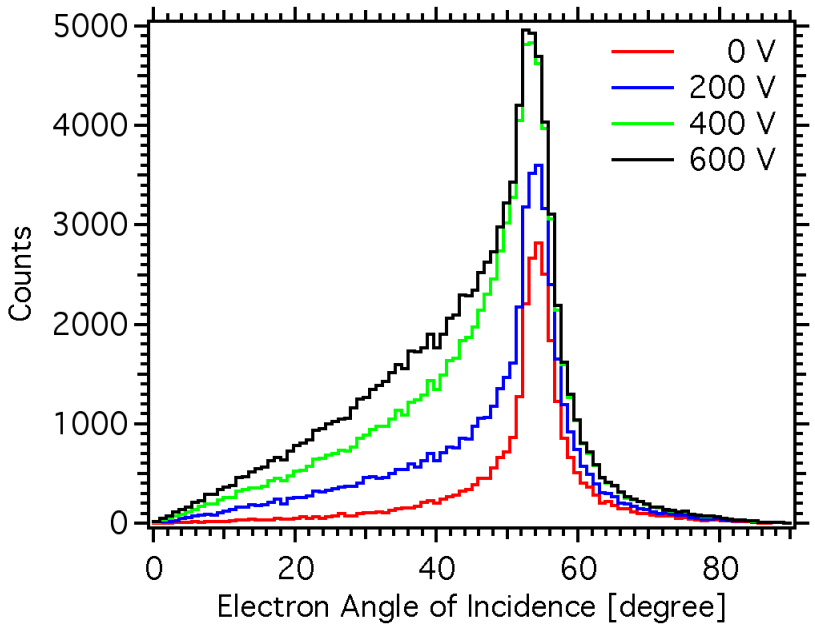

Figure 6.4: The incident angle that the electron strikes the SBD as a function electrostatic mirror voltage for non-radiative decays. Radiative decay show similar behavior.

Each computational package yields roughly the same result for the backscatter fraction. A comparison of electron backscatter data to GEANT4 [112, 113] and Penelope MC packages is described in Martin et al. [114]. Martin et al. describe normal backscattering from a silicon detector for electron kinetic energies up to 124 keV. The results from MCNP5 and Penelope are in reasonable agreement with each other and with the Martin et al. data.

Electron backscattering causes raw electron spectrum to shift towards lower energy because of partial energy deposition. By using the MC data, the change in the $R_{ep\gamma}/R_{ep}$ ratio is found to be mirror voltage dependent. This is expected because the average electron energy and angle of incidence are dependent upon electrostatic mirror voltage. The electron incidence angle can be calculated in MC for non-radiative decay, and this is shown as a function of electrostatic mirror voltage in figure 6.4. The radiative decays show similar behavior.

The inclusion of electron backscattering requires a 0.2 % systematic correction to

the branching ratio. The variation of the correction at each mirror voltage varies by $\pm$ 0.5 %, and this value was taken as the systematic uncertainty. To account for any discrepancies in the backscatter fraction from MCNP5, GEANT4, or Penelope, a phenomenological model was also used to parameterize electron backscatter. This model is derived from electron backscattering studies on plastic scintillators [103, 104] and modified to match the results of Martin et al. The model allows a wide variety of parameters to be used, and the backscatter results are consistent with those from the software packages.

CHAPTER VII

Conclusion

The results of the first radiative beta decay experiment a future experiment are summarized in this chapter. Section 7.1 reports the branching ratio and discusses the question of the photon energy spectrum. The significance of this first measurement of the radiative decay mode is reiterated. Section 7.2 discusses the planned second run of the radiative decay experiment. For the second run, apparatus upgrades and a more detailed calibration procedure anticipate lowering both the statistical and systematic uncertainty to below the 1 % level.

7.1 Results of First Experimental Run

The branching ratio is extracted from a fit of the MC to the $R_{ep\gamma}/R_{ep}$ ratio data, and it is shown in figure 4.12. The branching ratio from the fit is 3.18×10^{-3}, and the uncertainty ascribed to the fit is 3.4%. The uncertainty of the fit arises from the statistical uncertainty from the ratio data points (background subtraction enlarges this uncertainty beyond simple Poisson counting statistics). After applying the systematic corrections and uncertainties, the branching ratio is $(3.09 \pm 0.32) \times 10^{-3}$.

The experimental result is consistent with the theoretical prediction of 2.85×10^{-3} [115]. With a total uncertainty of approximately 10 %, this result is not precise

enough to constrain any new physics. This result does test the lowest order QED prediction of electron bremsstrahlung though. This experiment performed a 10 % precise measurement of an effect that is approximately 0.3 % of the neutron decay rate. The total contribution to the neutron lifetime, though, is reduced by cancellations with the photon exchange process, but it is an important first measurement of a radiative correction. The systematic effects have highlighted that radiative decay can affect some neutron decay experiments at the $\mathcal{O}(0.5)$ %, especially those experiments that are sensitive to the electron-proton opening angle and electron energy.

7.1.1 Importance to nuclear physics

The radiative decay mode of the neutron is a fundamental decay branch of an important subatomic particle. Because the neutron lifetime holds such an important place in the structure of the SM, every contributing piece of the lifetime should be understood. This is the first definitive measurement of the branching ratio for this rare decay branch. Improved future measurements of the radiative decay mode will be more sensitive probes of new physics, and they must overcome the same systematic uncertainties as this experiment.

Because many neutron experiments utilize polarized neutrons, this work extends the pioneering theoretical calculations of Gaponov et al. [57, 58, 59] and Bernard et al. [60, 61] by considering the radiative decay of a polarized neutron. The effect of time-reversal is also incorporated which yields new angular correlations. While Bernard et al. calculated the emitted photon polarization numerically, this dissertation reports the lowest order, analytic form for a polarized photon in Appendix A. These calculations contain well-known QED interactions, and it is possible to extend them to new interactions such as right-handed currents, non-V/A interactions, etc. Few neutron experiments have considered what effect high energy photons have on

their results, but these new theoretical results can be used to calculate it.

To overcome a low decay rate in a background polluted environment, a unique detection scheme was required. The electron, delayed proton, and photon were all detected in coincidence to reduce the large background rate. The photon detection scheme was required to operate in an extreme environment and has a novel design. This experiment uses rugged, solid state photodiodes over PMTs, and this trend is on the rise in many nuclear experiments with large magnetic fields. The use of crystal scintillators is not new, but the realistic choices available are limited due to the experimental apparatus' cryogenic environment. An added complication is the relative low energy of the neutron decay photons. Most nuclear systems liberate more energy so these nuclear decay photons are easier to detect.

Because the SBD was a hybrid electron / proton detector, the triggering system is more susceptible to pathological events. Correlating the electron and photon in time is an extremely high priority for background suppression. The DAQ in this experiment is one of the first in neutron decay experiments to record the entire oscilloscope waveforms for all events in lieu of standard nuclear counting techniques. This allows the analysis to perform a crude pulse-shape discrimination (baseline cut) to eliminate pathological events. The fitting procedure for the electron and photon, described in chapter IV, utilizes waveform data to improve timing in lieu of a traditional constant fraction discriminator.

7.1.2 Photon energy spectrum

In figure 4.13 the experimental photon energy spectrum is shown and overlaid is the decay spectrum from MC with a model of the detector response which was incorporated in the branching ratio as a systematic uncertainty. This can be done for the photon energy spectrum as well, but a more exact treatment of the photon

detector response is desired. This work is ongoing, and MCNP5 and GEANT4 are is the MC tools being utilized. The method of analysis in progress takes the theoretical decay spectrum and simulates its response in the detector, yielding the modified decay spectrum.

The desired analysis procedure would be to record the photon energy spectrum from the experiment and remove the detector response through de-convolution, leaving the raw decay spectrum. One potential solution is to simulate the detector response of the experiment for monochromatic sources. By picking sources across the entire energy region, the full response can be measured. This is an ambitious program that is underway with the support of MC simulations.

7.2 Future Work

A second run of the radiative decay experiment is underway. This second run will measure the branching ratio to a 1 % uncertainty and precisely measure the photon energy spectrum. Section 7.2.1 describes the motivation for improving the experimental uncertainty from 10% to 1%. Apparatus upgrades are necessary to improve the systematic and statistical uncertainties. The centerpiece of the upgrade is a new, 12-element detector with a similar design as the original detector, and it is discussed in section 7.2.2. The bare APD can be used to detect radiation, and a bare APD detector array is being constructed, and it is described in section 7.2.3. Section 7.2.4 describes the use of a calibrated fission chamber to measure the $1/v$-weighted neutron flux which allows the measurement of absolute decay rates. Section 7.2.5 describes the preferred method for assessing the systematic uncertainties, and it emphasizes the importance of photon detector calibrations to eliminate the largest uncertainty of the first measurement.

7.2.1 Motivation for a second run

A new measurement of the radiative decay mode of the free neutron continues to improve knowledge of a fundamental semileptonic decay process. Low's theorem describes how a low energy radiative decay experiment can shed light on the non-radiative decay mode. Conversely, a high energy photon measurement can search for new physics directly correlated to the photon's presence. The new photon detector will measure the radiative decay for all photons above 15 keV to the photon endpoint energy (782 keV). The extension from 340 keV to the endpoint relies upon a dramatic reduction of backgrounds and improved timing resolution. An additional photon detector is being constructed from bare APDs to probe a lower photon energy regime for photon energies from approximately 200 eV to 10 keV. With the two detectors, the radiative decay mode can be measured over nearly 4 orders of magnitude in photon energy. The combination of the two arrays of detectors allows the measurement of photon angular correlations.

The experiment represents an important exploration for future precision radiative decay experiments below 1 % uncertainty. By including all inner bremsstrahlung contributions and recoil order terms, the decay total radiative rate differs from the leading electron bremsstrahlung result at $\mathcal{O}(0.5\ \%)$ [60]. Therefore, non-leading order radiative decay contributions are within reach of a next generation experiment. The development of these new experiments must solve the same problems that this experiment is addressing.

The experiment could also be performed with polarized neutrons, allowing new angular correlations to be measured. The photon momentum can be correlated with the polarized neutron's spin, and time-reversal violating correlations can only be measured with polarized neutrons. A next generation experiment that measures the

photon polarization is a test of the $V - A$ structure of the weak current [60]. In all of these tests, the extracted parameters are due to 4-body final states (radiative decays) versus the 3-body final state in the usual non-radiative beta decay.

7.2.2 12-element detector

A new photon detector with 12 BGO-APD detectors in a coaxial configuration is being developed for use in the second run. The 12 detectors are mounted into a single assembly that can be located accurately in the magnet bore. Tests are underway to paint the crystals with a Bicron reflective tape to increase light yield. The 12 APDs are mounted on a G10-FR4 fiberglass mount and pressed against the open ends of the BGO with a nylon, spring-loaded mount. The entire system is assembled on stainless steel struts and aluminum rings hold the BGOs in a precise position. Nylon cylinders at the upstream and downstream ends of the detector, each with 3 brass retractable "feet," hold the entire assembly in the magnet bore. A photograph of the detector under construction is shown in figure 7.1.

Mounted at the downstream end of the photon detector assembly is a pair of embedded aluminum tubes that serve as an electrostatic mirror. The outer tube is grounded and shields the neutron beam from any stray electrostatic fields from the APDs or supply wires. The inner tube is biased with a variable electrostatic potential, and it is a 4.75 in. long, 2.00 in. outer diameter, and 0.065 in. thick tube. The outer ground tube is 5 in. long, 2.50 in. outer diameter, and 0.125 in. thick. The 0.125 in. gap remaining between the tubes is filled with a two-piece, interlocking, teflon insulating tube. The mirror registration systematic is reduced to less than 0.5 mm because it is mounted directly to the photon detector. MC was used to determine the optimal position of the detector / mirror assembly in magnetic bore. The assembly is placed so that the APD is 10.00 cm from the end of the magnet bore.

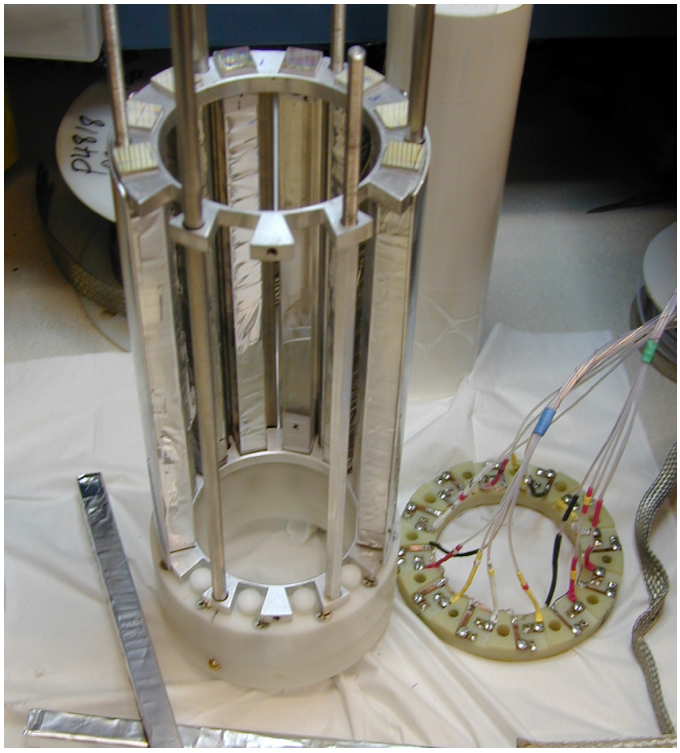

Figure 7.1: A photograph of the 12-element detector with the electrostatic mirror removed.

Figure 7.2 shows a mechanical drawing of the photon detector / mirror assembly.

Mounted upstream of the photon detector is a lead-copper shield to reduce the total uncorrelated background events from the reactor. The 1.00 in. thick tube of lead with an inner diameter of 2.00 in. and outer diameter of 4.00 in. is surrounded by 0.00625 in. layer of copper. The lead block provides bulk attenuation of the uncorrelated photons coming from the reactor. Unfortunately, high energy photons excite the lead atoms to fluoresce a 90 keV X-ray. The thin layer of copper effectively attenuates the lead X-ray, but must be thin to reduce the Compton scattering of photons back towards the BGO crystals. This design was optimized with MCNP5.

The new photon detector will reduce the statistical uncertainty below the 1 % level. First, the increased solid angle for detection gives 12 times the total photon events detected. The addition of the lead-copper shield reduces the uncorrelated

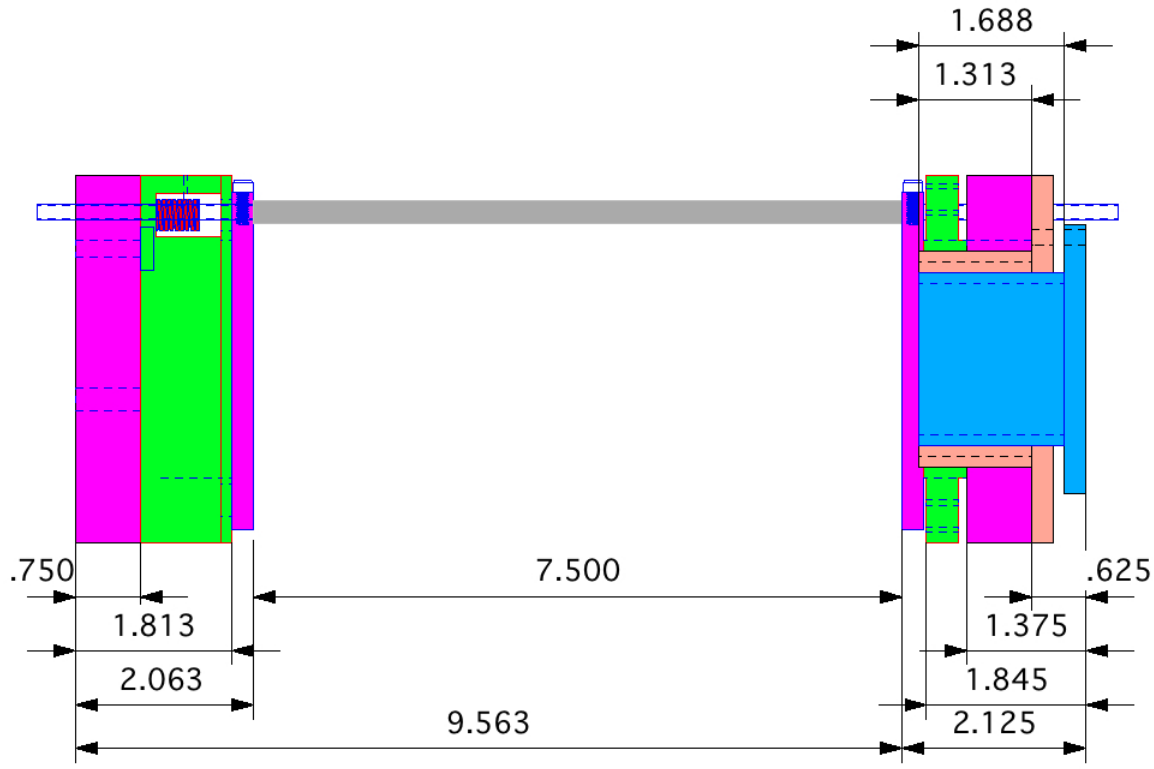

Figure 7.2: Schematic of the 12-element photon detector. The magenta elements at the ends are the nylon placement cylinders with brass "feet." The green element on the left is the nylon, spring-loaded crystal pusher. The green element to the right is the G10-FR4 fiberglass APD mount. The gray bar is the BGO crystal which is held by the thin magenta elements. The thin magenta elements are aluminum, notched rings that hold crystals with friction. The entire crystal assembly is surrounded by an aluminum heat shielding tube. The embedded tube electrostatic mirror is on the right with the orange and blue elements.

photon background that is subtracted from the correlated photon peak, improving the statistical uncertainty. During the first run, an 8-bit, bipolar oscilloscope card was used to digitize all the waveform data collected. A 14-bit, bipolar GaGe Octopus oscilloscope card has currently replaced the original card, and the higher voltage resolution significantly reduces the digitization noise on the photon signal. This improves the width of the electron-photon time difference spectrum, further reducing the uncertainty from background subtraction.

7.2.3 APD direct detection

Large area APDs can be used to directly detect radiation below the threshold of the scintillator-APD detector. Because the bremsstrahlung diverges as $1/\omega$, where ω is the photon energy, the APD can detect a higher photon rate per unit area and per unit energy. At the end of the first run, a series was run with a bare APD. Because the photon response of an APD is much faster than cold BGO, the electron-photon time difference spectrum, corresponding to figure 4.9, was much narrower. The background was practically zero, and the signal-to-background was measured to be 15 compared to 1/2 for the original BGO / APD detector.

In external cryostat tests, a photon detection threshold of 200 eV was observed for direct detection by the APDs. Photons above 5 keV are detected with reduced efficiency because they do not deposit all of their energy in the device. X-ray fluorescence tests with the 5.9 keV X-rays from ^{55}Fe source used to test the lower energy response of the APD [116]. The $CaSO_4$ was placed in the vacuum of the cryostat and irradiated by the ^{55}Fe source through a thin plastic window. Figure 7.3 shows the response of the APD for the iron (5.90 keV), calcium (3.69 keV), sulfur (2.31 keV), and aluminum (1.49 keV) X-rays. The disadvantage of direct detection is much lower solid angle for detection.

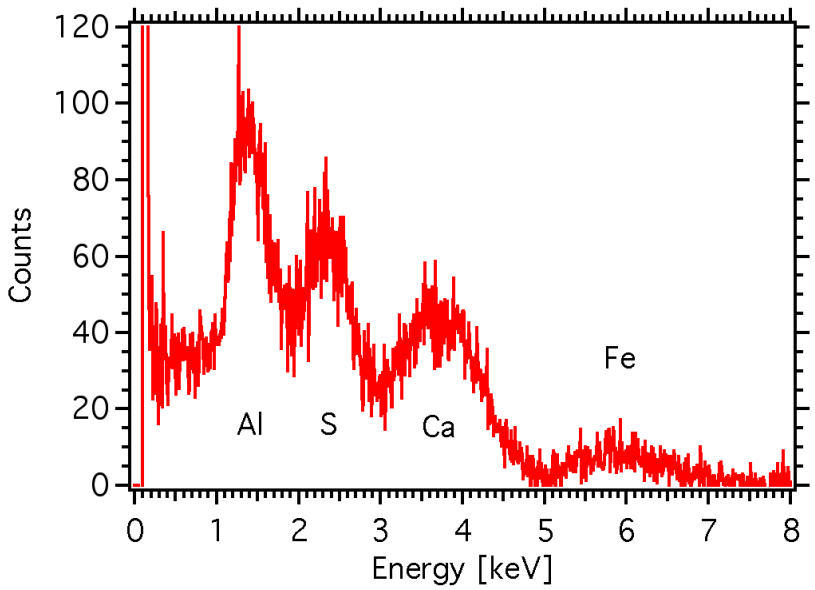

Figure 7.3: X-ray fluorescence spectrum from $CaSO_4$ irradiated by a 5.9 keV iron X-ray. The iron (5.90 keV), calcium (3.69 keV), sulfur (2.31 keV), and aluminum (1.49 keV) X-rays pass through a thin, plastic window before striking the APD.

An array of 4 large area APDs in an coaxial configuration is being assembled . While the APDs that couple the BGO signal are 13.5 mm x 13.5 mm active area, the APDs for the direct detection assembly are 28 mm x 28 mm active area. The direct detection assembly will be located between the lead-copper shield and the 12-element detector. By running both detector arrays simultaneously, some information can be gleaned about photon angular correlations.

7.2.4 Absolute decay rate measurements

The branching ratio in the first run was extracted from the ratio of the electron-delayed proton-photon events to the electron-delayed proton (no observed photon) events as a function of voltage. This procedure was necessary because there was no way to calibrate the observed electron-delayed proton and electron-delayed proton-photon rates absolutely. A calibrated, Li-foil, neutron flux detector will be mounted downstream of the experimental apparatus for the second run. This neutron flux

detector measures the $1/v$-weighted neutron flux where v is the neutron velocity. Because the beam is polychromatic, the $1/v$-weighting accounts for, in a nearly perfect way, the probability that a neutron decays in the apparatus.

The vast majority of detected events are electron-delayed proton events with no correlated photon (over 10^7 events in the first run) because the radiative decay rate is very small. With absolute decay rate knowledge, the MC can be tested absolutely by measuring the parameter a. The measurement procedure follows from the same discussion presented at the end of section 2.4.1. The electrostatic mirror is effectively a proton spectrometer that is sensitive to the longitudinal momentum component (and not the total energy), and a is measured with low precision.

7.2.5 Run 2 systematics

Off-line cryostat testing is underway to characterize the photon detector response to external gamma-ray sources. These tests have been performed at both room and cryogenic operating temperatures. At cryogenic temperatures, tests were also performed with and without the 4.6 T magnetic field. The stability of the noise and gain of the detector over long periods of operation, including over cryogen fill cycles, was tested and found to be very stable.

During the first run, no photon singles measurements were made resulting in poor statistical sensitivity to the calibration features. The observed photon detection rate in the first experiment is consistent with a 100 s^{-1} photon singles rate. The lead-copper shield will reduce the photon singles rate from background photons, but the photon singles rate will be large enough to resolve the calibration features in a very short amount of time. Previously, the photon backscatter peak (approximately 160 keV) and the pair production photon peak (511 keV) were used as gain monitors. Because the new photon detector is segmented, a bismuth X-ray from one BGO

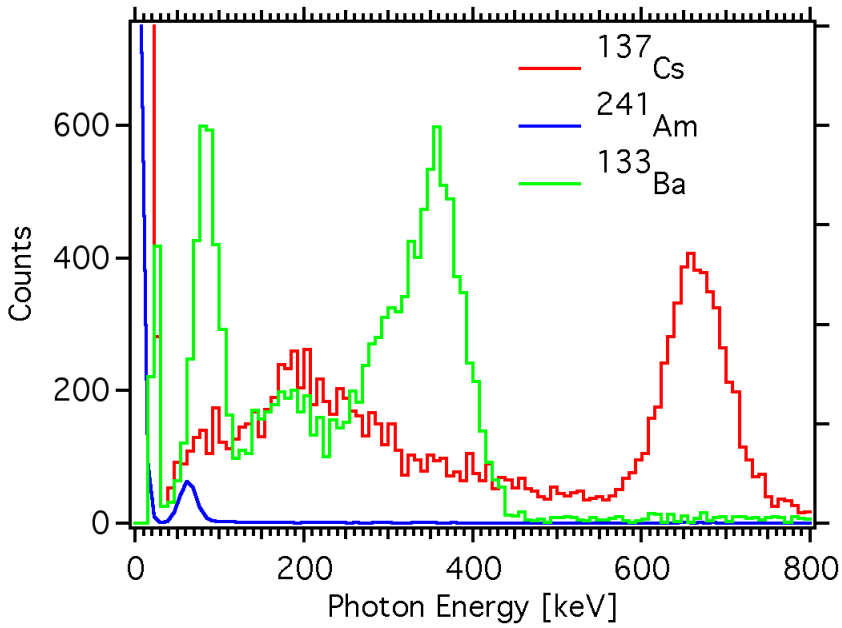

Figure 7.4: Calibration source spectra for ^{137}Cs (662 keV) and ^{133}Ba with ^{241}Am (60 keV) overlaid for comparison. The main ^{133}Ba gamma rays are at 80 keV, 303 keV, and 356 keV. This plot shows that the detector has a linear response.

element can be detected and used as another gain monitor.

Calibration runs with gamma ray sources at cryogenic temperatures are shown in figure 7.4. These tests show the 661 keV peak from a ^{137}Cs source and a 60 keV peak spectrum from ^{241}Am is overlaid for comparison to Cs. These spectra confirm the linearity of the detector over the effective energy range for the detector. In this particular calibration test, the bismuth X-ray is emerging at approximately 80 keV in the ^{137}Cs spectrum.

The efficiency of the photon detector must be known to an uncertainty better than 1 %. To improve the uncertainty by almost an order of magnitude, both simulation and experiment are needed to understand the efficiency. The spatial dependence of the scintillation light yield in BGO was smaller than the uncertainty in the first run of the experiment, but it requires a more precise determination for the second run. A standardized gamma ray source must be calibrated for the test geometry, and this

can be done with a standard Ge detector arrangement. By using a lead collimation tube, the gamma rays can be implanted in a specific location on the BGO crystal, and the spatial dependence can be mapped. This procedure can be combined with MC to understand the detector response to less than 1 % uncertainty.

To reduce the total uncertainty, all of the systematic uncertainties in table 6.1 must be reduced by an order of magnitude. The procedure outlined in chapter VI averaged each systematic effect over all electrostatic mirror voltages. A better estimate is to treat each voltage as a separate radiative decay experiment and separate the systematics. More experimental testing and MC are needed.

7.2.6 Status

At the time of writing, the experimental apparatus for run 2 has been installed on the NIST NG-6 beamline. It is currently undergoing commissioning runs to optimize the setup. The experiment is expected to run for one year on the beamline to achieve the precision needed.

APPENDICES

APPENDIX A

Polarized Photon Decay Rate

In Chapter II, the photon polarization versus photon energy was calculated. Below is the lowest order decay rates for each photon polarization state $d\Gamma_{\pm}/dX$ where X are the 8 kinematic variables. The left-handed photon state $d\Gamma_{-}/dX$ is

$$\frac{d\Gamma_{-}}{dE_e d\omega d\Omega_e d\Omega_{\bar{\nu}} d\Omega_{\gamma}} = -\alpha \frac{g_V^2 |\mathbf{p_e}| E_{\bar{\nu}} \omega}{2(2\pi)^7} (1 + 3|\lambda|^2) \times \left[\frac{1}{\omega^2} + \frac{m_e^2}{(p_e \cdot k)^2} - \frac{2E_e}{(p_e \cdot k)\omega} \right] (E_e E_{\bar{\nu}} + a(\mathbf{p_e} \cdot \mathbf{p}_{\bar{\nu}})) .$$

The right handed polarization state $d\Gamma_{+}/dX$ is

$$\frac{d\Gamma_{+}}{dE_e d\omega d\Omega_e d\Omega_{\bar{\nu}} d\Omega_{\gamma}} = -\alpha \frac{g_V^2 |\mathbf{p_e}| E_{\bar{\nu}} \omega}{2(2\pi)^7} (1 + 3|\lambda|^2) \times \left[E_{\bar{\nu}} \left(\frac{2}{\omega} + \frac{E_e}{\omega^2} + \frac{m_e^2 (E_e + 2\omega)}{(p_e \cdot k)^2} - 2\frac{(2E_e + \omega)}{(p_e \cdot k)} - 2\frac{E_e^2}{(p_e \cdot k)\omega} \right) + a\mathbf{p}_{\bar{\nu}} \cdot \left(\frac{\mathbf{p_e}}{\omega^2} + m_e^2 \frac{(\mathbf{p_e} + 2\mathbf{k})}{(p_e \cdot k)^2} - 2\frac{(\mathbf{p_e} + \mathbf{k})}{(p_e \cdot k)} - 2E_e \frac{(\mathbf{p_e} + \mathbf{k})}{(p_e \cdot k)\omega} \right) \right] .$$

It is easy to check that when these results are added, the unpolarized rate calculated in equation 2.29 is returned. It is written below for reference,

$$\frac{d\Gamma}{dE_e d\omega d\Omega_e d\Omega_{\bar{\nu}} d\Omega_{\gamma}} = -\alpha \frac{g_V^2 |\mathbf{p_e}| E_{\bar{\nu}} \omega}{(2\pi)^7} (1 + 3|\lambda|^2) \times \left[E_{\bar{\nu}} \left(\frac{1}{\omega} + \frac{E_e}{\omega^2} + \frac{m_e^2 (E_e + \omega)}{(p_e \cdot k)^2} - \frac{(2E_e + \omega)}{(p_e \cdot k)} - 2\frac{E_e^2}{(p_e \cdot k)\omega} \right) + a\mathbf{p}_{\bar{\nu}} \cdot \left(\frac{\mathbf{p_e}}{\omega^2} + m_e^2 \frac{(\mathbf{p_e} + \mathbf{k})}{(p_e \cdot k)^2} - \frac{(\mathbf{p_e} + \mathbf{k})}{(p_e \cdot k)} - E_e \frac{(2\mathbf{p_e} + \mathbf{k})}{(p_e \cdot k)\omega} \right) \right] .$$

APPENDIX B

Oxford Magnet Coil Configuration

In this appendix, the coil configuration for the superconducting magnet are given in table B.1. These were the specifications used by Oxford to assemble the magnet. The current in the magnet during operation was 101.95 A. An illustration of the assembled coils is given in figure B.1.

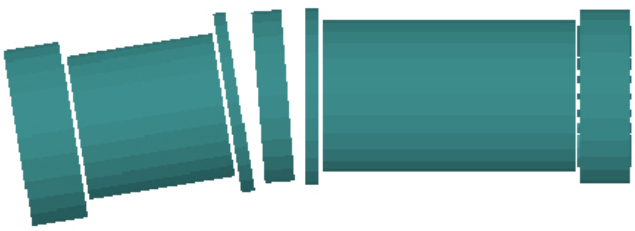

Figure B.1: Schematic of the coil configuration.

Coil	x [m]	z [m]	Bend Angle [degree]	Inner Diameter [m]	Outer Diameter [m]	Coil Length [m]	Windings
1	0.00	0.03	0	0.07	0.0828	0.3	1422
2	0.00	0.03	0	0.0832	0.1 0285	0.3	1949
3	0.00	0.215	0	0.07	0.0 7885	0.3	4787
4	0.00	0.215	0	0.0791	0.0896	0.3	5252
5	0.00	0.3775	0	0.07	0.0757	0.15	152
6	0.00	0.3775	0	0.07605	0.09277	0.15	396
7	0.00	0.3775	0	0.09317	0.1046	0.15	303
8	0.00	0.4235	4.7	0.07	0.1015	0.035	2008
9	-0.0072	0.03	9.5	0.07	0.10756	0.015	987
10	-0.0237	0.03	9.5	0.07	0.0858	0.175	5125
11	-0.0445	0.03	9.5	0.08	0.1052	0.0675	3204

Table B.1: Coil configuration data, and the x and z coordinates are for the center of the coil.

BIBLIOGRAPHY

BIBLIOGRAPHY

[1] J.C. Hardy. Superallowed nuclear beta decay: recent results and their impact on V_{ud}, 2007. http://www.int.washington.edu/talks/WorkShops/int_07_1/ People/Hardy_J/Hardy.pdf.

[2] C.E.H. Mattoni. *Magnetic Trapping of Ultracold Neutrons Produced Using a Monochromatic Cold Neutron Beam.* 2002. Ph.D. Thesis.

[3] Hamamatsu Photonics, http://www.hamamatsu.com/.

[4] L. Yang et al. *Nucl. Instrum. Meth. A*, 508:388, 2003.

[5] M.J. Berger et al. National Institute of Standards and Technology XCOM: Photon Cross Sections Database, http://physics.nist.gov/PhysRefData/Xcom/Text/XCOM.html.

[6] C. Amsler et al. (Particle Data Group). *Phys. Lett. B*, 667:1, 2008.

[7] A. Serebrov et al. *Phys. Lett. B*, 605:72, 2005.

[8] J. Chadwick. *Nature*, 129:312, 1932.

[9] A.H. Snell and L.C. Miller. *Phys. Rev.*, 74:1217A, 1948.

[10] A.H. Snell, F. Pleasonton, and R.V. McCord. *Phys. Rev.*, 78:310, 1950.

[11] J.M. Robson. *Phys. Rev.*, 78:311, 1950.

[12] J.M. Robson. *Phys. Rev.*, 83:349, 1951.

[13] C.S. Wu, E. Ambler, R.W. Hayward, D.D. Hoppes, and R.P. Hudson. *Phys. Rev.*, 105:1413, 1957.

[14] R.L. Garwin, L.M. Lederman, and M. Weinrich. *Phys. Rev.*, 105:1415, 1957.

[15] L. Goldhaber, L. Grodzins, and A.W. Sunyar. *Phys. Rev.*, 109:1015, 1958.

[16] L. Goldhaber and S.B. Treimann. *Phys. Rev.*, 110:1478, 1958.

[17] J. D. Jackson, S. B. Treiman, and H. W. Wyld Jr. *Phys. Rev.*, 106:517, 1957.

[18] J. D. Jackson, S. B. Treiman, and H. W. Wyld Jr. *Nucl. Phys.*, 4:206, 1957.

[19] T.D. Lee and C.N. Yang. *Phys. Rev.*, 104:254, 1956.

[20] J.S. Allen et al. *Phys. Rev.*, 116:134, 1959.

[21] C. H. Johnson, F. Pleasonton, and T. A. Carlson. *Nucl. Phys.*, 41:167, 1963.

[22] P. Herczeg. *Prog. Part. Nucl. Phys.*, 46:413, 2001.

[23] N. Severijns, M. Beck, and O. Naviliat-Cuncic. *Rev. Mod. Phys.*, 78:991, 2006.

[24] J.S. Nico and W.M. Snow. *Ann. Rev. Nucl. Part. Sci.*, 55:27, 2005.

[25] J. Byrne et al. *Europhys. Lett.*, 33:187, 1996.

[26] S. Arzumanov et al. *Phys. Lett. B*, 483:15, 2000.

[27] J. S. Nico et al. *Phys. Rev. C*, 71:055502, 2005.

[28] J.C. Hardy and I.S. Towner. *Phys. Rev. Lett.*, 94:092502, 2005.

[29] J.C. Hardy and I.S. Towner. *Phys. Rev. C*, 71:055501, 2005.

[30] I.S. Towner and J.C. Hardy. *Phys. Rev. C*, 77:025501, 2008.

[31] D. Počanić et al. *Phys. Rev. Lett.*, 93:181803, 2004.

[32] G.H. Aston. *Proc. Camb. Philos. Soc.*, 23:935, 1927.

[33] C.S. Wang Chang and D.L. Falkoff. *Phys. Rev.*, 76:365, 1949.

[34] J.K. Knipp and G.E. Uhlenbeck. *Physica*, 3:425, 1936.

[35] F. Bloch. *Phys. Rev.*, 50:272, 1936.

[36] R.J. Glauber and P.C. Martin. *Phys. Rev.*, 104:158, 1956.

[37] A. Yousef, M. Abdelrahman, and N. Hasan. *Jpn. J. Appl. Phys.*, 36:3688, 1997.

[38] A. Yousef, M. Abdelrahman, and N. Hasan. *Jpn. J. Appl. Phys.*, 36:5282, 1997.

[39] M. Beck et al. *JETP Lett.*, 76:332, 2002.

[40] R.U. Khafizov et al. *JETP Lett.*, 83:5, 2006.

[41] P. Langacker. *Phys. Rev. D*, 14:2340, 1976.

[42] P. Langacker. *Phys. Rev. D*, 15:2386, 1977.

[43] M.E. Peskin and D.V. Schroeder. *An Introduction to Quantum Field Theory.* Perseus Books, Cambridge, MA, 1995.

[44] D. R. Yennie, S. C. Frautschi, and H. Surra. *Ann. Phys.*, 13:279, 1961.

[45] J. M. Jauch and F. Rohrich. *The Theory of Photons and Electrons.* Addison-Wesley, Cambridge, MA, 1955.

[46] T. Kinoshita. *J. Math. Phys.*, 3:650, 1962.

[47] T. D Lee and M. Nauenberg. *Phys. Rev.*, 133:B1549, 1964.

[48] F. E. Low. *Phys. Rev.*, 110:974, 1958.

[49] S. L. Adler and Y. Dothan. *Phys. Rev.*, 151:1267, 1966.

[50] A. Sirlin. *Phys. Rev.*, 164:1767, 1967.

[51] A. Sirlin. *Rev. Mod. Phys.*, 50:573, 1978.

[52] W. J. Marciano and A. Sirlin. *Phys. Rev. Lett.*, 96:032002, 2006.

[53] A. Czarnecki, W. J. Marciano, and A. Sirlin. *Phys. Rev. D*, 70:093006, 2004.

[54] J. Byrne et al. *J. Res. Natl. Inst. Stand. Technol.*, 110:415, 2005.

[55] J.D. Jackson. *Classical Electrodynamics, 3rd Ed.* Wiley, New York, 1998.

[56] S. DeBenedetti. *Nuclear Interactions.* Wiley, New York, 1964.

[57] Y. V. Gaponov and R. U. Khafizov. *Physics of Atomic Nuclei*, 59:1213, 1996.

[58] Y. V. Gaponov and R. U. Khafizov. *Phys. Lett. B*, 379:7, 1996.

[59] Y. V. Gaponov and R. U. Khafizov. *Nucl. Instrum. Meth. A*, 440:557, 2000.

[60] V. Bernard, S. Gardner, U-G. Meißner, and C. Zhang. *Phys. Lett. B*, 593:105, 2004.

[61] V. Bernard, S. Gardner, U-G. Meißner, and C. Zhang. *Phys. Lett. B*, 599:348, 2004.

[62] J. Byrne et al. *J. Phys. G: Nucl. Part. Phys.*, 28:1325, 2002.

[63] F. Glück et al. *Eur. Phys. J. A*, 23:135, 2005.

[64] J. S. Nico, M. Arif, M. S. Dewey, T. R. Gentile, D. M. Gilliam, P. R. Huffman, D. L. Jacobson, and A. K. Thompson. *J. Res. Natl. Inst. Stand. Technol.*, 110:137, 2005.

[65] H.P. Mumm. *A Test of Time Reversal Violation in Neutron Beta Decay.* 2003. Ph.D. Thesis.

[66] H.P. Mumm et al. *Rev. Sci. Instrum.*, 75:5343, 2004.

[67] R.E. Williams and J.M. Rowe. *Physica B*, 311:117, 2002.

[68] A.-J. Dianoux and G. Lander. *Neutron Data Booklet, 1st Ed.* Institut Laue-Langevin, Grenoble, France, 2002.

[69] M. S. Dewey et al. *Phys. Rev. Lett.*, 91:152302, 2003.

[70] ORTEC, 801 South Illinois Avenue, Oak Ridge, TN 37830, http://www.ortec-online.com/.

[71] Glenn F. Knoll. *Radiation Detection and Measurement.* Wiley, New York, 2000.

[72] N. Tsoulfanidis. *Measurement and Detection of Radiation, 2nd Ed.* Taylor and Francis, Washington, D.C., 1995.

[73] M. Moszyński, M. Szawlowski, M. Kapusta, and M. Balcerzyk. *Nucl. Instrum. Meth. A*, 485:504, 2003.

[74] B. M. Fisher et al. *J. Res. Natl. Inst. Stand. Technol.*, 110:421, 2005.

[75] T. R. Gentile et al. *Nucl. Instrum. Meth. A*, 579:447, 2007.

[76] G.H. Rieke. *Detection of Light, 2nd Ed.* Cambridge University Press, New York, 2003.

[77] Radiation Monitoring Devices, Inc., Watertown, MA 02472.

[78] M. Boucher et al. *Nucl. Instrum. Meth.*, 505:136, 2003.

[79] M. Moszyński, M. Szawlowski, M. Kapusta, and M. Balcerzyk. *Nucl. Instrum. Meth. A*, 497:226, 2003.

[80] A.Q.R. Baron and S.L. Ruby. *Nucl. Instrum. Meth. A*, 343:517, 1993.

[81] T. Ikagawa et al. *Nucl. Instrum. Meth. A*, 515:671, 2003.

[82] R. Chen et al. *Nucl. Instrum. Meth. A*, 433:637, 1999.

[83] M. Moszyński et al. *Nucl. Instrum. Meth. A*, 505:63, 2003.

[84] M. Moszyński et al. *IEEE Trans. Nucl. Sci.*, 49:971, 2002.

[85] S.E. Derenzo, M.J. Weber, E. Bourret-Courchesne, and M.K. Klintenberg. *Nucl. Instrum. Meth. A*, 505:111, 2003.

[86] A. Lempicki. *J. Appl. Spect.*, 62:787, 1995.

[87] I. Holl, E. Lorenz, and G. Mageras. *IEEE Trans. Nucl. Sci.*, 35:105, 1988.

[88] Saint-Gobain Crystals, 12345 Kinsman Rd., Newbury, OH, www.detectors.saint-gobain.com.

[89] http://www.detectors.saint-gobain.com/.

[90] Rexon Components, Inc., 24500 Highpoint Rd., Beeachwood, OH 44122.

[91] G. Keil. *Nucl. Instrum. Meth.*, 89:111, 1970.

[92] C. Amsler et al. *Nucl. Instrum. Meth. A*, 480:494, 2002.

[93] H. Nishimura, M. Sakata, T. Tsujimoto, and M. Nakayama. *Phys. Rev. B*, 51:2167, 1995.

[94] H. V. Piltingsrud. *J. Nucl. Med.*, 20:1279, 1979.

[95] R. Moncorgé, B. Jacquier, and G. Boulon. *J. Lumin.*, 14:337, 1976.

[96] Z.H. Cho, M.H. Petroff, and R. Bharat. *IEEE Trans. Nucl. Sci.*, 14:38, 1786.

[97] E. Frlež et al. *Nucl. Instrum. Meth. A*, 440:57, 2000.

[98] E. Frlež et al. *Nucl. Instrum. Meth. A*, 459:426, 2001.

[99] Certain trade names and company products are mentioned in the text or identified in illustrations in order to adequately specify the experimental procedure and equipment used. In no case does such identification imply recommendation or endorsement by the National Institute of Standards and Technology, nor does it imply that the products are necessarily the best available for the purpose.

[100] Canberra Model 2006 Proportional Counter Preamplifier, Canberra Industries, 800 Research Parkway, Meriden, CT 06450.

[101] K.G. Kiriluk. *Understanding Photon Detector Response Functions for the Neutron Radiative Decay Experiment.* 2005. B.S. Thesis.

[102] M. Bhattacharya and E.G. Adelberger. Reanalysis of $\alpha + \alpha$ scattering and the β-delayed α spectra from ^{8}Li and ^{8}B decays, 2002. unpublished.

[103] F.E. Wietfeldt et al. *Nucl. Instrum. Meth. A*, 538:574, 2005.

[104] T. Tabata, R. Ito, and S. Okabe. *Nucl. Instrum. Meth.*, 94:509, 1971.

[105] F. B. Brown et al., 2003. A General Monte Carlo N-Particle Transport Code, Version 5 LA-UR-03-1987.

[106] I. Kremsky. *Generating Radiative Beta Decays.* 2005. B.S. Thesis.

[107] W.H. Press, B.P. Flannery, S.A. Teukolsky, and W.T. Vetterling. *Numerical Recipes in C: The Art of Scientific Computing.* Cambridge University Press, New York, 1988.

[108] www.ripplon.com.

[109] E. Kreyszig. *Advanced Engineering Mathematics.* Wiley, New York, 1999.

[110] J.F. Zeigler and J.M. Manoyan. *Nucl. Instrum. Meth. B*, 35:215, 1998.

[111] J. Sempau, J.M. Fernandez-Varea, E. Acosta, and F. Salvat. *Nucl. Instrum. Meth. B*, 132:107, 1997.

[112] S. Agostinelli et al. *Nucl. Instrum. Meth. A*, 506:250, 2003.

[113] J. Allison et al. *IEEE Trans. Nucl. Sci.*, 53:270, 2006.

[114] J.W. Martin et al. *Phys. Rev. C*, 73:015501, 2006.

[115] S. Gardner, 2006. private communication.

[116] L.M.P. Fernandes et al. *X-ray Spectrom.*, 30:164, 2001.